SILICON CARBIDE FIBRE
SILICON NITRIDE MATRIX COMPOSITES

by

A.G.Razzell, BSc (Hons)

For submission to the
degree of Doctor of Philosophy

University of Warwick

Department of Physics

July 1992

CONTENTS

LIST OF FIGURES

CHAPTER 6

TABLES

ACKNOWLEDGEMENTS

I would like to thank my supervisor, Prof. Mike Lewis for his help, encouragement and patience during the course of this work. I would also like to thank my employers, Rolls-Royce Plc. for their financial support in seconding me for the last three years. Financial support from the SERC for this project was also gratefully received.

Within Rolls-Royce, Andy Bennett, Gerry Syers, Rich Hillyer, Bob Broomfield, Colin Beesley and many others have helped and encouraged me in the project. Thanks to Ted Butler for initiating the idea of SiC reinforced Si_3N_4 within the company in the first place.

Of the many friends and collegues in the Physics department who have helped and encouraged me, I would like to thank Gerry Smith, Steve York, Dave Hammond, Steve Carpenter and especially Rebecca Cain (neé Stewart) for technical support with electron microscopy, the hot press, and material preparation. Bob Lamb was very helpful with X-ray diffraction and tape casting, Harold Mathers was always willing to make or modify equipment and Pat Beecraft was generous with his time and his workshop facilities. I would like to thank Paul Thompson for his enthusiasm for extracurricular activities.

Past and present members of the ceramics group have been helpful in a wide variety of ways. It has been a privilege to work alongside Ian Tuersley, Olwen Pullum, Markys Cain, John Fernie, Steve Ketchion, Mark Pharoah, Stuart Sutherland, John Lumby, Graeme Leng-Ward, Hong Feng and Tony 'TC' Chamberlain. Thanks especially to Adrian Daniel for the use of his indentor system.

Of the friends outside the world of ceramics, I would like to thank Philip Pring and Allan Hudson especially for encouragement during the difficult bits of the project.

I would like to thank my parents for support and encouragement, and finally I would like to thank my wife, Cathy, for her love, support and patience, especially during the writing of this thesis.

DECLARATION

This thesis is submitted to the University of Warwick in support of my application for admission to the degree of Doctor of Philosophy. It is an account of my work carried out in the department of Physics, University of Warwick during the period October 1989 to March 1992, and except where specifically acknowledged in the text, is a result of my own independent research. No part of this thesis has been submitted in respect of a degree to this or any other university.

Part of this work has previously been presented at conferences, appearing in the proceedings as follows:

1. "Silicon Carbide/SRBSN Composites", A.G.Razzell and M.H.Lewis, Ceram.Eng.Sci.Proc., **12** [7-8] pp. 1304-1317 (1991)

2. "Silicon Carbide/SRBSN Composites", A.G.Razzell and M.H.Lewis, Journal of the Royal Microscopical Soc., Special composites issue (in press)

A.G.Razzell, July 1992

ABSTRACT

Silicon carbide fibre/silicon nitride matrix composites have been fabricated using the reaction bonded silicon nitride (RBSN) and sintered reaction bonded silicon nitride (SRBSN) processing routes. A filament winding and tape casting system was developed to produce sheets of parallel aligned fibres within a layer of green matrix ('prepreg') which were cut, stacked and hot pressed to form a plate. This was nitrided and (in the case of SRBSN matrix composites) hot pressed at 1700°C to densify the matrix.

The magnesia (MgO) and the yttria/alumina (Y_2O_3/Al_2O_3) additive SRBSN systems were investigated as matrices for ease of processing and compatibility with the matrix. The MgO additive Si_3N_4 matrix reacted with the outer carbon rich layer on the surface of the fibres, forming a reaction layer approx. 2μm in thickness. A reaction layer was also observed with the Y_2O_3/Al_2O_3 additive matrix, but was thinner (<0.5μm), and was identified as silicon carbide from the electron diffraction pattern. X-ray mapping in the SEM was used to investigate the spatial distribution of elements within the interface region to a resolution <1μm, including light elements such as carbon. The 6wt%Y_2O_3/ 2wt%Al_2O_3 additive SRBSN system was chosen for more detailed investigation, and the majority of characterisation was performed using this composition.

Oxidation of composite samples was carried out at temperatures between 1000°C and 1400°C for up to 1000 hours. Little damage was visible after 100 hours for all temperatures, corresponding to a relatively small drop in post oxidation bend strength. After 1000 hours at 1000°C both carbon rich outer layers and the central carbon core of the fibre were removed. Samples were severely oxidised after 1000 hours at 1400°C, having a glass layer on the outer surface and replacement of near surface fibre/matrix interfaces with glass. The post oxidation bend strengths for both conditions were approx.$^2/_3$ of the as fabricated strength. Less damage was observed after 1000 hours at 1200°C, and the post oxidation bend strength was higher than the 1000°C and 1400°C samples.

Mechanical properties of the SRBSN matrix composite were investigated at room temperature and elevated temperatures (up to 1400°C). The average room temperature values for matrix cracking stress and ultimate strength (in bend) were 651.1 and 713.2 MPa respectively, with corresponding Weibull moduli of 5.7 and 8.7. The stresses are comparable to similar monolithic silicon nitrides. Room temperature tensile matrix cracking and ultimate strength were 232MPa and 413MPa, lower than the bend test results, which were attributed to bending stresses in the sample, lowering the apparent failure stresses. The samples failed in a composite like manner (i.e. controlled rather than catastrophic failure), with a substantially higher work of fracture than monolithic materials.

The average matrix cracking and ultimate bend strength at 1200°C were 516MPa and 554MPa, dropping to 178MPa and 486MPa at 1400°C (the matrix cracking stress was indistinct at 1400°C due to plasticity).

The creep and stress rupture properties at 1300°C were investigated in four point bend, using dead-weight loading. The creep rate was 10^{-8}/s at a stress of 200MPa, lower than a hot pressed silicon nitride with MgO additive, and higher than a hot isostatically pressed Y_2O_3/SiO_2 additive silicon nitride. A cavitation creep mechanism was deduced from the stress exponent, which was >1. Failure by stress rupture did not have a lower limit, which is also associated with cavitation of the amorphous grain boundary phase.

1.0 ENGINEERING CERAMICS

1.1 Ceramic Materials

Ceramics may be defined as inorganic non-metallic solids which normally consist of two or more species, and are usually processed at elevated temperatures. They are usually crystalline and the bonding between atoms may be ionic or covalent. Ceramics have been in existence for many thousands of years in the form of pots and tiles etc. produced by firing the required shapes in clay to produce the finished product. In recent years, developments in ceramic processing technology have allowed the direct synthesis of ceramics, with good control over composition, microstructure and properties. For this reason, ceramics have become available to the designer offering properties that in some cases are unobtainable from conventional metallic alloys.

Covalent bonding will result in high modulus and strength in a solid, the degree of covalency is dependant on the difference in electronegativity between species, a small difference giving a highly covalent bond and a large difference giving an ionic bond. The covalent bond energy is high, giving ceramics high melting/dissociation temperatures, and also resistance to chemical attack.

For this reason, ceramics are attractive for use at high temperature and/or high stress, typical current applications being tool tips for high speed machining and parts for reciprocating engines (e.g. cylinder liners, tappets, cam followers and turbocharger rotors), and potential future applications being in gas turbine engines.

1.2 Current and Future Gas Turbine Materials

The gas turbine engine consists of an air compressor, a combustor where fuel is burnt with the compressed air, and a turbine, which is driven by the expanding gases from the combustor and coupled to the compressor. This is shown schematically in fig. 1.1.

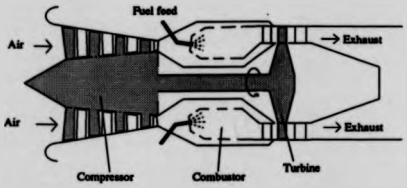

fig.1.1 Schematic arrangement of a gas turbine

The use of gas turbine engines is widespread in marine and remote electrical generating applications, where an additional turbine is added at the back end of the core in fig.1.1, and used to provide power. In aircraft applications, the exhaust is expelled at high velocity propelling the aircraft forward, an additional turbine at the back end of the core often being used to drive a fan at the front of the engine, most of the air from the fan being used to provide forward thrust, and the remainder taken into the compressor. The compression ratio and the turbine entry temperature are primary factors governing the efficiency of the gas turbine and are shown in fig 1.2. The turbine entry temperature (TET) has steadily increased [1] since the first successful gas turbines were developed, using improvements in high temperature alloys and devising more efficient ways of cooling components using a portion of the compressor air. The current TET in a typical military engine is >1800K, exceeding the melting point of the alloys used.

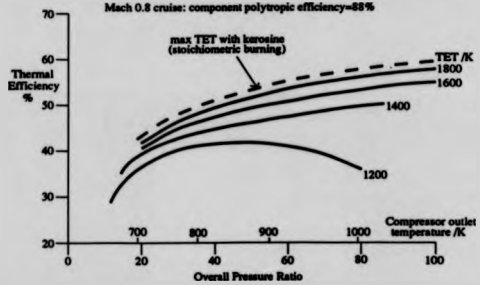

fig.1.2 Thermal efficiency vs pressure ratio and temperature for a gas turbine [1].

The thrust of modern gas turbine aircraft engines compared to their weight is significantly greater than earlier engines, and thrust to weight ratio is an important parameter for military engines (a high thrust to weight ratio gives increased aircraft performance) and for civil engines (where reductions in engine weight give an increase in aircraft payload). Replacement of high density nickel alloy components with low density ceramic components can reduce overall weight, for example, reductions in the weight of blades can give weight savings in the discs to which they are attached. An important consideration is the amount of cooling air that is used to cool components such as turbine blades and vanes. Improvements in thermal efficiency can be obtained by reducing the cooling air used. Thermal barriers in the form of porous sprayed zirconia have been used to allow increases in the gas temperature or decrease the cooling air requirements. The low thermal expansion coefficient of many ceramic materials can improve the control of blade tip clearances, and significantly improve the fuel consumption (a very important parameter for a civil engine) and the non-strategic nature of ceramic compositions make them

attractive compared to nickel alloys with rare and expensive constituents.

The combination of attractive properties that ceramics have do not necessarily make them a direct replacement for the current alloys, where a high degree of sophistication has been attained, an example being the state of the art single crystal turbine blade, with intricate cooling passages, and a well developed manufacturing route. The poor fracture behaviour of monolithic ceramics such as silicon carbide (SiC), silicon nitride (Si_3N_4) and alumina (Al_2O_3) makes them very unattractive for use in critical, high integrity components, where component failure could damage or even destroy an aircraft. Nevertheless, a lot of effort has gone into developing materials and making and testing components in gas turbines in the last twenty years. The key to improving properties, in addition to refining compositions, has been to develop manufacturing routes in which careful control and reproduceability of the processing is obtained.

1.3 Monolithic Ceramics

Monolithic ceramics may be defined as homogeneous, isotropic ceramic materials consisting of one or more phases. They range from alumina to zirconia but all have one property in common, they are brittle, that is they fail in a catastrophic manner following an elastic deformation. For a polycrystalline material to deform plastically it must have at least five independent slip systems [2] which most ceramics at room temperature do not possess (some oxide ceramics such as MgO and UO_2 exhibit plasticity at elevated temperatures because additional slip systems can operate). Also, the covalent bond is highly resistant to shear by dislocation glide at low temperatures which prevents plastic deformation. This behaviour is unattractive for structural materials in engineering

applications, a more acceptable response being a plastic deformation and a graceful failure mode as observed for many of the metallic alloys presently used.

The failure of brittle materials and the effects of cracks or flaws has been extensively investigated and reviewed [3,4], the Griffith failure criterion stating

$$\sigma \propto c^{-1/2} \qquad (1.1)$$

Where σ is the stress to failure, and c is a critical flaw size.

Any ceramic material will have intrinsic flaws within it from defects during processing (e.g. foreign inclusions, large grains, agglomerations and porosity) and may develop flaws during service (e.g. ingress of impurities, growth of voids at grain boundaries under stress and growth of cracks from machining damage). Improvements in processing methods have reduced, but not eliminated the intrinsic flaws.

A stress intensity factor at the tip of a crack in a homogeneous material can be defined as

$$K_1 = \sigma Y c^{1/2} \qquad (1.2)$$

where σ is the external applied stress remote from the crack, Y is a constant dependent on the geometry of the crack and specimen, c is the crack size (the 1 refers to mode 1 crack opening, in tension)

K_{1c}, the critical stress intensity factor may defined when the c, size of the crack becomes large enough to spontaneously grow until the material fails and has the units $MPam^{1/2}$.

K_{1c} is also known as fracture toughness, typical values for glass [4] being $0.75MPam^{1/2}$.

and for dense silicon nitride 3-8 $MPam^{1/2}$. Growth of the crack may be halted by plastic deformation at the crack tip, reducing the local stress, however as has been previously stated, plastic deformation cannot easily occur in ceramics.

The fracture toughness of a ceramic material may be increased by making the growth of a crack more difficult, by deflection when it reaches second phase particles, or by energy absorbing processes at the crack tip such as phase changes. These energy absorbing mechanisms may be produced by variations in composition and processing, or by adding second phases to the material to form a composite (see 1.4).

The grain morphology is an important parameter, elongated grains making the crack path more tortuous, causing crack deflection and crack bridging/grain pullout, giving an increased fracture toughness compared to equaixal grains of the same material [5]. The growth of elongated grains is encouraged by a high volume fraction of liquid phase present at the sintering temperature in Si_3N_4, however the high temperature properties are degraded by large amounts of grain boundary glass.

Zirconia can be stabilised in the tetragonal and cubic structures by the addition of Y_2O_3, CaO or MgO [3,6,7]. By heat treatment of a doped zirconia it is possible to precipitate tetragonal ZrO_2 particles in a metastable state within a cubic zirconia matrix. These undergo a fast, stress induced diffusionless transformation from the tetragonal structure to the room temperature stable monoclinic structure as the stress field at the crack tip approaches. This is accompanied by a molar volume change that lowers the stress at the crack tip, and is known as transformation toughening. The tensile strength of these materials may be as high as 2GPa with a room temperature toughness of $13.5MPam^{1/2}$ [8]. The degree of toughening decreases as the temperature is increased until the thermodynamic equilibrium temperature for the transformation is reached. Above this

temperature, there is only a limited toughening effect caused by the dispersed tetragonal particles, which prevents the use of transformation toughened materials in gas turbines.

In service in a gas turbine component, the stresses within the material may be 100-300MPa. For a typical dense silicon nitride, the strength may be 750MPa at the temperature of operation, and the fracture toughness value 8MPam$^{1/2}$ [1]. In this case, the critical flaw size may be 50-100 μm. Flaws of this size may occur during processing (voids or powder agglomerates within the bulk of the material) and machining (surface and sub-surface damage may be caused by grinding), and are hard to detect reliably by non destructive testing methods. Flaws may also develop at the surface of components during service as a result of oxidation and corrosion and fretting. Because flaws are likely to exist in practical components, a probabilistic fracture mechanics approach appears to be an attractive option to the designer using these materials.

Weibull statistics can be used to describe the variation in strengths of monolithic materials arising from the flaw distribution. The Weibull modulus m denotes the scatter in data, high values of m indicating a small degree of scatter and vice versa. Scatter in strength data is dependent on the stressed volume of materials [1,9], large test pieces or components having a higher probability of a critical flaw than small ones. Values of m=30 have been suggested [1] for an acceptable scatter in strength in a small (2cm^3) component with a design stress of 200MPa, and an average fracture stress of 300MPa, giving a 'probability of failure ' of 0.001%. As the Weibull modulus for current monolithic materials is between 10 and 15, the use of these materials in high stress/high integrity components such as turbine blades seems to be ruled out.

1.4 Composite Ceramics

The formation of a composite by the addition of a strong second phase in the form of particles, platelets or whiskers (single crystals) has been shown [10,11,12] to increase fracture toughness in monolithic ceramics. Adding fibres to ceramic matrices also improves the fracture behaviour. These materials are dealt with in section 1.5. The increase in toughness is caused by crack deflection, crack bridging and pullout of the second phase, each process requiring additional energy to allow the crack to propagate through the material.

Crack deflection processes have been modelled [10] for three second phase morphologies (spherical particles, platelets and whiskers) and different volume fractions. Increases in toughness were attributed to crack tilting or twisting on meeting a second phase particle, reducing the resolved stress component opening the crack at the tip and therefore the driving force for crack growth. Toughness was predicted to increase with volume fraction up to V_f=0.2 for all three second phase morphologies, with asymptotic increases at higher volume fractions. Variations in the size of second phase particles were not predicted to affect the toughness. High aspect ratio rods were predicted to cause the greatest increase in toughness (up to a factor of four higher than the pure matrix) with smaller increases for platelets and spherical particles.

Experimental work [11] was carried out on deflection processes in Si_3N_4 with high aspect ratio grains, in a lithium-alumino-silicate glass ceramic with lath-shaped crystals, and in a barium silicate glass ceramic with spherulite grains. These results validated the model in [10] for the second phase size and morphology effects.

The interface between the matrix and the second phase is important, in that it determines

whether the crack is deflected by the second phase particle (weak interface) or goes through the particle (strong interface).

Crack bridging (i.e. the microcracking of the matrix, the load being transferred to the second phase) is only applicable when high aspect ratio, strong second phase particles e.g. whiskers are added to the matrix. In this case, the interface must be strong enough to allow load to be transferred to the whiskers, but not so strong that the crack passes through the whiskers.

Energy can be absorbed by the frictional resistance of the ruptured interface to the pullout of the whiskers and by the fracture of the interfacial bond between the whisker and the matrix. The whisker volume fraction and average length affect the amount of energy absorbed, and an additional requirement is that the whiskers are parallel sided and smooth enough to allow pullout to occur. The whisker morphology is dependent on the manufacturing process conditions. Whiskers have been observed with variations in diameter with length that would cause them to 'jam' in the matrix and fracture before absorbing energy by pullout.

1.5 Continuous Fibre Ceramic Matrix Composites

Ceramic fibres may be incorporated into ceramic matrices to form ceramic matrix composites (CMCs). The fracture behaviour of a continuous fibre CMC is very different from the monolithic ceramics, being analogous to ductile metallic behaviour, although the mechanisms operating are different (fig.1.3). The load deflection curve is linear up to the matrix cracking load, at which there is a departure from linearity. The matrix continues to crack into smaller and smaller blocks until a peak load is reached, at which the fibres are

carrying all the load. Following the peak load, there is a graceful load drop accompanied by further elongation as fibres break and pull out of the matrix. The multiple matrix cracking, the fibre breakage and pullout are all processes that absorb energy, the total work of fracture being many times that of the monolithic matrix material.

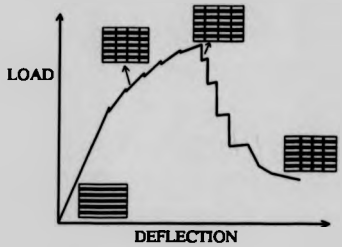

fig.1.3 CMC fracture behaviour

For high temperatures, a variety of materials may be chosen for use as fibres and matrices [13], elements such as hafnium and molybdenum, and compounds such as silicon carbide and boron nitride. The melting (or dissociation) point of an element or compound is not necessarily the prime consideration in choice of material. Density, thermal expansion, Young modulus, creep behaviour and chemical compatibility with the second phase and the environment are also important factors in the choice of constituents for a composite material. The processing requirements of the matrix are important to consider when the temperatures are substantially greater than the service temperature of the composite - an example being dense silicon nitride, which may have to be processed at between 1700°C and 1850°C, but would only be used at up to 1400°C. In this case, the

ability of the fibres to withstand the hot pressing schedule is a critical consideration. Of equal importance is the availability of high temperature materials in fibrous form. Only a handful of the materials reviewed in [14] have been successfully made into fibres, and even fewer are available commercially.

Carbon fibre reinforced glass was the first ceramic matrix composite system to be studied. However the poor oxidation resistance of carbon made the practical use of the material limited (oxidation of carbon fibres occurs above 400°C). The material is useful in allowing fabrication routes to be explored (prepreg preparation, hot pressing) and in testing theoretical models [15]. Carbon reinforced carbon [16] is a composite that has found a variety of uses in spacecraft re-entry shields (good thermal shock resistance), aircraft and racing car brake discs (lack of brake "fade"), and prosthetic implants (inertness in vivo). The inherently poor oxidation properties of the material make it unattractive for use in gas turbines. However for short life demonstrations of component shapes, the material may have some benefits, as its temperature limitation in inert conditions or vacuum is very high indeed (2500°C).

Carbon fibres remained the only small diameter fibre capable of withstanding the high temperatures during matrix fabrication until the development of silicon carbide based fibres produced by the polymer pyrolysis route [17,18,19]. The commercially available fibres (Nicalon by Nippon Carbon, and Tyranno by UBE) have been incorporated into glass [20], glass ceramics [15] and silicon carbide [21] matrices. Glass and glass ceramic matrix composites are produced by making a prepreg from fibre tows and glass frit, followed by hot pressing, usually in the 900-1300°C temperature range (depending on matrix composition). Silicon carbide matrix composites are produced by the chemical vapour infiltration route (CVI), a fibre preform being heated to between 1100° and

1300°C, and silicon carbide being deposited by the thermal decomposition of methyl trichlorosilane. The material is inherently porous as a result of the process. A drawback of the fibres used is their instability at high temperature, grain growth and evolution of carbon monoxide progressively reducing the strength above 1100°C.

Another class of fibres (also referred to as monofilaments) have been developed for use in metal matrix composites, using matrices such as aluminium and titanium [22]. These are produced by the chemical vapour deposition (CVD) of silicon carbide or boron onto a substrate of tungsten or carbon. The fibre diameter is typically 100-150μm and is therefore not as easy to handle or design with as the Nicalon or Tyranno fibres, however the temperature capability is higher. This opens up the potential of using silicon nitride matrices (typical processing temperature of 1700°C) which are well characterised as monolithic materials, and have higher temperature capabilities than glass ceramics. This has been investigated in this work, using Textron SCS-6 fibres in a hot-pressed reaction bonded silicon nitride matrix. Dense silicon nitride is a very promising matrix material, because the processing requirements are well understood, reproducible and relatively cheap, compared to chemical vapour infiltration (CVI) methods used in the production of SiC/SiC composites. The SCS-6 silicon carbide fibres have an as-recieved strength of 4GPa, which is almost twice that of the small diameter Nicalon fibres. The SiC fibre/Si_3N_4 matrix combination has the potential for operation above 1000°C, and has previously been studied in various forms (reaction bonded matrix [23-29], hot pressed matrix [30,31,32]) although the sintered reaction bonded silicon nitride (SRBSN) route does not appear to have been studied before. The advantage of this process route is the reduced shrinkage that occurs during sintering (or hot pressing), which is important when fibres that restrain any shape changes are incorporated into the material.

CHAPTER TWO CONTINUOUS FIBRE CMCS

2.1 CLASSICAL COMPOSITES

The behaviour of continuous fibre composites with polymer based matrices has been investigated in some depth, and such materials are now being increasingly used in engineering and aerospace applications. The methods used to describe the elastic behaviour of these materials can be used to describe the elastic behaviour of ceramic matrix composites.

Before describing the behaviour of a complete composite laminate, it is useful to concentrate on an individual lamina. This may consist of a section of matrix containing a planar array of parallel, equally spaced fibres (fig.2.1). The longitudinal Youngs modulus of the lamina can be shown [33] to be

$$E_l = E_f V_f + E_m(1-V_f) \qquad (2.1)$$

where E_f, E_m are the fibre and matrix moduli, and V_f is the fibre volume fraction. The assumptions made are that the strains in the fibre and matrix are identical, and that Poisson contraction effects are small. The above equation (known as the rule of mixtures) has been verified experimentally in polymer matrix/glass fibre systems. The Young moduli of the fibres and matrices in CMC's are more alike than in the polymer/glass systems and errors due to Poisson contraction effects could be expected to be smaller.

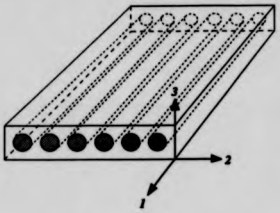

fig.2.1 Single lamina

The transverse modulus E2 can be derived in a similar fashion [33].

$$E_2 = \frac{E_f E_m}{V_f E_m + (1-V_f) E_f} \qquad (2.2)$$

In this case, the stress in the fibre and matrix is assumed to be the same, with perfect stress transfer across the fibre/matrix interface. The errors due to Poisson contraction effects are more severe in this case and experimental data from polymer/glass systems do not fit the equation perfectly.

The elastic properties of unidirectional laminae when the stress field is at an angle to the fibre direction have been calculated by previous workers, and a summary is given in [33]. The general form of the variation of moduli with direction are shown in fig. 2.2a, Ex and Ey refer to moduli measured in a new coordinate system rotated by θ degrees from the 1-2 directions respectively. The variation in shear modulus and Poissons ratio with angle is shown in fig.2.2b

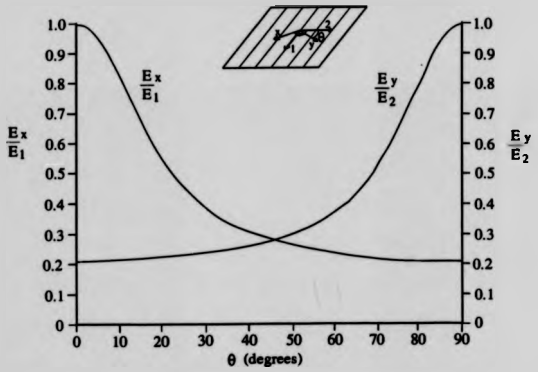

fig.2.2a Variation of modulus with ply angle (from [33])

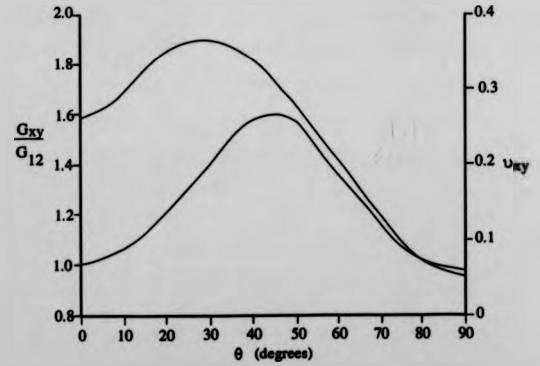

fig.2.2b Variation of shear modulus and poissons ratio with ply angle (from [33])

2.2 BRITTLE MATRIX COMPOSITE THEORY

There are a number of processes that absorb energy during the fracture of a ceramic matrix composite or CMC. These may include work done during matrix or fibre cracking (either single or multiple cracking), work done during fibre/matrix debonding, and work done during fibre pullout. The cracking behaviour of a composite with a brittle matrix (i.e. a linear stress-strain relationship leading up to a catastrophic failure) has been considered by a number of workers (34-45) and has recently been reviewed (42). The paper by Aveston, Cooper and Kelly (34),referred to as ACK), has formed the basis for much of the subsequent work, and is reviewed below.

Aveston, Cooper and Kelly

Considering a fibrous composite in uniform tension in which one of the phases breaks at a lower elongation than the other (fig. 2.3), if the remaining phase is able to bear the additional load transferred to it, then multiple fracture of the weaker phase will occur. Conversely, if the additional load is too great, the composite will fail with a single fracture. The weaker phase may be either the fibre or the matrix, however it is conventional for the fibres to have a higher strength and strain to failure than the matrix.

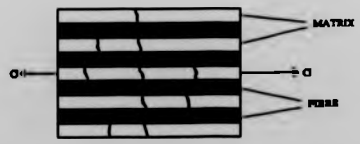

fig. 2.3 Schematic view of unidirectional fibre composite under load

In the case of high strength fibres in a lower strength matrix, multiple fracture (of the matrix) will occur when;

$$\sigma_{fu}V_f > \sigma_{mu}V_m + \sigma_f'V_f \qquad (2.3)$$

where V_f= Volume fraction of fibres, V_m= Volume fraction of matrix, σ_{fu} = Ultimate fibre strength, σ_{mu}= Ultimate matrix strength, σ_f'= Stress in fibre necessary to exceed the strain to failure in the matrix.

If the above inequality is not true, the composite will fail in a single fracture, as the additional load applied to the fibres following matrix cracking exceeds σ_{fu}. In the multiple fracture case, the matrix cracks into blocks with lengths between x and 2x where x is determined by the rate of transfer of shear stress from the fibre to the matrix across the interface. The strength of the interface (τ) is a determining factor in the rate of shear stress transfer.

Balancing the forces at the interface;

$$2\pi rNx\tau = \sigma_{mu}V_m \qquad (2.4)$$

N is the number of fibres per unit area, r is the fibre radius. Since N may be substituted for $V_f/\pi r^2$, the equation may be rearranged to give

$$x = (V_m/V_f)\,\sigma_{mu}r/2\tau \qquad (2.5)$$

The crack spacing in the matrix is therefore dependant on fibre radius and inversely

dependant on fibre volume fraction and the shear strength of the fibre/matrix interface. The inequality in (2.3) may be illustrated graphically (fig.2.4), and shows that a critical value for V_f exists where a transition from single to multiple fracture occurs

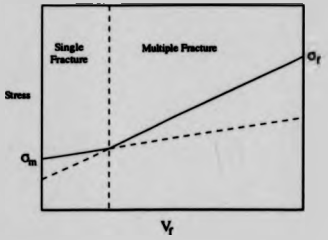

fig.2.4 Dependence of fracture mode on fibre volume fraction

The idealised stress/strain curve for a brittle matrix composite is shown in fig.2.5 below. The curve describes the behaviour of a composite with a single, well defined matrix failure strain, thus keeping the stress during matrix failure constant. The matrix starts to fail at 'A', cracking into smaller and smaller lengths until the blocks of matrix are all between x and 2x in length. The fibres are then carrying all the applied load, and continue to stretch, until they fail. The modulus of the composite during this stage is reduced to $E_f V_f$, and failure of the fibres occurs at $\sigma_{fu} V_f$.

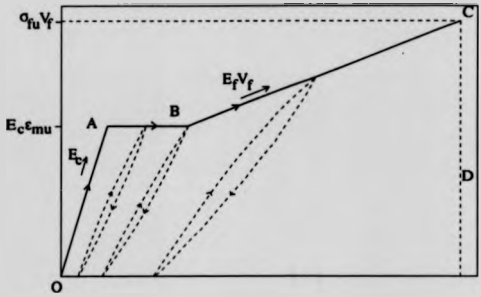

fig.2.5 Schematic stress/strain curve of an ideal brittle matrix composite

Unloading the composite produces a hysteresis, the composite failing to return to its original length after ε_{mu} has been exceeded. This is because the matrix/fibre interfacial shear stress τ clamps the fibre in the matrix blocks, preventing sliding back to the original positions.

The behaviour of a real composite is different in that the matrix exhibits a range of failure strains (in a uniform stress field, the weakest part of the matrix is the first to fail, the strongest is the last). This results in a stress/strain curve in which the stress rises during the matrix cracking phase (fig.2.6).

Again, on unloading, the strain does not return to zero, but to a finite level, indicating irreversible energy absorbtion. It is this energy absorbing behaviour that makes these CMC's attractive as engineering materials, as they absorb energy under rising load conditions throughout the specimen, before the ultimate tensile stress (UTS) is reached.

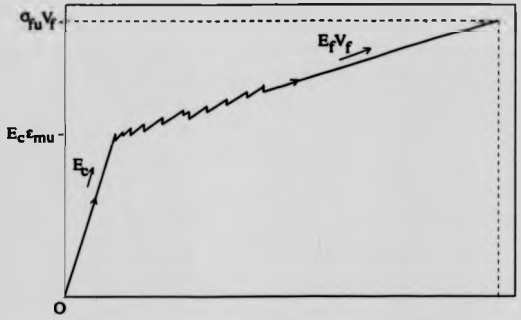

fig.2.6 Schematic stress/strain curve of a practical brittle matrix composite

The energy absorbed during fracture can be broken down into a number of contributions [34]. If a single matrix failure is considered then work done during debonding of the fibre from the matrix, work done in causing the matrix to crack, work done in breaking the fibres and work done in pulling the fibres out of the matrix against frictional forces at the interface may be considered. The work done in interfacial debonding and fibre pullout are found to increase with increasing fibre diameter and decreasing interfacial shear strength. For the fibre pullout contribution, the increased toughness of the composite is only obtained at the expense of composite strength.

An increase in matrix cracking strain ε_{mu} may occur as the diameter of the fibre is reduced. It can be shown that the matrix cracking strain in this case is given by:

$$\varepsilon_{mu} = \left(\frac{6\tau G_m E_f V_f^2}{E_c E_m^2 r V_m} \right)^{1/3} \qquad (2.6)$$

Where G_m is the matrix fracture energy and E_c is the composite modulus. The linear part of the stress/strain curve is therefore extended to a higher stress given by $E_c\varepsilon_{muc}$, after which the matrix breaks into a series of blocks of length between x and 2x. The work of fracture increases with increasing ε_{muc} until $E_c\varepsilon_{muc}=\sigma_{fu}V_f$ where there is a transition from multiple fracture to single fracture, and a sharp drop in energy absorption. The failure strain of the composite and ability to withstand stress after the initial matrix cracking both reduce with increased matrix failure strain, so the composite appears to behave in an increasingly brittle manner.

As can be seen in equation (2.6) a high fibre/matrix interfacial shear strength will cause an increase in matrix failure strain, composites with high strength bonding at the interface will exhibit more brittle behaviour than comparable systems with a weak interface.

RECENT DEVELOPMENTS IN CMC THEORY

More recent work has concentrated on a fracture mechanics approach to the analysis of CMC failure. The ratio of fibre fracture energy to interface fracture energy must be smaller than 1/4 for the matrix crack to be deflected along the interface rather than propagate through the fibre [42]. This is a theoretical prediction, but observations of debonding mechanisms in SiC/Pyrex[43] and SiC/LAS [42] composites have shown embrittlement when oxidation has removed the graphitic interface layer, replacing it with silica, and greatly increasing the interface bond strength.

The steady state cracking stress is given by equation 2.7 [42], showing the relationship between cracking stress σ_m and matrix fracture energy G_m, fibre radius r, fibre volume fraction V_f, interfacial shear strength τ, fibre and matrix moduli E_f and E_m and composite modulus E_c.

$$\sigma_m = \left[6G_m \frac{\tau E_m E_f V_f^2}{r E_c (1-V_f)} \right]^{1/3} \qquad (2.7)$$

The ACK theory assumed a single fibre strength, whereas in reality, fibres have a strength distribution that can be described using Weibull statistics. Thus the ultimate strength of a composite is given by [42]

$$\sigma_u = V_f S f \qquad (2.8)$$

S is the fibre strength and f is a function of τ,r,m,x and L, where m is the fibre Weibull modulus, x is the crack spacing and L is the gauge length. The dependence of ultimate strength on test piece size is also seen in monolithic ceramics [9], which also show a Weibull distribution of strengths.

The increase in composite fracture energy under steady state crack growth conditions can be calculated from integrating the area under the stress displacement curve [42], obtaining (for m=infinity,i.e. a single fibre strength value and a zero pullout length)

$$\Delta G_c = \frac{S^3 r V_f (1-V_f)^2 E_m^2}{6\tau E_f E_c^2} \qquad (2.9)$$

An important point to note is that the toughening increment increases with r/τ whereas the matrix cracking stress in equ.2.7 decreases with r/τ, which is in keeping with the earlier

ACK model. With fibres with a finite m, the toughness has contributions from unbroken and from broken fibres. From [42] the unbroken (i.e. crack bridging) fibre contribution is given by

$$\Delta G_b = 4V_f TU/(m+1) \qquad (2.10)$$

where T and U are pullout parameters, and U being proportional to $(r^{m-5}/\tau^{m-2})^{1/(m-1)}$. There is an inversion in the trend with τ at a value of m=2 and an inversion in the trend with r at m=5. For the broken fibres, the energy contribution due to pullout is given by an equation of the form

$$\Delta G_b = \langle h \rangle^2 (\tau/r) \qquad (2.11)$$

where $\langle h \rangle$ is the average fibre pullout length. $\langle h \rangle$ can be related to m, S_0 (a scale parameter for the fibre strength distribution) to give an energy contribution proportional to

$$[r^{m-3} S_0^{2m}/\tau^{m-1}]^{1/(m-1)} \qquad (2.12)$$

The important conclusions from this theory are that the toughness increases with fibre radius when m>5 and decreases when m<3, and that when m<1 (wide scatter in fibre strength) toughness increases with τ, and when m>2 it decreases with τ. The value of m is thus a crucial factor in the choice of τ when designing composite systems. It should be noted that the value of m in these equations is for the fibre within the composite, not for as produced fibre.

ACK model. With fibres with a finite m, the toughness has contributions from unbroken and from broken fibres. From [42] the unbroken (*i.e.* crack bridging) fibre contribution is given by

$$\Delta G_b = 4V_f TU/(m+1) \qquad (2.10)$$

where T and U are pullout parameters, and U being proportional to $(r^{m-5}/\tau^{m-2})^{1/(m-1)}$. There is an inversion in the trend with τ at a value of m=2 and an inversion in the trend with r at m=5. For the broken fibres, the energy contribution due to pullout is given by an equation of the form

$$\Delta G_b = \langle h \rangle^2 (\tau/r) \qquad (2.11)$$

where $\langle h \rangle$ is the average fibre pullout length. $\langle h \rangle$ can be related to m, S_0 (a scale parameter for the fibre strength distribution) to give an energy contribution proportional to

$$[r^{m-3} S_0^{2m} / \tau^{m-1}]^{1/(m-1)} \qquad (2.12)$$

The important conclusions from this theory are that the toughness increases with fibre radius when m>5 and decreases when m<3, and that when m<1 (wide scatter in fibre strength) toughness increases with τ, and when m>2 it decreases with τ. The value of m is thus a crucial factor in the choice of τ when designing composite systems. It should be noted that the value of m in these equations is for the fibre within the composite, not for as produced fibre.

2.3 REVIEW OF CMC SYSTEMS

Combinations of materials that have been studied include carbon or silicon carbide fibres/borosilicate glass [15,20,46], silicon carbide fibres/lithium aluminosilicate (LAS) [47,48], carbon fibres/carbon matrix [46,49], carbon fibres/silicon carbide matrix, silicon carbide fibres/silicon carbide matrix [16,21,50], silicon carbide fibre/mullite [51]

Carbon fibre reinforced carbon has good properties that are stable with temperature to at least 1500°C in inert atmospheres, low density (1.8 gcm^{-3}) and has been used extensively in rocket engines and in the nose cone and wing leading edges of the NASA space shuttle [16]. A lack of oxidation resistance (unprotected C/C oxidises at above 400°C) makes its use in gas turbines unattractive, where gas temperatures of 1850°C and a large number of cycles are encountered, although protected C/C may have uses in exhaust components. C/C is produced by the CVI process, in which a carbon fibre preform (often with a porous pyrolysed polymer matrix) is infiltrated with carbon produced by the decomposition of methane gas. Protection systems based on SiC coatings and borosilicate glass sealants are applied to finished components, and provide limited protection. A similar material is SiC/SiC in which a silicon carbide matrix is applied by CVI to a fibre preform held in a graphite tool. Nicalon fibres are used in the majority of SiC/SiC composites implying a temperature limit of 1200°C. The strength of the material is low (100 MPa for 2D woven material [21]) because the of matrix porosity, (the porosity in CVI matrix composites is inherent in their production). However SiC/SiC (and a variant C/SiC) has been demonstrated in exhaust components and has flown on a Snecma aircraft. A layer of graphitic carbon is applied to the fibres in the preform stage, prior to application of the SiC matrix, to give a weak interface between the fibre and matrix. This is necessary to allow

debonding to occur during failure, allowing energy absorbtion and a non-catastophic failure. The low oxidation resistance of this layer (around 1μm thick) is poor, and damage can occur to the composite via 'pipe' oxidation along the interface.

Glass and glass ceramic composites have been studied, both as model materials, and as potential engineering materials in their own right. Glass 'frit' (powdered glass) is mixed with a binder and a solvent (usually a water based system) and a desired fibre tow is passed through, picking up glass particles. The impregnated tow is then wound onto an octagonal drum to create flat sheets of 'prepreg' and dried. Prepreg sheets are cut and stacked in a graphite die and hot pressed at a temperature high enough to make the glass fluid, to densify the composite. Borosilicate glasses, calcium alumino-silicate, barium alumino-silicate, magnesium alumino-silicate and lithium aluminosilicate are among the compositions that have been investigated, all materials showing composite behaviour, with large amounts of energy absorbed during fracture. The temperature limitation of these materials is dependant largely on the matrix properties, borosilicate matrices such as Pyrex being limited to 550°C-600°C, and glass ceramic matrices to potentially 1200°C depending on composition, and the quantity of residual glass present. The processing of glass ceramic compositions requires careful control of the temperature cycle used during pressing to obtain matrix densification in the glassy state prior to the onset of crystallisation, and satisfactory conversion to the crystalline state afterwards.

The properties of the various composites are shown in table 2.1. It should be noted that tensile tests and bend tests cannot be directly compared, and that the fibre layup varies. The absence of an OMF (onset of matrix failure) does not necessarily indicate a 'brittle' failure as some fibre debonding and pullout may occur, although the failure is likely to be a mixture of tensile and shear (especially if the test is performed in flexure)

Composite System	Ref	Layup	V_f /%	E /GPa	CMF /MPa	UTS /MPa
Carbon fibre/glass	56	0°	50	100	100	830
SiC/glass	58	0°	40	120	-	340 (bend)
SiC/LAS	57	0°	44	136	301	480
SiC/SiC (2D)	52	0/90	-	-	100	230
SiC/Mullite (Textron SCS-6)	55	0°	25	82	-	700(bend)

table 2.1

2.4 SILICON NITRIDE MATRIX COMPOSITES

There has been relatively little published on silicon nitride matrix composites, using silicon carbide fibres as a reinforcement, much of the composite work undertaken on the SiC/Si_3N_4 system has been on particle and whisker reinforced/toughened materials. The difficulty of retaining fibre integrity during processing of the Si_3N_4 matrix (especially using fibres derived from the polymer route) is a likely reason. Composites using Si_3N_4 in the reaction bonded form (RBSN) as a matrix (where finely divided elemental silicon is reacted with gaseous nitrogen at temperature) have been investigated particularly by Bhatt and co-workers [23-27], and by Corbin et al [28]. CVD (chemical vapour deposition) SiC fibres by Textron (formerly AVCO) were used as reinforcement in the composite and a range of properties investigated. Another composite using RBSN as a matrix was investigated by Lundberg et al [29] using Nicalon fibres (polymer derived), and showed non-brittle behaviour with fibre pullout.

Composites using Si_3N_4 in the dense form (hot pressed) have been investigated by Shetty et al [30], Miyoshi et al [31] and recently (i.e. after this program of work was started) by Foulds et al [32] from Textron.

Reaction bonded silicon nitride matrix composite.

The work by Bhatt [23-27] was initially the most influential in this program of work, as the mechanical and thermal behaviour of the composite (Textron SCS-6 fibres in an RBSN matrix) were investigated in reasonable depth, and the reported properties were encouraging (see table 2.1 at the end of this section). The composite exhibited a 'classic' load/deflection curve as predicted in ACK theory, the matrix cracking stress being 237±25 MPa at a fibre volume fraction of 23±3% and 293±15 MPa at a volume fraction of 40±2%. Multiple cracking occurred during matrix failure, and a value for fibre/matrix interfacial shear strength of 10MPa was calculated from the crack spacing. Thermal stability was investigated, and the results compared to commercial RBSN, HPSN and unidirectional SiC/SiC by the CVI route (the ultimate strength of the materials in 4 point bend at the test temperature was the parameter chosen for comparison). The results are reproduced in fig 2.7 below.

Environmental stability was studied by heat treating the composite samples in flowing oxygen and in nitrogen at temperatures up to 1400°C for 100 hours. The effect of nitrogen was minimal except at 1400°C where a slight drop-off in ultimate strength occurred. Oxygen lowered the strength from between approx 400 and 1200°C, the matrix cracking stress and ultimate strength recovering a little at temperatures above 1200°C. These results were attributed to the ingress of oxygen through the porous RBSN matrix and at the exposed ends of the fibres, causing internal oxidation of the matrix, and oxidation of the carbon rich fibre/matrix interface. The high oxygen transport rate and poor oxidation behviour of an RBSN matrix are an inherent limitation of its use in composites for operation at intermediate temperatures (400-1000°C).

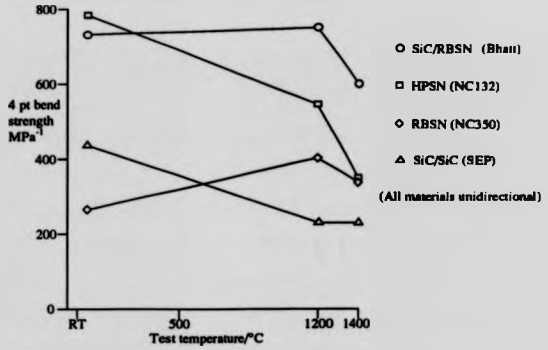

fig 2.7 SiC/RBSN compared to other materials (after Bhatt [23])

Work by Corbin et al [28] on a 50-60% fibre volume fraction RBSN matrix composite yielded a maximum flexural strength of 900 MPa at room temperature. Textron fibres SCS-6 and SCS-2 were used in the composites, the SCS-2 fibre having a thinner (1μm) carbon coating than the SCS-6 fibre (3μm). The SCS-2 composites showed poorer ultimate strength and energy absorption properties than the SCS-6 composites, which was attributed to a greater interfacial shear bond strength. The span to depth ratio of the samples tested was between 8:1 and 12:1 and shear failure was seen between laminates during flexural testing, particularly in the SCS-6 composites. Evidence of a reaction between the carbon layer and the silicon in the matrix was found using scanning auger microanalysis, the SCS-2 composite having a thinner layer of carbon present (before

processing of the composite) which reacts completely with matrix silicon. The low strength and low toughness of SCS-2 composites was attributed to a lack of this carbon layer preventing shear failure at the interface.

Although the production of a Nicalon reinforced RBSN must involve temperature excursions into the region where fibre degradation has been observed, composites have been produced by Lundberg et al [29], using a modified nitriding cycle that only holds at 1350°C for 3 hours. Silicon powder was milled with silicon nitride powder in order to disperse it and to increase the silicon surface area, yttria and alumina were also added (they are used in conventional pressureless sintered materials, but are also observed to increase nitriding rates). A slip containing the milled powder mixture was used to infiltrate a set of stacked fibre tows, dried and nitrided. Although no mechanical properties were reported, composite behaviour (i.e. a matrix cracking stress, fibre pullout and non-catastrophic failure) was observed.

Dense silicon nitride composites

At the start of this program of work, there was little work reported on fibre composites using silicon nitride in the dense form (hot pressed, pressureless sintered or HIPped). Work by Shetty et al [30] using SCS-6 fibres in an HPSN matrix showed that that strength reduction from 930 MPa to 430 MPa occurred, and single edge notched beam (SENB) fracture toughness only increased from 7.2 $MPam^{1/2}$ to 8.4 $MPam^{1/2}$. Composite like behaviour was observed during flexural testing, although the maximum load reached always corresponded to the first matrix crack, subsequent loads being less than this value. Fibre damage during processing was thought to be the cause, and a major factor in limiting

toughness increments of the composite compared to the unreinforced matrix. Possible causes of this fibre damage were thought to include exposure to the high hot pressing temperature, residual tensile stress from differential expansion of the fibre relative to the matrix and damage due to the loads applied during hot pressing. In addition, the large diameter of the SCS-6 fibres was thought to reduce the composite strength by allowing them to act as critical flaws in the matrix (the reduction in strength compared to the monolithic matrix could be related a critical flaw size of 90μm, close to the fibre diameter).

A survey of fibre reinforced SiC and Si_3N_4 matrix composites by Miyoshi et al [31] showed more encouraging results than [30], a flexural strength of 600MPa and an SENB fracture toughness of 17MPam$^{1/2}$ at a fibre volume fraction of 15% was reported for SCS-6 fibres in a hot pressed Si_3N_4 matrix. SiC matrix composites using the SCS-6 fibre were less encouraging as the surface carbon layers on the fibre were removed during processing of the composite causing a strong fibre/matrix bond to be formed, the composite fracturing in a brittle manner. Addition of carbon (10wt%) to the matrix composition appeared to alleviate the problem to some extent, and fibre pullout during fracture was observed. The outer carbon layers on the SCS-6 fibre were removed by oxidation and a further composite produced using a hot pressed silicon nitride matrix. A high interfacial bond strength resulted, the composite behaved in a brittle manner and no fibre pullout was observed.

During the time that this work was in progress, there have been a number of reports on a hot-pressed silicon nitride matrix composite by Textron, the manufacturer of SCS-6 fibre [32]. The material described has good properties (see table 2.1), behaving in a composite like manner in all the tests performed. An unusual feature of the processing of the material was the high pressing pressure used, 70MPa. This compares with 27MPa used in the work

by Shetty. High temperature exposure was carried out, at times of up to 100 hours and temperatures up to 1371°C (2500°F). Reductions in strength were observed after exposure, typically 50% of the as produced room temperature values of matrix cracking stress, ultimate bend strength and elastic modulus. The reductions in properties were attributed to oxidation damage to the matrix, a porous, cracked oxide scale forming on the composite surfaces. Similar reductions in strength had been observed in monolithic matrix material under the same conditions. Chevron notch tests were used to measure energy of fracture, by integrating the area under the load/deflection curve. Increases of 493% for the energy to the peak stress and 2350% for the energy to full deflection were measured for the composite, compared to monolithic Si_3N_4.

The properties of the various silicon nitride matrix materials discussed are shown in table 2.2 below.

Author, ref	Fibre	Matrix	Vf %	OMF/ MPa	OMF strain %	UBS/ MPa	UBS strain %	Fracture toughness MPa.√m
Corbin [28]	SCS-6	RBSN	50-60					
Bhatt [23-27]	SCS-6	RBSN	30	227	0.11	682	0.45	13
Shetty [30]	SCS-6	HPSN	44	400	-	-		7
Miyoshi [31]a	SCS-6	HPSN	15		-			7 - 8
b	SCS-6	HPSN	15			600		13

N B. OMF = onset of matrix fracture UBS = Ultimate bend strength
t in bend data column denotes tensile data
a surface carbon layers removed from fibre prior to composite fabrication
b surface carbon layers intact

table 2.2

2.5 MATRIX SELECTION AND PROPERTIES

Silicon nitride (Si_3N_4) is a covalently bonded crystalline solid that has a high dissociation temperature, low density, high elastic modulus, high flexural strength and low coefficient of thermal expansion. These properties, as has already been stated, make the material attractive for use in high temperature structural applications e.g. in gas turbines.

The material has two crystalline forms, α and β which are hexagonal structures, the c lattice parameter in the α form being twice that in the β form. The β form is illustrated below, showing the tetrahedral SiN_4 units joined at the corners to others in a three dimensional structure (fig.2.8).

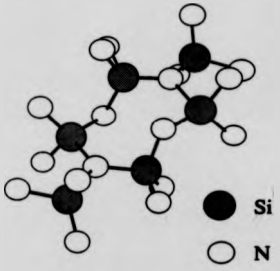

fig. 2.8 Crystalline structure of β Si_3N_4

The α form differs from the β form in that layers containing Si and N atoms are arranged in an ABCDABCD..... order rather than an ABAB..... order, layers C and D being mirror images of A and B.

The formation of the α form is generally associated with lower temperature reactions in the vapour phase, such as those that occur during the nitriding process, where Si or SiO in vapour form react with gaseous nitrogen. As temperature is increased, β-Si_3N_4 either forms preferentially, or results from transformation of the α phase.The formation of β also appears to be associated with the formation of a liquid phase. Transformation from α to β has been observed during annealing of RBSN, and also during the sintering of dense silicon nitrides using α Si_3N_4 powder with metal oxide sintering aids. Due to the covalent bonded nature of pure Si_3N_4 it is not possible to sinter the material directly, as the self diffusivity is low, so sintering aids are added to promote a liquid phase sintering process.

Reaction bonded silicon nitride

The formation of RBSN is a well documented process, and the material is produced commercially for use in high temperature applications. Silicon powder of size 10μm (typically) is cold pressed into a billet and nitrided at up to 1400°C for several days. The milled silicon powder is reactive, and a surface film of SiO_2 forms on each particle on exposure to the atmosphere which inhibits the nitridation reaction as nitrogen cannot get to the silicon surface to react. This layer may be removed [52] by reaction with impurities or by pretreatment in a vacuum, Ar or H_2 at high temperature prior to nitriding taking place. The temperature of the nitriding furnace is carefully controlled as the melting point of silicon is 1410°C and the reaction is exothermic. Local melting of Si is to be avoided as it creates globules that are unable to react with nitrogen except at the surface, and are potential flaws in the material. Three reaction mechanisms are thought to exist between silicon and nitrogen;

$$3Si\ (s) + 2N_2\ (g) \rightarrow Si_3N_4\ (s) \qquad \Delta G^\circ = -723 + 0.315T\ kJmol^{-1} \qquad (2.7)$$

$$3Si\ (l) + 2N_2\ (g) \rightarrow Si_3N_4\ (s) \qquad \Delta G^\circ = -874 + 0.405T\ kJmol^{-1} \qquad (2.8)$$

$$3Si\ (g) + 2N_2\ (g) \rightarrow Si_3N_4\ (s) \qquad \Delta G^\circ = -2080 + 0.757T\ kJmol^{-1} \qquad (2.9)$$

Equations (2.7) and (2.8) are both only valid at temperatures near the melting point of pure silicon, and it is thought that they describe the formation of β-Si_3N_4, whereas equation (2.9) refers to the likely formation conditions of α-Si_3N_4. Depression of the silicon melting point by impurities such as Fe allow equation (2.8) to remain valid at below 1410°C. The reaction between silicon monoxide (SiO) and nitrogen is is often associated with α-Si_3N_4, and is described by (2.10) below.

$$3SiO\ (g) + 2N_2 \rightarrow Si_3N_4\ (s) + {}^3/_2\ O_2\ (g) \qquad (\Delta G\ +ve) \qquad (2.10)$$

The reaction can occur in spite of the fact that ΔG° is positive because the presence of hydrogen gas in the nitriding atmosphere encourages the formation of SiO from SiO_2 (on the surface of silicon particles) by lowering the O_2 partial pressure. In general, the α-phase morphology is needle-like, the β being more equiaxed. A layer of fine whiskers (dia. 0.05-0.2μm) of α forms on free surfaces, possibly via a vapour-liquid-solid (VLS) process, as impurities are often found at whisker origins. α-Si_3N_4 also forms on the surface of silicon grains, an island of nitride building up, removing the silicon around it. Porosity in the original silicon grain is formed by this mechanism, leading to an increase in surface area for reaction to occur. Vapour phase reactions may occur within pores allowing them to fill completely with α. β-Si_3N_4 may form in the solid state by the growth of an oriented β

crystal in a silicon grain, nitrogen diffusing down the hexagonal tunnels in the <001> direction to the reaction site.

The microstructure of RBSN is dominated by the macroporosity associated with the original silicon grains, microporosity is evident at higher magnification, associated with the fine needles of α-Si_3N_4. Porosity levels of between 25 and 15% are present in typical RBSN, the value depending on the size and size distribution of the starting powder, and the processing conditions. Unreacted silicon is usually present at concentrations of up to 5%, appearing as bright grains in a polished sample. The α content may be 80%, β 15% and the remainder silicon or silicides formed with impurities. Phase concentrations may be measured routinely using X-ray diffraction.

In the manufacture of shapes, the green compact is often pre-sintered to allow green machining to be performed prior to nitriding. The shape change on nitriding is minimal, a typical linear change of ±0.1% occurring, so green machining is an effective step to produce near net shape. Fracture strengths of up to 350MPa with a Weibull modulus of 20 may be obtained with the correct choice of silicon powder, and optimised processing. The initial silicon particle size distribution and purity are critical factors in producing consistent results. Poor oxidation resistance and hardness resulting from porosity limit the usefulness of RBSN in high performance applications.

Recent work [53-56] on nitrided, high purity laser synthesised silicon has shown that a finer microstructure can be achieved, which is more oxidation resistant, has a higher strength (MOR 435±120 MPa) and requires lower nitridation temperatures and times than conventional RBSN. The higher strength derives from the low flaw size compared to the conventional material, and the small pore size reduces the penetration of oxidation from the surface to the bulk. The powder is produced by the thermal decomposition of silane

(SiH_4) with a CO_2 gas laser, resulting in a small starting particle size (140-260nm). This allows an efficient packing density, and gives a much finer microstructure and smaller pore size than the conventional material. Of particular interest is the low nitriding temperatures and times necessary for full conversion of Si to Si_3N_4, a 10 min, 1250°C cycle has been demonstrated to give >99% conversion. The improved nitridation reaction kinetics are thought to be due to a Si-H layer on the surface of the Si particles from the laser synthesis process. This is within the temperature capability of Nicalon and Tyranno fibres, provided a method of infiltrating the fibre preform could be found. The difficulties of producing the silicon powder in larger quantities (at present a laboratory scale process), and handling without agglomeration have to be addressed before significant progress can be made.

Dense silicon nitride

Silicon nitride may be sintered to close to its theoretical density ($3.2gcm^{-3}$) by the addition of metal oxides which react with silica on the surface of the starting powder, and with the silicon nitride itself to form a glass, allowing liquid phase sintering. The process may take place at ambient pressure (pressureless sintering) or under high pressure (hot pressing or hot isostatic pressing). MgO was an early additive used, the sintering temperature being 1500°C-1700°C. Dissociation of the Si_3N_4 occurred at the higher temperatures, which was solved by sintering compacts within Si_3N_4 powder beds, locally increasing the partial pressure of nitrogen, and suppressing the dissociation reaction. The starting powder has to contain a high proportion of α-Si_3N_4 (often produced by the nitriding route), which dissolves in the glass formed by the additive, and reprecipitates on

the remaining β-Si_3N_4. The glass remaining at the grain boundaries is the main factor determining the high temperature properties, while the elongated prismatic morphology of the precipitated β grains gives a relatively high fracture toughness. Trivalent cations such as Y^{3+} form glasses with lower mobilities than divalent cations such as Mg^{2+}, and tend to give enhanced mechanical properties at high tempertures, as the grain boundary glass is more viscous. In addition, by careful control of the starting powder purity and quantities of additive used, it is possible to recrystallise the grain boundary glass, improving the refractory properties of the material further. In the case of Y, some secondary phases formed in this way are sensitive to oxidation, a volume change occurring. This can lead to disintegration of the material, so the phases formed must be carefully controlled to obtain an optimised material. The viscosity of the Y based glass is high, and full density cannot be achieved without the application of external pressure. Al_2O_3 may be added to the starting powder, lowering the Si_3N_4-Y_2O_3 eutectic temperature, allowing densification to take place by pressureless sintering. It was found that Al^{3+} and O^{2-} could substitute for Si^{4+} and N^{3-} in a solid solution of limited solubility based on β', a modification of the β-Si_3N_4 structure. The charges remain balanced, and no vacancies need be introduced into the structure. In the case of aluminium substitution, the compound has a generic formula of $Si_{6-x}Al_xO_xN_{8-x}$, where x is continuously variable up to a limit of 4.2 [57], and is known as a β' SiAlON.

A variation on the sintered Si_3N_4 theme is sintered reaction bonded silicon nitride (SRBSN) in which silicon powder is mixed with α-Si_3N_4 powder and the appropriate additives and nitrided prior to the final sintering stage. This has the advantages that the nitrided material may be machined to close to the required shape, having a low abrasion resistance compared to the sintered product, and the degree of shrinkage experienced

during sintering is low because the presintering density is higher than could be achieved by cold pressing. The sintering process may take place without external pressure being applied, in which case the material may be referred to as nitrided pressureless sintered (NPS).

2.6 SiC Fibre Selection and Properties

Textron SCS-6 fibre - Structure

The SCS-6 fibre is one of a range of CVD SiC fibres produced by Textron primarily for use in metal matrix composites (MMC's) but which have properties that make them attractive for use in CMC's. The fibre is produced [58] by the decomposition of silanes to produce SiC onto a resistively heated carbon core. The core is 33μm in diameter and is prepared for deposition of SiC by coating with a 1μm layer of pyrolytic carbon. The silanes are diluted with argon and hydrogen to the desired concentration and deposition takes place at 1300°C (the morphology and structure of the SiC is dependant on the temperature and gas concentration/flow rate amongst other things). The SiC is deposited in the β form in a columnar orientation, such that their [111] axis is parallel to the condensation direction. The SiC sheath produced has a distinct 2 zone structure [58,59,60], the inner zone having a grain size of 50nm changing to 100nm at a radius of around 40 μm. After the SiC sheath is deposited, one or more outer layers are deposited, which have the effect of increasing the strength of the fibre, typically from 2.1 GPa to 4 GPa. The mechanism for this improvement is thought to be sealing of the exposed SiC grain boundaries by the surface layer, preventing them from acting as stress raisers. In addition

to increasing tensile strength, the surface layers can be tailored in composition and structure to suit the desired matrix. The SCS-6 fibre has a twin carbon layer, approx. 3μm thick overall, deposited on the SiC sheath, with a silicon rich zone between these two layers. The structure of the fibre is shown in fig 2.9 below.

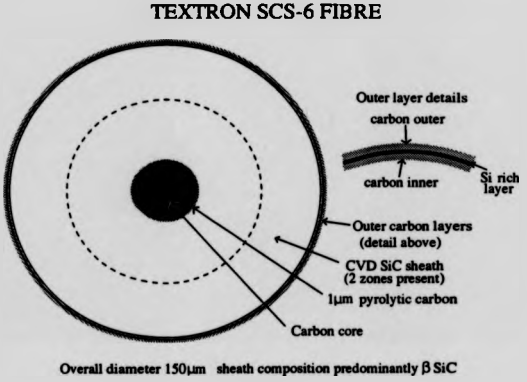

fig 2.9 Structure of SCS-6 fibre

SiC is one of a number of crystalline substances that exhibits polymorphism, that is, a layered arrangement of atoms to give a variety of structures, although the nearest atomic neighbours are the same. The basic unit of the structure is the SiC_4 or CSi_4 tetrahedra, stacked in close packed structures. The simplest is the cubic 3C structure, which is also known as β-SiC, the hexagonal wurzite structure (6H) is denoted α-SiC. Polytypism occurs when mixed layers of hexagonal and cubic repeat in one dimension.

Textron SCS-6 Fibre - Properties

The mechanical properties of SCS-6 fibres are excellent at room temperature, the average strength of a batch being 3.8 GPa (50mm gauge length) [23]. This may vary between 3.5 and 5.5 GPa (40mm gauge length) [59]. Retention of strength after high temperature exposure in oxygen and argon is shown in fig.2.10 [59] below. The retention of strength after exposures up to temperatures of around 1500°C for 30 minutes makes the fibre attractive for use in sintered ceramic matrix composites as processing temperatures and times may be similar to this. The reduction of strength with test temperature is shown in fig.2.11 [59] below.

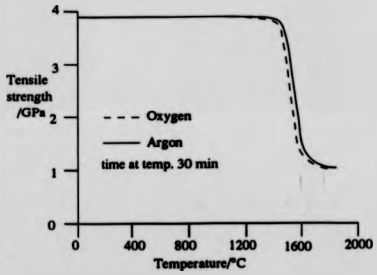

fig.2.10 Effect of high temperature exposure on SCS-6 fibre

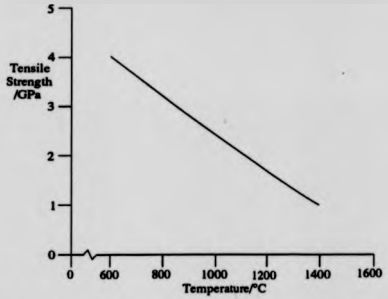

fig.2.11 Variation of strength with test temperature of SCS-6 fibres

The reduction of strength with test temperature is thought [59] to be due to a small amount of free silicon at the β-SiC grain boundaries, allowing sliding at temperatures above 600°C and structural changes within the fibre above 1200°C. Evidence for this free silicon comes from thermal expansion studies, in which a hysteresis is observed in the axial thermal expansion around 1350°C, corresponding to a strain decrease of 0.04%. This is consistent with the expected volume decrease of silicon at around 1400°C on melting, with a volume fraction of 1% free silicon [59]. The fibres exhibit creep as low as 1180°C, again indicative of free silicon present, anelastic (recoverable) creep occurring at temperatures below 1400°C; the creep behaviour at a constant stress of 278MPa at different temperatures is shown in fig.2.12 [59]. The controlling activation energy for creep was found to be 480±20kJmol^{-1}, which is in good agreement with the activation energy for self diffusion of silicon.

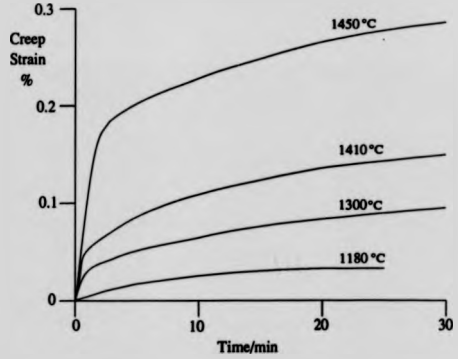

fig.2.12 Creep of CVD SiC fibres at a stress of 278MPa

The modulus of the CVD SiC fibres (SCS-0, the uncoated version of SCS-6 was used in the experiments) was investigated by dynamic means, and by static means at high temperatures [59]. A linear decrease in modulus with temperature was found, the scatter in the static test data making the higher temperature modulus less certain. A baseline room temperature tensile modulus of 391GPa was measured, and 414GPa in flexure, the lower modulus core being primarily responsible for the lower value recorded in tension. At 1000°C, the tensile modulus decreases to approx. 95% of the RT value, with a similar reduction for flexural modulus.

The large diameter of the SCS-6 fibre makes it unattractive for use in complex components, where the bend radius is restricted to 20mm or so. Nicalon fibres (Nippon Carbon Company, Tokyo, Japan) have a small diameter (10-15μm) and are available commercially based on the thermal decomposition of organometallic polymers containing silicon [17-19,61]. Dimethyldichlorosilane $(CH_3)_2SiCl_2$ was converted to polydimethylsilane by dechlorination with sodium, with was pyrolysed at 400°C under inert atmosphere to give a polycarbosilane with the structure:-

This polymer has an average molecular weight of 1200 and can be melt spun into a fibre. The spun fibre is subjected to various heat treatments up to 1200°C in order to convert it to predominantly β-SiC, with small amounts of oxygen [19]. The resulting fibre has a strength of 2.62 GPa, and a Youngs Modulus of 193 GPa [62], although its properties are rapidly degraded at temperatures above 1200°C [18], and even 1000°C may be damaging in long term exposure, depending on environment. The degradation process appears to involve loss of carbon monoxide (CO) from the fibre, together with coarsening of the β-SiC grains [18,19]. This restricts the process route for the matrix to 1200°C, although short excursions to around 1300°C may be permitted. The Tyranno fibre (UBE Industries Ltd, Tokyo, Japan) is made in a similar way to Nicalon, but has a small quantity

of titanium present, which stabilises the excess carbon present by forming TiC giving a slight improvement in high-temperature properties. Glass matrix composites based on the Pyrex composition and others have been demonstrated, and work is in progress to develop higher temperature capability glass ceramic matrices. The CVD process used to manufacture the SCS-6 fibre may be used to create a matrix in situ in a Nicalon or Tyranno fibre preform, as the temperature at which deposition takes place is low enough for the fibre to survive. This has been achieved with SiC, giving a SiC/SiC composite and the material is available commercially (SEP). CVD Si_3N_4 could also be used (little appears in the literature), however for silicon nitride matrices, the well developed hot pressing and pressureless sintering compositions involve temperatures that are too high. Reaction bonding has been used to create a matrix as mentioned previously [29], but little work has been done in this area.

Although not a SiC fibre the HPZ Si_3N_4 by Dow Corning is of interest as a high temperature capability fibre for use in a Si_3N_4 matrix. Made by a similar route to Nicalon and Tyranno using melt spun hydridopolysilazane, the strength (1.73-2.07 GPa) and modulus (179-235 GPa) [63] makes it attractive for use in many CMC's. Preliminary structural work [64] on the HPZ fibre showed that it contained Si, N, C and O (in order of abundance) and was an amorphous structure based on the SiN_4 tetrahedron. Stability is claimed [64] to be retained up to nearly 1400°C, and a feature of the fibre is its dielectric constant of 5.5-6.5 and high electrical resistivity (>10^7 Ω) [63].

2.7 PROGRAM OBJECTIVES

The objectives of the program may be summarised by the following :-

1. To develop a ceramic matrix composite to operate in excess of 1000°C, using Silicon Carbide fibres in a Silicon Nitride matrix.

2. To explore different matrix processing and constitutional options to provide a suitable protection for the fibres during service (i.e. to prevent oxidation/corrosion damage), and assess the effect of processing on fibre integrity

3. To evaluate the mechanical properties of the composite at room temperature and at elevated temperature, and to investigate mechanical properties after elevated temperature exposure. In addition, to investigate micromechanical properties at room temperature of virgin material and oxidised material.

4. To investigate general physical properties (e.g. density, coefficient of thermal expansion etc).

5. To investigate the microstructure of composite, and attempt to relate this to the mechanical/physical properties

6. To evaluate creep/stress rupture behaviour.

7. To study the applicability of the composite in the production of complex shapes and to assess the overall suitability of the material for use in the gas turbine engine.

3.0 EXPERIMENTAL TECHNIQUES

Composite samples were analysed using a number of techniques, the later SiC/SRBSN specimens being more completely characterised than earlier SiC/RBSN specimens. Microstructure was investigated using scanning electron microscopy (SEM) and transmission electron microscopy (TEM). X-ray diffraction was used to analyse the quantity of residual silicon in RBSN matrices, to check for α to β conversion in the SRBSN matrices and for phase identification. Mechanical testing was carried out in flexure at room temperature and at elevated temperatures, a small amount of creep/stress rupture and tensile testing being done at the end of the program of work. In addition to the macromechanical testing, micromechanical measurements of the fibre/matrix interfacial shear strength were carried out. Density, coefficient of thermal expansion and fibre volume fraction were additional techniques used.

At the time when the work was carried out, some of the machines used for analysis were interfaced with computers, to improve the storage, analysis and presentation of data. As a result, several programs were written either to collect data as it was generated, or to analyse collected data.

The composite preparation techniques developed during the program of work are described in chapter 4.

3.1 Scanning Electron Microscopy

Specimen Preparation

The composite microstructure was characterised by scanning electron microscopy (Cambridge S250 and JEOL 6100), and an associated X-ray elemental analysis system (LINK EDAX AN10000 on the S250). Samples were sliced using either a coarse Tyrlide diamond saw or for delicate/small specimens a Capco annular diamond saw. They were

then mounted in either conductive bakelite or MetSet polyester resin for the porous/ delicate samples. Grinding and polishing was mainly carried out on a Buehler Metaserv machine, using 70μm, 30μm, 6μm and 1μm diamond grit (bonded to the wheel in the case of the 70μm grit size). In some cases, silicon carbide paper was used for coarse stages although the hard SiC/Si_3N_4 composites quickly smoothed the paper surface. The samples were coated using sputtered gold to prevent charging in the microscope, with graphite loaded conductive cement used to improve conductive paths when using MetSet resin. In the case where a rough surface was to be imaged (e.g. a fracture surface) the sample was attached to an SEM mounting stub using graphite cement and then coated with sputtered gold in the usual way.

SEM Imaging

The SEM imaging modes used were secondary electron imaging, backscattered electron imaging, and elemental X-ray mapping. Secondary electrons gave topographic images, the depth of field allowing a detailed view of complex fracture surfaces etc. Backscattered electrons gave atomic number (z) contrast, high z elements being light in contrast and low z elements being dark. This allowed the imaging of silicon nitride β grains (dark contrast) with an yttrium containing grain boundary glass (light contrast).

X-rays emitted with energies characteristic of the elements present were used to produce maps of different elements and to analyse the composition of secondary phases in the silicon nitride matrix. The X-ray energy dispersive (EDS) detector (a LINK LZ5) was normally protected from contamination by a thin beryllium window, but to detect elements lighter than sodium (e.g. N, O, and C) this was removed because of X-ray absorption <1keV. Mapping of carbon, nitrogen and oxygen at the fibre matrix interface was carried out using this method. Quantitative analysis by peak height comparison of the heavier elements X-rays (energies >1keV) was carried out to determine the compositions of phases present using the LINK AN1000 system. The method could not be extended to the light

elements as corrections for absorption and fluorescence are difficult to apply for X-ray energies <1keV.

3.2 Transmission Electron Microscopy

Specimen Preparation

The transmission electron microscope has been successful in determining the microstructure of many new materials to the extent of imaging individual planes of atoms. The advantages of the technique are balanced by the difficulty of preparing samples, as the thickness of the sample has to be less than 200nm thick to allow a good electron image to be obtained. The weak interfacial bonding between fibre and matrix in the materials investigated made the application of the technique limited, however the matrix material was investigated to show that it had a similar microstructure to related silicon nitrides described in the literature. The microscopes used in the TEM work were a JEOL 100C operated at 100kVand a JEOL 2000FX operated at 200kV. X-ray EDS analysis was carried out on the 2000FX using a LINK AN10 with an LZ5 detector.

Preparation of a transverse sample was carried out by cutting a slice of the material (using the annular diamond saw) to a thickness of about 0.4mm. The sample was held in a brass tube 3mm o.d. by epoxy resin during this operation, which remained as a brass ring supporting the sample. The slice was then mechanically thinned on 1200 grit SiC paper to approx. 150μm before argon ion beam thinning. Cyanoacrylate glue ('Superglue') was used to hold the fibres in place during this operation, the low viscosity of the glue allowing it to penetrate the gap between the fibre and matrix. This is necessary because the fibre/matrix interfacial bonding in the composites investigated was very low, and fibres were debonded easily during mechanical grinding of thin sections. Argon ion thinning was used to thin the samples so that areas were electron transparent. 5 keV ions are used, at an angle of 30° or less to the plane of the sample disc, the rate of thinning being dependant on ion energy and angle. Longitudinal samples were prepared by cutting thin slices with the annular saw, and

grinding them to approx. 250μm thick on 1200 grit silicon carbide paper. A copper support ring was then glued onto the slice using epoxy resin, and overhanging edges of the slice broken off with a new razor blade. The sample was dimpled using a South Bay Technology Inc. model 515 dimpler, producing a shallow depression in the centre and argon ion thinned in the usual way. A problem that occurs during thinning of composite materials is the preferential thinning of different phases. In the case of CVD SiC fibres in a dense Si_3N_4 matrix, the SiC fibres tended to thin at a slower rate than the matrix. This problem may be overcome if the beam angle is reduced, however physical constraints within the goniometer used to mount the specimen, and the reduced thinning rate with angle limits this approach.

TEM Imaging

The principal contrast modes used were absorption and diffraction of electrons. Absorption contrast arises from incoherent scattering from amorphous and crystalline regions via the absorption law

$$I=I_0 e^{-\sigma t} \qquad (3.1)$$

where σ is a function of atomic number, and t is the specimen thickness. Diffraction contrast arises from coherent scattering of electrons from crystals within the specimen, conventional dark and bright field imaging modes were employed.

Tilting the specimen caused variations in contrast of crystalline areas, whereas in amorphous areas, contrast remained constant, as electrons are not scattered at sharply defined angles. This was used to identify amorphous areas (such as glassy grain boundary phases) within a predominantly crystalline sample

The electron diffraction mode was used to obtain diffraction patterns of crystals, and diffraction patterns were obtained for β-Si_3N_4 crystals to allow measurement of lattice

constants. Selected area diffraction (SAD) was used to obtain most of the diffraction patterns, using an aperture to select diffracted electrons from a single crystal. Microbeam diffraction was also used for obtaining patterns from crystals that were significantly smaller than the SAD aperture.

X-ray emission from the sample was analysed in a similar way to the SEM EDS analysis, a feature of the TEM being its ability to focus the electrons onto a very small area, allowing the analysis of grain boundary glasses at triple points.

3.3 X-ray Diffraction

The X-ray diffraction technique was used to find the relative phase concentrations in the Si_3N_4 matrix, initially for RBSN, where the principal concern was the presence of residual silicon after the nitriding phase, and later for the hot pressed SRBSN matrix to monitor the α to β transition. The technique was also used to identify any crystalline grain boundary phases or oxidation products present either in the bulk or on the surface of samples

Samples were usually analysed after processing had been completed on tiles of material. The surface was cleaned using a vapour blasting unit, and ground on 400 grit silicon carbide paper (in the case of RBSN, samples were ground on silicon carbide paper only). For analysing bulk materials, samples were crushed in a mortar with a pestle to a powder and pressed into a shallow aluminium holder. Two X-ray diffraction machines were used, a Philips PW1130/00 with a chart recorder was used for the bulk of the work and a Philips PW1050/80 with a Hiltonbrooks control system connected to an IBM PC for data recording. Both machines used copper K_α radiation, the PW1050/80 having a nickel filter to remove the Cu K_β peak.

The phases giving rise to the peaks observed were identified using the JCPDS file cards on microfiche, their references are listed in table 3.1. The method for analysing diffraction data in relation to relative phase concentration in RBSN has been studied previously [65],

and the method used in the present work was based on this. Peak heights were measured with a ruler, and normalised by multiplying each peak height with an appropriate constant (obtained from [65]) and then averaging normalised peak heights for each phase. The ratios of average normalised peak heights were then calculated and calibration curves [65] were then used to find the weight percentage of each phase. The α-Si_3N_4 peaks used were (101), (110), (200), (201), (102), (210) and (301). The β-Si_3N_4 peaks used were (110), (200), (101) and (201), and the Si peaks used were (110) and (220). Since the reduction of the raw data to the ratios of average normalised peak heights involved repetitive calculation a short computer program was written in BBC BASIC.

Phase	JCPDS ref.
Silicon Nitride (α) (Si_3N_4)	9-250
Silicon Nitride (β) (Si_3N_4)	33-1160A
Silicon (Si)	27-1402
Silicon Carbide (β) (Cubic, SiC)	29-1129
Boron Nitride (Hexagonal, BN)	34-421
Silicon Oxynitride (Si_2N_2O)	18-1171
Yttrium Disilicate α ($Y_2Si_2O_7$) β	21-1457 22-1103
Yttrium Silicate (Y_2SiO_5)	21-1458

table 3.1 JCPDS references for phases analysed

3.4 Mechanical Testing

Mechanical testing was carried out mainly on an Instron 1122 testing machine, although an Instron 4505 at the Rolls-Royce Advanced Ceramics Centre was used for a small proportion of the work. A BBC microcomputer was attached to the 1122, using the computer's analogue port via an interface to read a 0-10 volt output from the 1122 chart

recorder. A program was written to log the load data during a test, and together with test details (crosshead speed, load range etc) store it on floppy disc. This data was then transferred to an Acorn Archimedes A410/1 machine to allow analysis, and plotted on the attached laser printer. Data from many tests were collected and analysed by this technique, and stress/deflection curves incorporated into documents produced on the Archimedes. All the software was written in BBC BASIC.

A small amount of test development was necessary to allow the use of the samples that could be produced in the hot press (max length <50mm), samples being tested at room temperature and elevated temperature in flexure, and in tension at room temperature. A four point bend jig was produced by machining pieces of alumina tube, and using sintered SiC rods 6mm in diameter to load the sample. The jig (fig. 3.1) was enclosed in an existing furnace adapted for use with the 1122 load frame, water cooled brass end pieces were used to attach the alumina tubes to the crosshead and load cell. It was found necessary to place an aluminium shield above the furnace to protect the crosshead and upper part of the load frame at the higher test temperatures (>1200°).

The maximum stress in the sample was calculated using the standard equation for four point bend

$$\sigma = 3P(L-l)/2bd^2 \qquad (3.2)$$

where P is the overall applied load (P/2 on each loading roller or knife edge), L is the outer loading span, l is the inner loading span, b is the specimen width and d is the specimen depth. In the three point bend case, the inner loading span is zero, giving

$$\sigma = 3PL/2bd^2 \qquad (3.3)$$

The disadvantages of the bend test is that only a small volume of the sample is at the maximum stress. This may have the effect of raising the apparent strength of the material because the probability of a critical flaw being present within the stressed region of the sample decreases as the size of the stressed region is reduced. Methods of treating bend

test data to take volume effects into account are discussed in [9]. The result may also be influenced by the surface condition of the sample. This is important for ceramics because surface flaws (induced by sample machining etc.) can cause failure of the sample at a lower stress than the bulk material would fail at.

The main advantages of bend testing are that the samples are easy to prepare, do not use much material (which may only be available in small size plates), and the testing alignment is not very critical (compared to tensile testing).

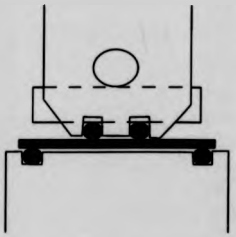

fig. 3.1 High temperature, four point bend jig

Creep and stress rupture testing was carried out in existing creep rigs, with specimen deflection being logged on a chart recorder. Load was applied via a 10:1 lever system to an alumina push rod, which transferred load to the sample using silicon carbide rollers held in an alumina fixture, the general arrangement of the loading jig is shown in fig.3.2. Prior to loading a sample into the rig, it was cleaned ultrasonically in IPA to remove contamination from fingerprints etc. Specimen deflection was measured using an LVDT attached to the loading push rod, the output from the LVDT being processed by a conditioning unit. The chart recorder output was converted to specimen deflection (the LVDT having been calibrated using feeler gauges) and the data analysed using the procedure outlined in [66]. Deflection rate (when the creep deflection curve had become approximately linear) was

plotted against applied load on a log/log plot. The slope of the line obtained was taken as the stress exponent N, and the equivalent sample strain (in the outer fibre) was calculated using equation 3.4 [66].

$$\varepsilon_{max} = \frac{2h\,(N+2)}{(L-a)\,[L+a\,(N+1)]}\, y_L \qquad (3.4)$$

where h= height of specimen, L= outer support span, a= inner loading span and N=stress exponent. The equivalent stress was calculated using equation (3.5) [66].

$$\sigma_{max} = \frac{3P(L-a)}{2bh^2}\,\frac{(2N+1)}{3N} \qquad (3.5)$$

where P=applied load, b=width of sample, h=specimen height, L=outer span, a=inner span and N is the stress exponent.

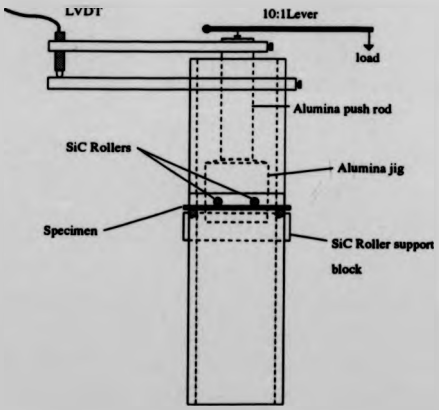

fig.3.2 Creep rig loading arrangement

A few samples were tested, in tension. This was desirable from the point of view of fracturing the material in a simple uniaxial stress field, to compare the material to the various models proposed for the mechanical behaviour of CMCs. A profile was ground in both the edges and the faces of a 50x5x2mm bar (nominal dimensions) sliced from a 50x50mm tile to give a dog-bone shape. This was then glued using high strength epoxy resin into aluminium end tabs, as shown in fig.3.3, which were then held in the 1122 tensile test grips. Room temperature testing was done in a simple brass fixture, with silver steel rollers, in three point bend.

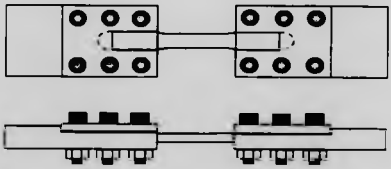

fig. 3.3 Tensile test piece with epoxied aluminium grips

3.5 Micromechanical testing

The behaviour of the fibre/matrix interface was investigated using an indentation technique described by Marshall [67], and subsequently used in investigations of composites similar to that studied in the present work [68]. The principle of the test technique is to indent the end of a fibre in a mounted and polished section of composite using a Vickers indenter, in order to debond the fibre and push it through the sample. A schematic diagram is shown in fig. 3.4.

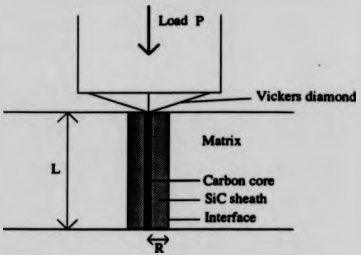

fig. 3.3 Interfacial measurements by indentation

The interfacial shear stress can be calculated by the equation

$$\tau = P / (2 \pi R L) \qquad (3.6)$$

where P=load on indenter, L=thickness of sample, R=radius of fibre (75μm).

The method of testing was to put different loads, e.g. 400g, 600g, 800g, 1000g etc, keeping a record of the load applied to each fibre. After indenting with approx. 10 indents per load, the sample was examined in the SEM for evidence of debonding, the results being plotted as a histogram of percentage of fibres debonded against load. A weakness of the technique is the difficulty of applying the loads in consistent way, and in addition, the fibre/matrix bonding is low enough to allow debonding during the grinding and polishing of the specimens prior to indenting. A new system, being developed by A. M. Daniel et al, will allow the indentation to be carried out in a controlled and repeatable way in situ in the SEM chamber, using a piezoelectric actuator with a load cell and indenter attached. The indentation process will be able to be visually monitored and a load/time (load/deflection at a constant indenter speed) graph produced.

3.6 Acoustic Emission

A small amount of acoustic emission work was done during room temperature mechanical testing of samples. A piezoelectric transducer was held onto the samples by masking tape or by a rubber band with an ultrasonic coupling jelly between the transducer and the sample, and events counted in a 0.1s window using a Dunegan/Endevco acoustic emission analyzer (amplifier model no.302A, counter model no.303, reset clock no.402). There was no attempt to characterise the emissions by their energy, only by their rate, correlating this with features in the load/deflection or stress/deflection curve. The rollers in the 3 point bend test jig were sprayed with PTFE for one series of tests to try to reduce the frictional contact noise between the sample and the rollers. The emission rate was recorded using a channel on the BBC computer connected to the Instron test machine as a number proportional to the rate, using the same software as for the load level recording.

3.7 Miscellaneous Characterisation Methods

The samples produced were also characterised by measuring density, fibre volume fraction and thermal expansion.

Sample density was measured using Archimedes method, in trichloroethane and in water for some specimens. Trichloroethane was chosen for its wetting capabilities and its slightly higher density than water (1.337 gcm^{-3}), thereby giving a greater weight change when the specimens were immersed in the solvent. The principle of the test is to measure the weight of a sample in air, and when immersed in a liquid, the density being given by (3.7). With the balance used for the bulk of the tests, it was necessary to use a thin copper wire to suspend the sample in the liquid used. This introduces a small error, however, with the mass of the samples measured this error was negligible.

$$\rho = \frac{\rho_{solvent} \times \text{weight in liquid}}{\text{weight in air - weight in liquid}} \qquad (3.7)$$

Fibre volume fraction was measured by counting fibres in an optical low magnification photograph of the microstructure in a given area, the volume fraction being given by

$$V_f = \frac{\text{number of fibres x area of one fibre on photograph}}{\text{total area of composite on photograph}} \qquad (3.8)$$

where the area of one fibre is given by

$$\text{area} = \pi (d/2)^2 \qquad (3.9)$$

(d=average diameter of a fibre as measured on the photograph)

The number of fibres in a typical section measured was 100.

Thermal expansion was measured using a Netzsch dilatometer connected to a BBC microcomputer, the data being stored on floppy disc and subsequently processed on an Archimedes A410/1. Alumina standards were run to determine the error inherent in the dilatometer as a function of temperature, the data obtained being used to correct the expansion data for the SiC/SRBSN samples.

4.0 SYSTEMS STUDIED AND FABRICATION TECHNIQUES

In the course of this program of work, a number of processes and materials have been developed. Material processes investigated were slip preparation and tape casting, filament winding and prepreg preparation, nitriding and hot pressing; some development of existing techniques was necessary. After the work reported by Bhatt [23-27], a reaction bonded silicon nitride matrix was investigated, and was developed into a dense, sintered reaction bonded matrix. Methods of reducing the nitriding temperature with a view to incorporating Nicalon fibres in it were investigated, using transition metal additives, and the HPZ fibre by Dow Corning [63,64,69] was put into a reaction bonded silicon nitride matrix to determine its ability to withstand nitriding conditions.

4.1 Composite Fabrication

4.1.1 Slip preparation and tape casting

A typical SRBSN matrix was prepared using silicon powder, silicon nitride powder and the liquid phase sintering additives (Y_2O_3, Al_2O_3 etc), which were ball milled in trichloroethane for 24 hours. The milling medium (HIPped Si_3N_4 pellets) was removed, the solvent evaporated and the mixture passed through a 1mm sieve . For the early work on RBSN matrix composites, "as received" silicon powder was used without milling.

A slip or slurry was made for tape casting the matrix either on its own, or onto aligned fibres. The powder (milled if applicable) was mixed with trichloroethane, ethanol, a binder (Du Pont 5200 MLC binder dissolved in MEK), a surfactant (ICI KD1), and a plasticiser (Monsanto Santicizer 160, Butyl Benzyl Phthalate). After mixing by hand, the slip was transferred to a high shear mixer to break down agglomerates and then de-aired in a partial vacuum. This method was later superseded by mixing the starting powders, the binder and solvents etc. and ball milling for 24 hours. This had the advantage of eliminating the

drying/sieving stage (which was prone to introduce agglomerations) and avoiding high shear mixing. The binder system was previously used in the production of tape cast glass ceramic substrate materials by Dr. E.Logan (formerly of the University of Warwick).

The tape casting process is shown schematically in fig. 4.1, the slip being cast on to a flat sheet of Mylar film on a flat bed casting machine, or on to fibres wound on a drum (4.1.2)

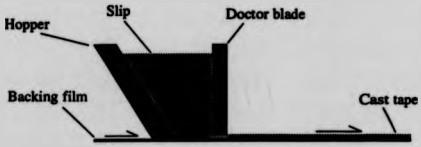

fig 4.1 Schematic view of tape casting process

The slip was poured into a hopper after mixing, de-airing etc., and the backing film moved underneath in the direction shown. The doctor blade position was adjustable allowing the thickness of the cast tape to be varied. The tape was then dried (24 hours at room temperature) and carefully removed from the backing film. A scalpel was used to cut the tape to the correct shape for further processing, the typical thickness of the dried tape was 0.3-0.5 mm dependent on the solvent content of the slip and the height of the doctor blade.

Earlier work on binders such as polyvinyl alcohol (PVA) and polyethylene oxide (PEO) gave inferior results, and they were abandoned. The quality of the finished tape or prepreg was found to be critically dependent on the techniques used in slip preparation, and much effort was put into refining slip compositions and processing methods to obtain satisfactory finished material. Problems encountered in tape casting included agglomeration of powder (particularly Si_3N_4), "mudflat" cracking during drying, bubbles of air or solvent vapour appearing in the cast tape, difficulty in separation from the backing film and poor

mechanical properties after separation from the backing film.

4.1.2 Filament winding and Prepreg Preparation

Green prepreg material was produced by winding the SCS-6 fibre on to a drum with a Mylar backing film. The filament winding machine (fig.4.2) was designed to allow sheets of prepreg of dimensions up to 400mm x 110mm to be produced, a suitable tape casting hopper being made to fit above the drum. The carriage was originally run from a separate motor drive to the drum, however a later modification using a belt drive from the drum shaft was incorporated to make the fibre spacing more reproducible. Changes in fibre pitch on the drum could be made by changing the pulleys driving the carriage.

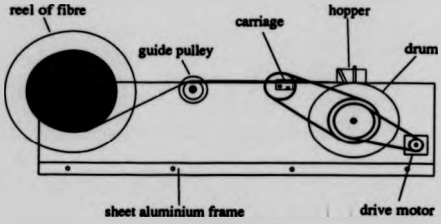

fig.4.2 Filament winding machine

A piece of Mylar film was cut to fit the drum, and held in place with tape during winding of fibre. Matrix material in slip form was then cast over the wound fibres by pouring it into the hopper above the drum. It was allowed to dry, and removed from the drum by cutting the fibres with a sharp edged wheel (the drum had a 1mm x 1mm slot machined into the surface to guide the wheel, see fig.4.3). Tape was stuck to the prepreg on either side of the slot to prevent splitting as the fibres were cut. The backing film was

easily removed from the prepreg, but the prepreg was found to be fragile, and had to be handled carefully. Cutting the prepreg was a problem with the SCS-6 fibres used because they could not be easily cut except by bending around a small radius, and the prepreg was easily damaged. The method adopted was to make a cutting jig (fig.4.3), similar to a sheet metal bending jig, which firmly gripped the prepreg as it was sharply bent along a line. This was found to be adequate, although time consuming to use.

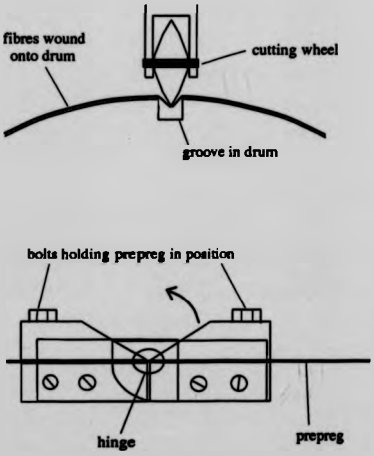

fig 4.3 Prepreg cutting methods

To produce composite tiles, eight sheets of prepreg 50mm x 50mm were cut out and stacked. Three sheets of tape cast matrix material were placed either side of the stack to allow surface machining after completion of the processing.

4.1.3 Hot Pressing and Nitriding

The processing of the matrix to form silicon nitride was done in one or more steps, depending on whether RBSN or SRBSN was being formed. The first trials to produce an RBSN matrix composite utilised a warm pressing stage followed by nitriding in a furnace. Later RBSN matrix samples were hot pressed at 1150°C in a graphite die to remove the binder and partially sinter the silicon matrix prior to nitriding. SRBSN matrix composites were produced by hot pressing at 1200°C, nitriding and then a final hot pressing at 1700°C to densify the reaction bonded matrix.

Nitriding was initially carried out in a small (38mm inner diameter) tube furnace, a larger furnace was then constructed with a 100mm inner diameter. A mixture of nitrogen and hydrogen was used, early experiments using separate bottles and later ones using premixed bottles. 95%/5% or 90% nitrogen/10% hydrogen mixtures were used for most of the experiments, the premixed gases simplifying the furnace gas arrangement, and making the nitriding atmosphere more reproducible.

Samples were placed on pieces of scrap silicon nitride or composite in alumina boats to minimise contact contamination. A nitriding cycle (fig.4.4) was developed which gave good results early in the program, and was then used for most of the later work. The nitriding mixture flow rate was kept constant during the cycle, the rate for the larger furnace being approximately 150ml/min.

Hot pressing was carried out in a graphite die producing a square tile of side 50mm. The die surfaces were painted with a boron nitride slurry to act as a release agent, as silicon powder reacts with graphite to form SiC. The die was placed onto an insulating base, and surrounded by a box containing bubble alumina. A hydraulic actuator forced a ram down onto the die to apply pressure, the typical die pressure during final pressing being 20MPa. The die was heated by induction heating using a 450kHz R.F. generator (Radyne Ltd.), the typical power input to the die being 12kW. The hot press assembly is shown schematically in fig.4.5.

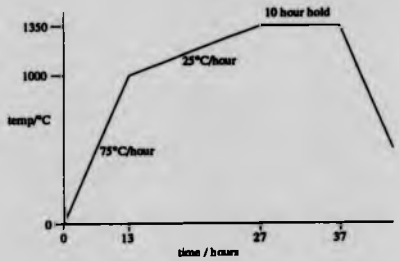

fig.4.4 Nitriding cycle for large furnace

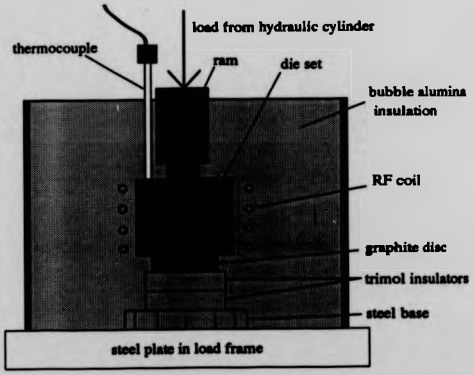

fig.4.5 Hot press assembly, schematic view

4.2 Materials Fabricated

4.2.1 SiC/RBSN

The first composite system studied was SiC/RBSN as there was an established preparation method and the material had been characterised [23-27]. Nitriding experiments were carried out on small pressed pellets of silicon powder to establish the nitriding cycle in the small furnace. The silicon powder used throughout the program was KemaNord grade 4E Sicomill. Early samples had a residual silicon content of 3.5% (measured by XRD), although it was found that reproducible nitriding was difficult because the furnace control system was unreliable. The tape casting process was then investigated using silicon powder and a binder/plasticiser/solvent system previously developed for use with glass ceramic substrates. Difficulty was experienced in removal of the tape from the backing film but sufficient tape was produced for laminating experiments using SCS-6 fibres. Warm pressing gave good results with monolithic tape, but when fibres were placed between sheets of tape and warm pressed they failed to laminate together. Cold pressing fibres and powder gave better results, and a plate produced in this way was nitrided. The matrix produced was satisfactory, but this process did not represent a realistic way of composite production.

Casting of a matrix slip (Si powder, binder,solvents etc.) onto aligned fibres was used to produce a prepreg, sheets of which were successfully laminated by warm pressing and then nitrided. Improvements in nitriding gave residual silicon content of <1.5%. Moderate success was achieved with these materials, with simple three point bend tests and SEM studies of fracture surfaces and polished sections. Improvements in the furnace control and gas supply systems improved nitriding, and the residual silicon content of later materials was typically <1.5%.

Following the laminating methods reported by Bhatt et al [23-27], later materials were produced by hot pressing prior to nitriding, which gave improvements in lamination, and a

number of samples were made to allow mechanical testing and environmental exposure.

Dow Corning HPZ fibre was incorporated into an RBSN matrix to investigate its ability to withstand the nitriding process. Prepreg was made by dipping tows wrapped on a square wire frame into a slurry of silicon with a polyethylene oxide binder dissolved in distilled water (this binder system has been used successfully for glass matrix composites using Nicalon fibres). The prepreg was stacked and pressed between warm (100°C) aluminium platens under a load of approx. 59MPa and nitrided using the standard cycle. Two bend specimens were cut from the plate produced and tested mechanically, and the fracture surface was examined in the SEM.

4.2.2 Nitriding aids for RBSN

The small diameter fibres Nicalon and Tyranno are attractive for use in an RBSN composite, however the maximum nitriding temperature needed to convert the silicon to silicon nitride (1350°C) causes irreversible damage to the fibre (as discussed previously). A NASA report [70] on thermogravimetric and differential thermal analysis in nitrogen of samples of silicon powder containing a number of transition metal oxide additives indicated that NiO and MnO_2 were most likely to reduce nitriding temperatures, and a series of experiments were conducted using these oxides. Four silicon powder samples containing 0.5%, 1%, 5% and 10% of each oxide (by weight) were dry pressed and nitrided at four different temperatures and then analysed by XRD to determine the residual silicon content, and whether a reduction in the temperature necessary for nitriding had been achieved. The residual silicon and the β-Si_3N_4 content were plotted as a function of nitriding temperature and percentage of oxides added. The results are shown in figs.4.6-4.9. The phase concentrations were calculated using the method described in [65] (see 3.3). The accuracy of the phase concentration measurements is estimated to be ±2%. The samples were also examined in the SEM (see chapter 5).

Both NiO and MnO_2 reduce the residual silicon content at lower nitriding temperatures.

A sample nitrided at 1207°C contained 0.4% Si (for 1% MnO_2 added), compared to 17.4% Si for a sample nitrided at the same temperature with no additives. The NiO was found to strongly influence the formation of β-Si_3N_4, with β content increasing as a function of nitriding temperature and NiO concentration, the maximum being 33.5% β at 10% NiO, compared to 5% β in the sample with no additive, both nitrided at 1350°C. No significant effect was found with the MnO_2 additive on the formation of β-Si_3N_4.

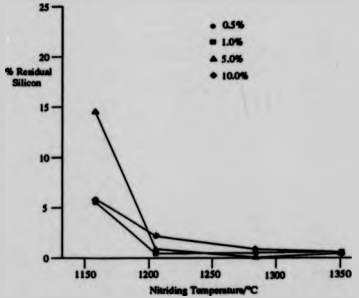

fig.4.6 Effect of MnO_2 on residual silicon content for different nitriding temperatures

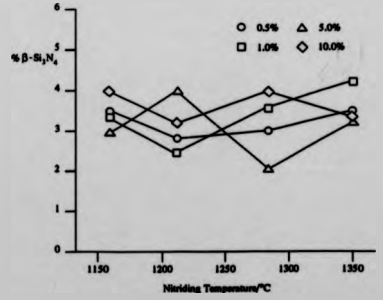

fig.4.7 Effect of MnO_2 on β-Si_3N_4 content for different nitriding temperatures

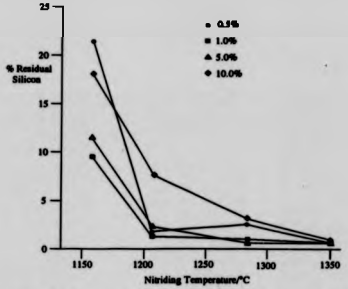

fig.4.8 Effect of NiO on residual silicon content at different nitriding temperatures

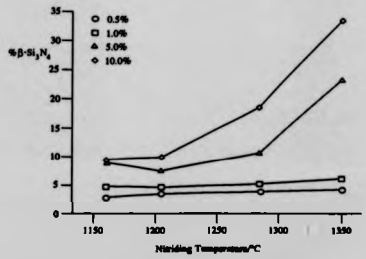

fig.4.9 Effect of NiO on β-Si_3N_4 content for different nitriding temperatures

It is likely that the metal oxide additives encourage the nitriding process by the formation of a liquid silicide or silicate phase that encourages the silicon-nitrogen reaction. Iron impurities have also been shown to enhance nitriding [71,72] but FeO was found to be inferior to MnO_2 and NiO in TGA and DTA nitriding studies [70]. The inherently low oxidation resistance and low matrix cracking stress of RBSN made the further development of this system unattractive, compared to the dense SRBSN materials studied.

4.2.3 SiC/SRBSN

The low strength and poor oxidation resistance of RBSN prompted the development of a dense matrix material, and sintered reaction bonded silicon nitride was chosen because of the relatively low shrinkage during densification.

Composite samples using MgO, MgO/SiO_2 and Y_2O_3/Al_2O_3 additive systems were produced to investigate variations in composition and hot pressing conditions (table 4.1). The matrix was tape cast onto fibres to make prepreg (section 4.1.2), however PVA was used as a binder in samples up to 22B, as the final binder system had not been chosen. This gave poor monolithic tape, and as a result, the early composite samples were not clad either side with monolithic matrix. Eight ply unidirectional laminates 50mm square were hot pressed at 1200°C for 1 hour at up to 10MPa, nitrided using the standard cycle, hot pressed at the sintering temperature, the density and volume fraction then being measured for each plate (table 4.1). X-ray diffraction analysis showed that the matrix in samples pressed at 1560°C consisted of predominantly α-Si_3N_4, whereas at 1700°C or higher, the matrix had transformed to β-Si_3N_4 (see figs 4.10 and 4.11). The samples were examined microstructurally (chapt 5) and mechanically tested (chapt 6).

Yttria/alumina additive SRBSN matrix composites were initially investigated using the samples 15 and 17 (the composition was not exactly 6wt% yttria/4wt% alumina in the nitrided material as no allowance was made for the increase in mass due to the formation of silicon nitride during nitriding of the silicon powder). Sample 15 was accidently pressed at approximately 1550°C due to a fault on the hot press, and did not transform from α to β-Si_3N_4 or density well, but was found to have superior mechanical properties compared to sample 17 which was hot pressed at 1750°C. This was thought to be due to fibre degradation at 1750°C, as the fibre/matrix interfacial properties (chapt.5) were similar to sample 15. An SRBSN composition suitable for pressing at temperatures lower than 1750°C was sought, and MgO additive SRBSN was investigated (samples 21A to 22B).

Sample	%Si	%Si_3N_4	%SiO	%MgO	%Y_2O_3	%Al_2O_3	Pressing Temp/°C	Pressure /MPa	Major Si_3N_4 phase	Density /gcm^{-3}	Fibre V_f/%
15	54	36	–	–	6	4	1550	5.5	α	–	–
17	54	36	–		6	4	1750	5.5	β	–	–
21A	43.55	43.55	–	10	–	–	1560	10	α	3.038	41.8
21B	43.55	43.55	–	10	–	–	1700	10	β	3 083	51.1
22A	46.72	46.72	–	5	–	–	1560	10	α	3.113	42.7
22B	46.72	46.72	–	5	–	–	1700	10	β	3.077	55.0
23	41.02	46.15	–	–	7.70	5.13	1700	20.5	α	3.02	16.8
24	34.17	58.97	3.31	3.55	–	–	1700	20.5	β	2.94	27.2
27	53.72	35.64	–	–	8.03	2.61	1700	20.5	β	3.159	25.1

Table 4.1 SRBSN compositions and processing

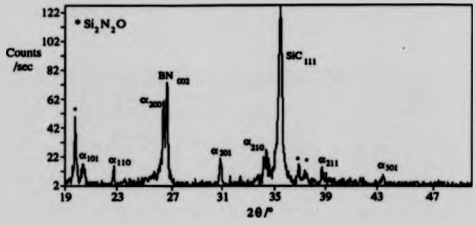

fig.4.10 XRD trace from sample 21A pressed at 1560°C

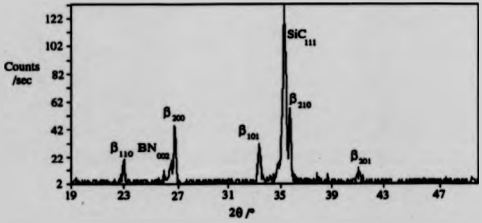

fig.4.11 XRD trace from sample 21B pressed at 1750°C

After improvements were made to the hot press, the maximum pressure used for hot pressing was increased to 20.5MPa and the yttria/alumina additive system was re-examined. A new batch of Y_2O_3/Al_2O_3 material, sample 23, was made up in parallel with an MgO/SiO_2 batch, sample 24 (table 4.1). A mechanical, micromechanical and microstructural comparison of the two materials was then carried out. The volume fractions of the batches of material vary because of difficulties in making reproduceable prepreg in the two compositions.

A large batch of material (27) was then produced, using a 6wt% Y_2O_3/2wt% Al_2O_3 additive system (in the nitrided condition), each 50mm square plate being given a letter (A,B,C,....). This composition had been prepared by L.Falk [7] in the pressureless sintered monolithic form. All the prepreg was produced in the same way on the machine using the slip composition shown in table 4.2 (total weight of dry powder = 200g), and an effort was made to make the processing as similar as possible for all the plates. The material was investigated in detail microstructurally and mechanically (at room temperature and at elevated temperature).

Component material	mass/grams
KD1 dispersant (ICI)	4
Trichloroethane	30
Ethanol	23
Santicizer 160	3.6
Du Pont 5200 binder	50
Methyl ethyl ketone	37
Y_2O_3 powder	16
Al_2O_3 powder	5.2
Si_3N_4 powder (UBE)	71
Si powder (KemaNord 4E)	107

5.0 MICROSTRUCTURE AND MICROMECHANICAL PROPERTIES

Composite microstructure was studied using SEM on polished sections and TEM on ion beam thinned specimens. X-ray mapping was carried out in the SEM on interfacial regions, and EDX analysis was used in the TEM to determine the grain boundary phase composition. Micromechanical measurements to determine interface properties were carried out using indentation to debond and push out fibres in thin sections of composite; the test method and results are discussed. The microscopy of fracture surfaces of test specimens is discussed in chapter 6 with the macro-mechanical property data.

5.1 MICROSTRUCTURE OF RBSN MATRIX COMPOSITES

Early SiC/RBSN composite samples had poor fibre distribution, low fibre volume fraction, and variations in matrix porosity. Fig. 5.1a shows a typical low magnification example of a section of composite, which is part of a bend test bar.

The layers of fibres (from the individual preprega) can be seen horizontally, the gap between fibres being variable, and sometimes large, giving rise to uneven fibre distribution, and a low volume fraction. This was due to inexperience in prepreg preparation, and variability induced by the filament winding machine. Figure 5.1b shows an optical view of fig.5.1a, the fibres and matrix having a greater contrast difference when examined using this method. The layered structure of the fibre, and the interface with the matrix can be seen in fig 5.2, the pyrolytic carbon layer deposited onto the core, the SiC sheath, and the twin carbon rich layers. Faint growth rings can be seen towards the centre of the fibre, which presumably arise from the slight variations in the deposition process. The large (typically 10μm) pores within the matrix are clearly visible.

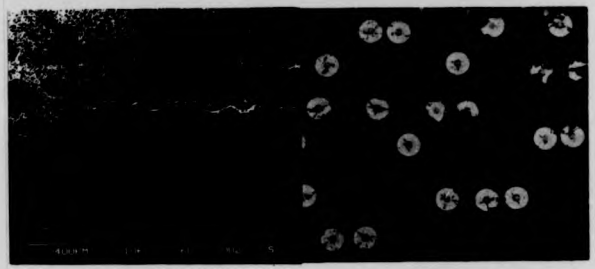

fig.5.1a Low magnification view of early SiC/RBSN composite

fig.5.1b Optical low magnification view of early SiC/RBSN composite

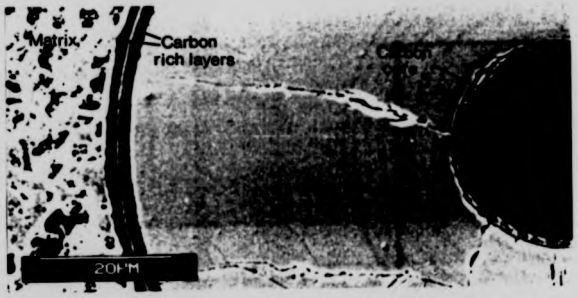

fig.5.2 SCS-6 fibre, showing layered structure, and porosity of adjacent matrix (secondary electron imaging)

The conversion of silicon to silicon nitride in the early composites was incomplete, residual silicon particles are most easily seen in optical micrographs, because they give a high contrast compared to the darker surrounding RBSN. A high magnification view of the fibre/matrix interface (fig.5.3) shows evidence of a thin reaction layer between the

outer carbon rich layer and the matrix. In this backscattered electron image, atomic number contrast shows low z regions (e.g. carbon rich layers) in dark contrast, and higher z regions (e.g. silicon containing) in light contrast.

fig.5.3 High magnification view of interface, showing reaction of outer carbon rich layer with the matrix (backscattered electron imaging).

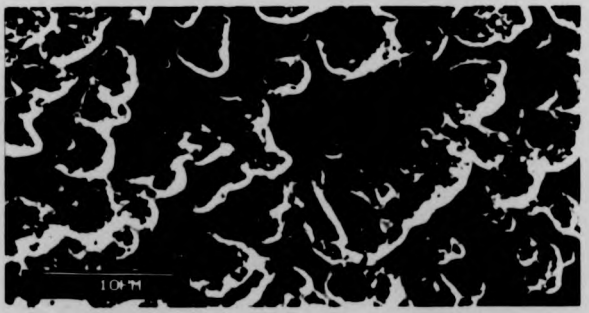

fig.5.4 RBSN matrix microstructure, showing characteristic porosity (secondary electron imaging)

Fig.5.4 is a high magnification view of the matrix, showing the high degree of porosity characteristic of RBSN. The specimen was difficult to prepare for microscopy due to the relatively weak matrix, with very hard fibres embedded within it.

A small amount of microscopy was carried out on NiO additive RBSN samples. Fig 5.5 shows nickel-containing particles within the surrounding RBSN matrix imaged using backscattered electrons. The sample contains 1.0wt% NiO additive and was nitrided at 1207°C. The backscattered imaging mode shows nickel-containing areas in light contrast (higher z than the surrounding silicon nitride), porosity (characteristic of RBSN) is observed in dark contrast. Energy dispersive X-ray (EDX) analysis was used to confirm the presence of nickel within the light areas, and was also used to map the distribution of nickel and silicon (fig.5.6). The technique was later used for elemental mapping of fibre/ matrix interfaces within SRBSN matrix composites, including the mapping of light elements such as carbon, nitrogen and oxygen (see the following section). The porosity (and implied lack of oxidation protection given to embedded fibres) of RBSN discouraged further work on the NiO and MnO_2 additive materials.

fig.5.5 Backscattered image of 1.0wt% NiO additive RBSN, nitrided at 1207°C

fig.5.6 X-ray mapping of Ni and Si in 1.0wt% NiO additive sample

5.2 MICROSTRUCTURE OF SRBSN MATRIX COMPOSITES

5.2.1 As fabricated material - matrix microstructure

The low magnification microstructure of SRBSN matrix composites was similar to the RBSN matrix composites, although greater control of fibre spacing and prepreg thickness gave a more even fibre distribution (fig.5.7). The SRBSN matrix has a higher density than the RBSN, porosity being isolated rather than continuous. A directional effect was observed in some samples, where porosity is present between fibres in the same layer, and dense matrix is present between fibres in successive layers (fig.5.8).

The 6%Y_2O_3/2%Al_2O_3 SRBSN material was also examined in the TEM; EDX elemental analysis and electron diffraction were used to confirm phase identification. The specimen preparation technique for the composite material was found to be very difficult, the carbon containing fibre/matrix interface region being very susceptible to mechanical damage and a faster thinning rate in the ion beam than the silicon carbide sheath or the bulk matrix.

fig.5.7 Low magnification view of SRBSN matrix composite

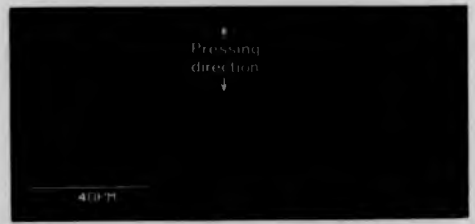

fig.5.8 Porosity variations within SRBSN matrix, pressing direction indicated

Fig.5.9 shows the matrix microstructure, consisting of β-silicon nitride grains and a glassy grain boundary phase. A diffraction pattern for the <001> zone axis was obtained from the silicon nitride crystal in dark contrast, and gave d spacings in good agreement (<1% error) with X-ray diffraction data.

fig.5.9 6%Y_2O_3/2%Al_2O_3 matrix microstructure showing β-Si_3N_4 grains

The glassy grain boundary phase was analysed using EDX, and a higher magnification view of β-Si_3N_4 grains with pockets of grain boundary glass is shown in fig.5.10. The β-Si_3N_4 was also analysed for comparison. The grain boundary glass was found to contain O, Al, Si, Y and a small amount of N, which is typical of monolithic examples of this matrix composition. Semiquantitive analysis of the heavier element content gave an average composition of 22 Si, 19 Y, 6 Al. These values were calculated by comparing the areas under the fitted peaks for each element, applying corrections for fluoresence yield (ω), ionisation cross-section (Q), and assuming a value of 1 for detector efficiency; no beryllium window was used. This composition is close to the SiO_2, Al_2O_3, Y_2O_3 eutectic, which has a liquidus around 1400°C. The high temperature properties (strength, creep rate etc.) are largely determined by the softening temperature of the grain boundary phase, so the control of its composition is an important part of material preparation. The presence of impurities such as Fe, Ca and Na lower the liquidus temperature further, hence contamination must be avoided both during powder milling, and from binder residue etc.

Crystallisation of the grain boundary phase would leave a residual glass as the composition is not a stoichiometric mixture.

fig.5.10 Grain boundary glass EDAX analysis, with β-Si_3N_4 analysis for comparison

Analysis of the β-Si_3N_4 grains indicated that a limited substitution of Al^{3+} and O^{2-} had occurred, forming a β'-Si_3N_4 phase. The degree of substitution was estimated to be 10%, giving an effective β' formula of

$$Si_{6-z}Al_zO_zN_{8-z} \qquad (z=^3/_5)$$

The difference in lattice parameter obtained by this degree of substitution could be expected to be <0.1% which is difficult to detect using a simple diffractometer. A diffraction run was carried out using a powdered sample (taken from the same sample used to prepare the TEM specimen) and silicon powder as an internal standard, to allow higher accuracy measurements of 2θ to be made than usually possible with a diffractometer. No difference could be found between the published (JCPDS) value for the lattice parameters and the measured values using this technique, implying that the

degree of substitution was low. One explanation for the aluminium detected in the β-Si_3N_4 grains is fluorescence from the grain boundary phase. Counter to this argument is that very little Y was detected when analysing the β-Si_3N_4 grains, whereas the Y content of the grain boundary phase was high, typically three times the Al content.

5.2.2 As fabricated material - fibre microstructure

The greater density and strength of the composite allowed a better quality of finish to be achieved during SEM specimen preparation, and a 'tree ring' effect was observed towards the carbon core of fibres in some specimens; this is shown in fig.5.11, which is a high magnification view of the carbon core/ silicon carbide sheath region of a fibre. The pyrolytic carbon layer, which is applied to the carbon core prior to deposition of the CVD SiC layers can also be seen in fig.5.11, and has a thickness of approximately 1.5μm.

Radial pores were observed in the outer SiC layer of the fibre, the pore size being <5μm. The pores appeared to be confined to the outer region of the fibre, clearly seen in backscattered electron imaging (fig.5.12). Fig.5.13 is a TEM view of the SiC sheath around the carbon core of the fibre, showing the columnar grain structure. The faulted appearance of the grains is typical of silicon carbide, particularly grown by CVD, and is due to stacking faults and twins in the 3C silicon carbide polytype, and the presence of other polytypes of SiC. The creep behaviour of SCS-6 has been attributed to either free silicon [59] or free carbon [73] in low concentrations, but no evidence of either was observed in this work.

fig.5.11 'Tree ring' effect in SiC sheath close to inner carbon core in SCS-6 fibre

fig.5.12 Porosity in outer SiC layer of fibre (backscattered electron image).

fig.5.13 SiC sheath, showing radial columnar grain structure

5.2.3 As fabricated material - interface microstructure

The fibre/matrix interface was studied using backscattered electron imaging and X-ray mapping in the SEM, and bright field imaging, electron diffraction and EDS in the TEM. Backscattered imaging of the interface region showed that specimens containing Al_2O_3/ Y_2O_3 pressed at 1700°C had a thin reaction layer between the fibre and matrix (fig.5.14), whereas the MgO containing sample pressed at the same temperature had a thicker reaction layer (fig.5.15). The interface region was mapped using X-rays, for carbon, nitrogen, oxygen, silicon and sintering additives, showing the reaction zone between the matrix and the outer layer for samples where the zone was thick enough. Fig. 5.16 shows the X-ray maps obtained for 5wt% MgO additive SRBSN pressed at 1700°C. The magnesium map shows a trace of magnesium in the fibre sheath; this is due to the background radiation and the strong silicon K_α peak (1.739 keV) producing spurious

counts at the magnesium K_α peak energy (1.253 keV). The original carbon outer layer position is shown on the silicon map and can be compared with the backscattered image of the same sample (fig.5.15) and that of the Y_2O_3/Al_2O_3 additive sample (fig.5.14).

fig.5.14 Fibre/Matrix interface in Al_2O_3/Y_2O_3 additive SRBSN matrix composite

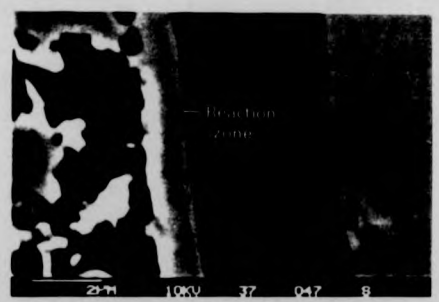

fig.5.15 Fibre/Matrix interface in 5wt% MgO additive SRBSN matrix composite pressed at 1700°C showing reaction zone between matrix and outer carbon rich layer of fibre

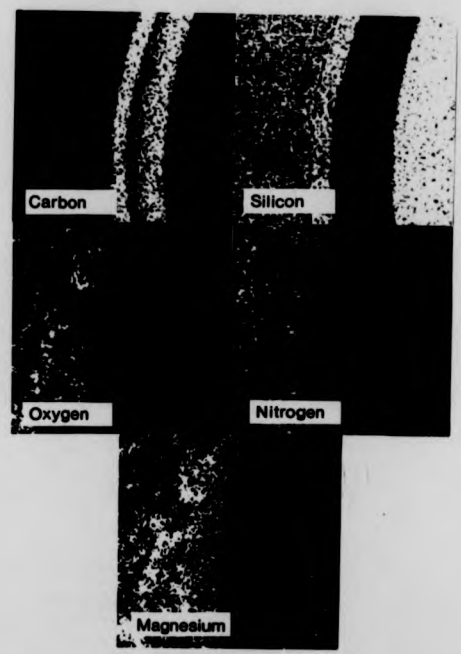

fig.5.16 X-ray maps of carbon, nitrogen, oxygen, magnesium and silicon at the fibre matrix interface in 5wt% MgO additive SRBSN pressed at 1700°C.

Fig.5.17 shows similar map for a Y_2O_3/Al_2O_3 sample pressed at 1700°C in which there was less detectable reaction between the fibre and matrix. A feature of both the X-ray maps and the backscattered electron images is the silicon rich zone between the outer layers of the fibre and in the reaction zone. There is a corresponding reduction in the carbon concentration, indicated by a dark region between the carbon rich layers and (particularly in the MgO additive sample) in the reaction zone.

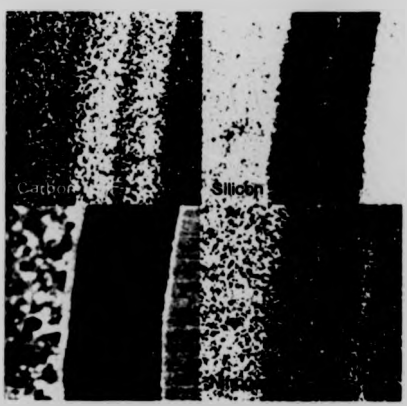

fig.5.17 Backscattered image and corresponding X-ray maps for carbon, silicon and nitrogen for a Y_2O_3/Al_2O_3 SRBSN sample pressed at 1700°C.

A view of the outer fibre layers is shown in fig.5.18. The inner layer has separated from the silicon carbide sheath, which was often seen when specimen were mechanically tested (see chapter 6). The twin carbon layers can be seen, the outer layer reaction zone being clearly defined. The silicon rich layer between the carbon layers can be seen as a well defined boundary, and can be compared to the backscattered SEM images, where there is a sharp division between the inner and outer layers.

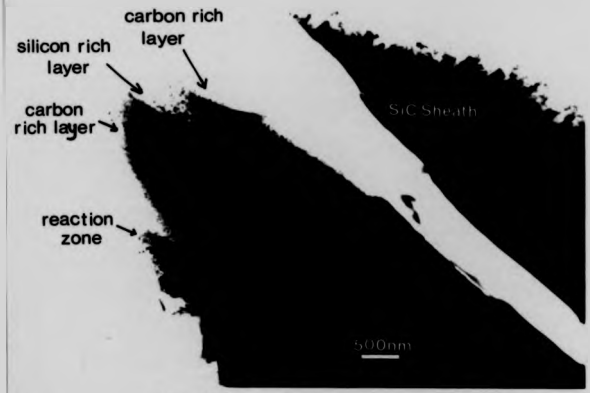

fig.5.18 Fibre outer layers separated from SiC sheath

Fig.5.19 shows the outer layers at higher magnification, with silicon nitride grains attached to the outer layer. The carbon layers and the reaction zone have small particles within them, the density of particles being higher in the reaction zone. The particles were found to be crystalline as they showed diffraction contrast when the specimen was tilted. Diffraction patterns from the carbon rich layers show the existence of silicon carbide in the form of fine crystallites (diffraction rings formed), with an enrichment of silicon carbide in the reaction zone (stronger diffraction rings than the unreacted part of the layers). The diffraction patterns also reveal the presence of graphitic carbon, with a preferred orientation, the patterns in the outer layer being more pronounced. The silicon carbide particles distributed within the unreacted part of the layers were produced during the final chemical vapour deposition of carbon on the surface of the fibres. Diffusion of silicon from the matrix has enriched the silicon carbide concentration in the reaction zone.

fig.5.19 Outer fibre layers, showing reaction layer, outer carbon layer, silicon rich zone, inner carbon layer and diffraction patterns.

5.3 EFFECT OF OXIDATION ON MICROSTRUCTURE

Samples of the 6%Y_2O_3/2%Al_2O_3 additive composite were subjected to oxidation at 1000°C, 1200°C and 1400°C for 100 and 1000 hours, sectioned, polished and examined in the SEM (the mechanical behaviour and fracture surfaces of the samples are described in chapter 6). 100 hours oxidation at 1000°C, 1200°C and 1400°C appeared to have little visible effect on the carbon rich layers; examples of these are shown in fig.5.20, 5.21 and 5.22.

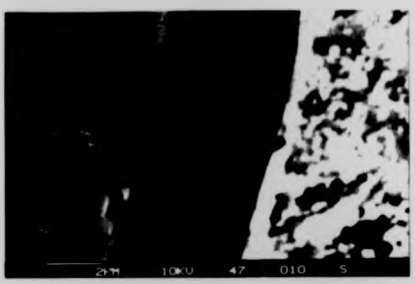

fig.5.20 SiC/SRBSN sample oxidised for 100 hours at 1000°C.

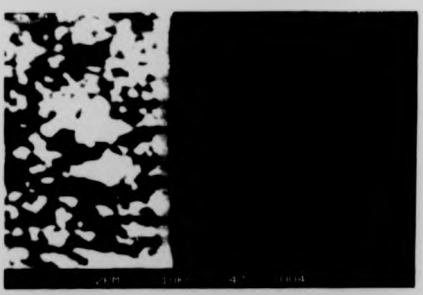

fig.5.21 SiC/SRBSN sample oxidised for 100 hours at 1200°C

fig.5.22 SiC/SRBSN sample oxidised for 100 hours at 1400°C

For oxidation times of 1000 hours, damage to the composite was more obvious; fig.5.23 shows the interfacial region in a sample oxidised for 1000 hours at 1000°C. The carbon rich layers have been removed, however both the silicon rich zone between the layers and the reaction zone between the outer layer and the matrix remain. The central carbon core is also removed during prolonged oxidation, as shown in fig.5.24, which is part of the same sample.

fig.5.23 Interfacial region of SiC/SRBSN sample oxidised for 1000 hours at 1000°C

fig.5.24 Central carbon core of SiC/SRBSN sample oxidised for 1000 hours at 1000°C

After 1000 hours at 1200°C, there was less evidence of damage than 1000°C, the carbon rich layers being largely intact (fig.5.25). After 1000 hours at 1400°C, the composite was found to be quite severely damaged by oxidation, with an yttrium rich glassy layer forming at the interface for fibres close to the sawn edge of samples (fig.5.26).

fig.5.25 SiC/SRBSN sample oxidised for 1000 hours at 1200°C

fig.5.26 SiC/SRBSN sample oxidised for 1000 hours at 1400°C

A glassy oxide layer had formed on these samples, which was rich in yttrium, having light contrast in backscattered electron imaging. This layer was removed by grinding with silicon carbide paper prior to bend testing the samples, however there were some areas of glass observed which had crystals that had grown within them (fig.5.27). Yttrium disilicate ($Y_2Si_2O_7$) crystals have previously been observed in similar materials after prolonged periods of oxidation at high temperatures [74].

fig.5.27 Growth of crystals within glassy oxide layer on a SiC/SRBSN sample after 1000 hours at 1400°C.

5.4 MICROMECHANICAL BEHAVIOUR

Push-through tests were first carried out on the early MgO and Y_2O_3/Al_2O_3 SRBSN matrix composites, to obtain a value for the fibre/matrix interfacial shear stress τ. The fibre ends were loaded using different weights on a Vickers indenter (several fibres were indented for each load), and the samples were then examined in the SEM to determine whether the fibres at each stress had debonded and moved. A histogram of percentage of debonded fibres against interfacial stress was then plotted. It was found that the fibres in the MgO additive material were strongly bonded to the matrix, with a lower limit of interfacial shear strength of 8MPa (the maximum stress able to be applied). The ends of the fibres indented were damaged by the indenter due to the high loads applied. The Y_2O_3/Al_2O_3 additive material gave better results, and was measured in the as produced state, and after 1 hour and 5 hours oxidation at 1000°C, the histograms are shown in fig.5.28 (each sample section tested was 6mm from the exposed end of the fibres).

As can be seen, the effect of oxidation at 1000°C is to progressively reduce the interfacial shear strength between the fibre and matrix. The as produced material had a strength ranging from 4MPa down to approximately 2MPa (no fibres moved at stresses<2MPa. After one hour of oxidation, the interfacial shear strength had reduced to between approximately 2 and 1 MPa, and after five hours exposure, most fibres were being permanently debonded at stresses of 1MPa. It should be noticed that the interfacial shear strength measured in this way is a range of values, rather than a single value. This variation may be a material property, however part of the variation observed may be attributed to the test method, which was labour intensive and repetitive (which allowed scope for human error). The indentation system did not have a very accurate indentor positioning arrangement (although the fibres used were of relatively large diameter

compared to Nicalon and Tyranno fibres) and the indentations made were generally within approximately 0.25 fibre diameters of the centre of the fibre.

A system developed in a separate program [75] enabled the controlled indentation of a fibre using a diamond indentor attached to a piezoelectric actuator, with a load cell sandwiched in-between to measure the force applied. The whole system was mounted on the X-Y stage in a JEOL JSM6100 scanning electron microscope allowing accurate indentor positioning (within 1-2μm) and observation of the indentation process. The load cell output was fed into a specially developed high input impedance amplifier, and recorded simultaneously on a storage oscilloscope, and an Acorn Archimedes 310 computer fitted with an analogue input port. The Archimedes also provided output signals to control the piezoelectric actuator (via its high voltage power supply), and the software developed enabled a load/deflection curve to be generated for each indentation test.

A standard flexure sample (nominal dimensions 50x6x2 mm) was oxidised for 100 hours at 1200°C, and sliced into 5mm sections, starting from one end (the first 1mm was removed to allow a clean surface for polishing). Six of the sections were mounted in slots milled in a 30mm diameter brass disc of 5mm thickness using epoxy, and both sides of the disc (and therefore both ends of each section) were polished on an automatic polisher.

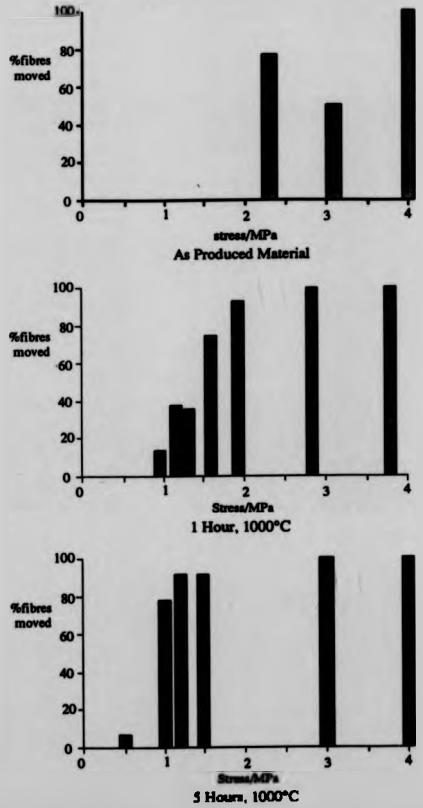

fig.5.28 Early interfacial shear results for Y_2O_3/Al_2O_3 SRBSN matrix composites, in the as fabricated state, and after oxidation.

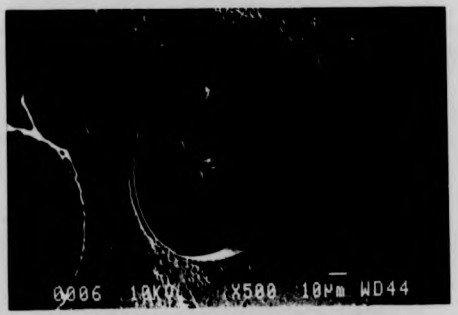

fig.5.29 Indented fibre (push through test)

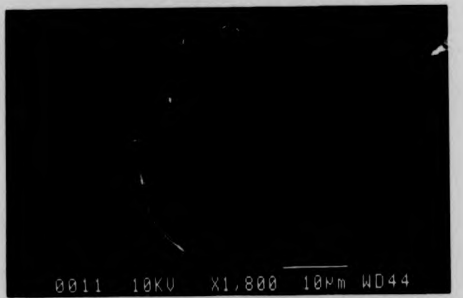

fig.5.30 Central carbon core of an indented fibre, showing debonding at carbon core/pyrolytic graphite interface, and displacement of carbon core.

The samples were indented and a typical post indent fibre is shown in fig.5.29. The indentor touched the fibre close to the centre of the carbon core, which was itself displaced during the overall indentation (fig.5.30). As can be seen in fig.5.29, the carbon rich layers remained attached to the surrounding matrix, confirming the results observed

in TEM studies of the interface, where the separation of the fibre from the matrix occurred at this interface. It appears from fig.5.30 that the inner carbon core has debonded at the interface with the pyrolytic carbon, and the carbon fibre has remained displaced by approx.0.5μm. The load/deflection curve from an indentation of a fibre in the slice closest to the end of the sample is shown in fig.5.31. A debonding event can be clearly seen, followed by a steady fibre pushthrough until the Vickers indenter makes contact with the surrounding matrix, after which the load increases.

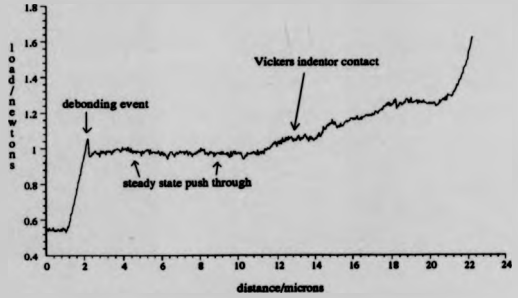

fig.5.31 Load/deflection trace from fibre pushthrough test

The total distance moved by the fibre in the above example can be seen to be approx.19μm. The initial load on the indenter was zero, prior to contact with the fibre, however the load reading on the computer at this stage was not zero because of an offset in the load cell amplifier. This offset was removed by subtracting the zero reading from each load value to obtain the true load and the effective interfacial shear stress was then calculated for the load just before the debonding event, and also for the pushthrough load. The push through load was only constant in a few cases, generally tending to rise steadily

after debonding, but the indenter contact with the matrix was always accompanied by an increase in the slope of the load/deflection curve.

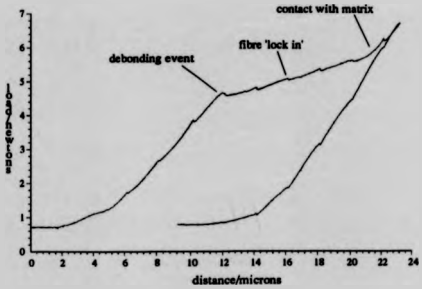

fig.5.32 Load/deflection curve for fibre in fig.5.29

An example of this behaviour is shown in fig.5.32 (a load/deflection curve for the fibre in fig.5.29), having a rise in load after the debond, but before contact of the indenter wth the surrounding matrix. This effect has been attributed to a fibre 'lock-in' process, due to aspherities on the fibre surface preventing the fibre from sliding smoothly through the matrix [76] (although in that case the effect was observed during the pushback of the fibre after an initial indentation). An increase in friction from debris between the fibre and the matrix (produced as a result of sliding at the interface) is another possible cause of the rise in load, particularly if the fibre has previously been moved during specimen polishing etc.. The indenter contact was central with the fibre axis in fig.5.29/5.32, and the rise cannot therefore be attributed to partial contact with the matrix. The combined debond and pushthrough results from slices at 3.75,14.25 and 24.75 mm distance from the end of the sample are shown in fig.5.33, (these values being the distance from the end of the

sample to the centre of the slice). There is scatter in the results, which reflects the previous results from the simple indentation rig using dead weight loading. The main feature in fig.5.33 is a dip in the pushthrough stresses at 14.25mm accompanied by a small drop in debond stress.

The large diameter of the fibres allows the use of a flat ended punch rather than a Vickers diamond indenter. This technique has been employed [76] to investigate the effect of moving fibres under frictional conditions for larger distances than have been investigated here. The positioning of the punch indenter is easier to achieve because the end can be seen in a microscope; the large included angle of a Vickers indenter prevents direct viewing of the tip, making positioning less accurate.

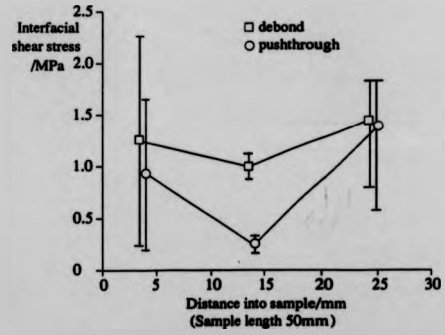

fig.5.33 Debond and pushthrough interfacial shear stresses for sample oxidised at 1200°C for 100 hours (results have been displaced from the correct positions for clarity).

In summary, the indentation testing of the composites has shown that the fibre/matrix interfacial shear strength is low (<2.5MPa), and the interfacial shear sliding stress is also

low (<2MPa), with little variation after oxidation after 100 hours at 1200°C in air. The fibres in samples that had been more severely oxidised appeared to be even less well bonded, as they tended to be debonded during specimen polishing process for SEM examination.

5.5 DISCUSSION OF COMPOSITE MICROSTRUCTURE

The microstructure of the early RBSN matrix composites and the later SRBSN matrix composites have been investigated using SEM, TEM and optical microscopy. At low magnifications, the composites are similar, consisting of an array of fibres within a silicon nitride matrix, RBSN matrices being porous, and SRBSN matrices being dense. The poor control of fibre spacing in the early materials reflects the lack of development of the filament winding system, later SRBSN samples having more even fibre spacing.

The RBSN matrix was similar in α/β Si_3N_4 phase ratio [52,77] and appearance [2] to previously reported material, with needle like grains, pores between 5 and 10μm in size and occasional areas of free silicon (unconverted during nitriding). The addition of small amounts (1wt%) of MnO_2 or NiO was found to improve the nitridation process, lowering the nitriding temperature to approx. 1200°C. This raises the possibility of using RBSN as a matrix for Nicalon and Tyranno fibre reinforced composites, although fibre damage by silicon particles during the 1200°C hot pressing process may limit this approach. Higher magnification SEM investigation of the fibre/matrix interface showed some evidence of a reaction layer between the matrix and the outer carbon layer on the fibre. Debonding between the inner carbon layer and the SiC sheath was observed at the fracture surface (fig.6.2a). Poor oxidation resistance of the RBSN matrix discouraged further work on these composites.

SRBSN matrix composites were densified by hot pressing (using sintering aids) after the nitriding process had been carried out. The lower porosity level was immediately obvious, however some porosity still occurred, particularly between adjacent fibres in a layer, where the hydrostatic pressure is lower than that between fibres in different layers (see fig.5.34).

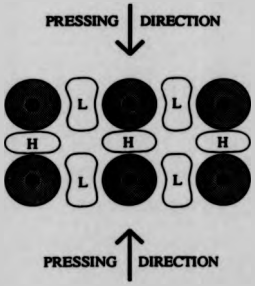

fig.5.34 Approximate distribution of hydrostatic pressure in the matrix during hot pressing

The variation in pressure arises because the sample is not being compressed isostatically, and also because the matrix is not behaving in a true hydrostatic manner. The porosity in the SRBSN composites was closed (compared to the interconnected porosity of the RBSN matrices), and densities were generally >95% theoretical, giving much improved oxidation resistance.

Initial trials using MgO as a sintering aid showed significant reaction between the matrix and the outer carbon layer of the fibre, X-ray EDX analysis showing that silicon was the major element present in the reaction layer, other than carbon. In some cases, the

whole outer layer had reacted, the silicon rich zone appearing to act as a barrier to further reaction with the inner layer. A thinner layer was present in the Y_2O_3/Al_2O_3 additive samples, and silicon was again the major matrix element present. X-ray mapping of the interfacial layer showed the spatial distribution of elements at the interface, the use of an ultrathin window in front of the detector allowing the mapping of light elements such as C,N and O. Resolution using this technique is limited due to the finite X-ray excitation volume in the sample when mapping small scale (<1μm) structures, and the difficulty of acquiring the X-ray map in a reasonable time..

Transmission microscopy revealed a typical sintered silicon nitride microstructure with elongated β-Si_3N_4 grains and a glassy grain boundary phase. The grain boundary phase contained Y, Si, Al, and O, and was amorphous in as produced material. The composition was close to the SiO_2-Y_2O_3-Al_2O_3 eutectic, which has a liquidus around 1400°C. The viscosity of the grain boundary phase is determined critically by the composition and is lowered by additions of Ca and Fe, which are common contaminants in silicon and silicon nitride powders. The high temperature properties (strength, creep rate and stress rupture life) are determined to a large extent by the volume fraction and viscosity of the grain boundary phase, the refinement of which has been the subject of much study in recent years. A reduction in volume fraction would lead to improvements in high temperature behaviour, at the expense of ease of final densification; most high performance monolithic silicon nitrides are densified by the HIPping process at pressures>100MPa. By control of the composition, a grain boundary phase can be produced which is able to be crystallised to a more refractory phase by further heat treatment of the material enhancing the high temperature properties of the material. Knowledge of the silica (SiO_2) content of the starting silicon nitride and silicon powders, and careful control of impurity levels are

neccessary.

Aluminium and oxygen were found in the β-Si_3N_4 grains using EDX analysis, implying that the grains were a β'-Si_3N_4 solid solution, with a substitution level of $z=^3/_5$. X-ray diffraction analysis using a silicon internal standard gave lattice parameters indistinguishable from the published JCPDS data for β-Si_3N_4 , which implied that the degree of Al and O substitution was very low. The EDX results show a definite Al peak, with no discernable Y (a Y peak would be expected if there was fluorescence from the grain boundary phase when a β-Si_3N_4 grain was analysed). It is concluded that there is some Al and O substitution in the β-Si_3N_4 grains, although at a level too small to detect by measuring the lattice parameters using XRD.

The fibre/matrix interface was investigated to determine the nature of the reaction between the matrix and the outer carbon layer. Selected area electron diffraction showed the presence of fine grained silicon carbide dispersed throughout the carbon layers and the silicon rich zone, identified by SiC 111 and 220 diffraction rings. The rings were much stronger in the reaction layer so the major constituent was concluded to be silicon carbide. The role of the sintering aids in the reaction layer is unclear at present, and concentrations in the reaction layer (from peak heights in the SEM EDX spectra) were low.

The reaction layer present may prove to be beneficial in future composites of this type in terms of forming an oxidation barrier, protecting the carbon rich layers from oxygen diffusing through from the matrix, as it remains after severe oxidation damage had occurred (fig.5.23). In the current (6%Y_2O_3/2%Al_2O_3) material the predominant damage mechanism is 'piped' oxidation running down the fibre/matrix interface from exposed fibre ends.

The theoretical behaviour of the interface in SiC/Si_3N_4 systems has been

thermodynamically modelled [78] and the principle reactions likely to occur between SCS-6 fibres and a surrounding silicon nitride matrix identified. Reactions can occur between surface silica in the silicon nitride matrix and the carbon in the outer layers and also between carbon and silicon monoxide (present in gaseous form at a high temperature) e.g.

$$SiO_2 + 3C = SiC + 2CO \qquad (5.1)$$

$$2SiO_2 + 3C = SiC + SiO + 3CO \qquad (5.2)$$

$$2SiO + 2C = 2SiC + O_2 \qquad (5.3)$$

For 1 atmosphere total pressure, the interface is unstable above 1783K (1510°C). The nitrogen pressure also controls the reaction between silicon nitride and carbon e.g.

$$Si_3N_4 + 3C = 3SiC + 2N_2 \qquad (5.4)$$

This reaction can occur at temperatures above 1712 K (1440°C) under a 1 atmosphere N_2 pressure. Thus although carbon provides a good interface layer between the fibre and matrix in a SiC/Si_3N_4 composite, a reaction with the matrix is thermodynamically favourable during processing (typically 1700°C) and during service if temperatures are in excess of 1440°C. The formation of a thicker layer in MgO additive composites may be explained by the reaction between elemental silicon (in the un-nitrided material) and MgO e.g.

$$Si + 2MgO = SiO_2 + 2Mg\ (g) \qquad (5.4)$$

$$Si + 3MgO = MgSiO_3 + 2Mg\ (g) \qquad (5.5)$$

The SiO_2 produced in the reaction (5.4) can have two effects, firstly to inhibit the

nitridation process by sealing off areas of unreacted silicon from the nitriding gas, and secondly to react with carbon in the interfacial layers to form silicon carbide. There is therefore another source of SiO_2 to react with carbon, other than that already present on the silicon nitride particle surfaces.

The silicon nitride/carbon stability diagram given in [78] was reproduced using the National Physical Laboratory MTDATA thermodynamic material database, assuming an excess of carbon (as would be present in an unreacted SCS-6/Si_3N_4 interface) for a number of different pressures and temperatures. The result is shown in fig. 5.35.

The SiC microstructure in the SCS-6 fibre was identical to that reported by other workers [60] consisting of heavily faulted grains, elongated in the direction of growth (radial). No difference in the microstructure was observed in the TEM as a result of the composite processing, however porosity in polished sections was observed in the SEM, particularly in the outer region of the fibre. The pores were elongated in the radial direction with a length <5μm.

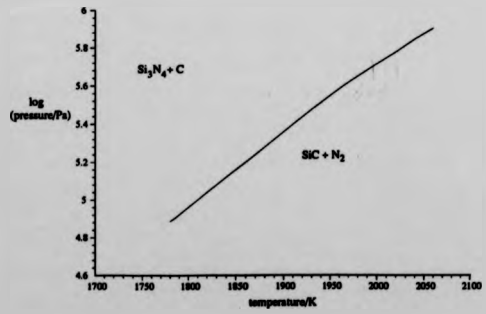

fig.5.35 Stability diagram for Si_3N_4/SiC system

Micromechanical testing by indentation of fibres in a thin section of the composite showed that the interfacial shear strength was low (<4MPa in the case of Y_2O_3/Al_2O_3), and was reduced further by oxidation of the composite of only a few hours at 1000°C. The oxidation mechanism appeared to be by 'piping' along the interface from exposed fibre ends. Fibre cores are also damaged by the same process. After 25 hours of oxidation at 1000°C, the interfacial shear strength of the Y_2O_3/Al_2O_3 SRBSN composites had dropped to less than 1MPa, only a residual frictional component being present. The interface after 1000 hours was highly oxidised, the carbon rich layers being largely removed, and only the reaction layer, and the silicon rich zone remaining intact. The higher silicon carbide content of these regions presumably makes them much more resistant to damage than the predominantly carbon rich layers. The MgO additive samples had higher interfacial shear strengths, however it is not known whether this is as a result of reaction at the outer layer, or due to another mechanism such as thermal clamping (as a result of differential thermal expansion of the fibre and matrix). If the thermal expansion of the MgO additive matrix was higher than that of the Y_2O_3/Al_2O_3 additive matrix there would be a greater likelihood of thermal clamping of the fibre by the matrix on cooldown from the sintering temperature. The thermal expansion of the bulk matrix is determined by the thermal expansion of the β-Si_3N_4 grains, the thermal expansion of the glassy grain boundary phase, and the volume fractions of both phases. The reaction at the interface causes chemical bonding between the matrix and outer carbon rich layer (as observed in the TEM), but the interface between the inner layer and the SiC sheath would appear to be very weak. Failure usually occurs at this interface during micro-mechanical (indentation) testing, macro-mechanical testing (bend, tensile etc.) and TEM specimen preparation. This implies that chemical bonding cannot be totally responsible for the increase in

interfacial shear strength.

The interface in CMC's is usually regarded as crucial in terms of the mechanical behaviour during fracture, a low cohesive chemically stable interface, being regarded as a goal. In borosilicate (Pyrex) glass/Nicalon composites, the reaction between the fibre and matrix during processing creates a layer of carbon (with a graphitic like structure), with desirable low strength and frictional characteristics [64]. The penalty of a carbon layer at the interface is the susceptibility of the composite to oxidation at the interface, and consequent change in mechanical behaviour. This has been observed in glass/Nicalon systems where replacement of the carbon layer by silica gives a greatly increased bonding between the fibre and matrix. The mechanical behaviour of the composite is radically altered, with a linear elastic region followed by a catastrophic brittle failure. The typical thickness of the graphitic layer is around 50nm, two orders of magnitude thinner than the twin layers on the SCS-6 fibres. This may explain the apparent stability of the SiC/ SRBSN composites, a silica bridge across a 3μm gap being more difficult to form than a 50nm bridge in glass/Nicalon composites.

6.0 MECHANICAL BEHAVIOUR

Composite samples were mechanically tested in bend and tension at room temperature and in bend at high temperature. Acoustic emission data were logged during room temperature tests and plotted on the stress/strain graphs. A minimum of three test bars were used for all tests, with more bars being used for some test conditions (particularly room temperature bend tests). Early RBSN and SRBSN work (MgO and 6wt%Y_2O_3/ 4wt%Al_2O_3) was only carried out at room temperature, a more comprehensive test program was carried out for the 6wt%Y_2O_3/2wt%Al_2O_3 SRBSN, and SEM studies of fracture surfaces were carried out on samples from each test condition.

The mechanical behaviour of the 6%Y_2O_3/2%Al_2O_3 SiC/SRBSN composite was then compared to theoretical models (such as the ACK theory) for room temperature and elevated temperatures.

6.1 RBSN MATRIX COMPOSITES

All testing was carried out in three point bend at room temperature, on unidirectional specimens, and no acoustic emission data were obtained. The results are shown in fig.6.1, early RBSN matrix composites, which were laminated by warm pressing prior to nitriding having poorer properties than material which was laminated by hot pressing prior to nitriding. Shear stresses are induced in a bend test bar when under load, and poor lamination of the warm pressed materials makes them likely to fail in interlaminar shear, which lowers the apparent bend strength value. Hot pressed materials are laminated well, and consequently fail in a tensile manner at the outer surface, and at a higher apparent bend

stress level. An example of a stress/deflection curve is shown in fig.6.2

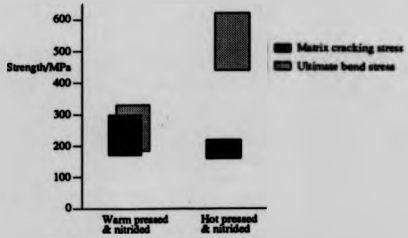

fig.6.1 Room temp, three point bend results for RBSN matrix composites.

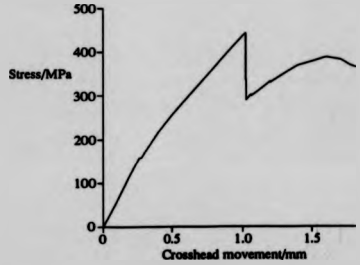

fig.6.2 Stress/deflection curve for an early RBSN matrix sample

Microscopy of the fracture surface was carried out on the hot pressed samples to study the fibre/matrix debonding and compare fracture behaviour to the theory outlined in 2.0. Fig.6.3 shows part of a specimen that has failed by delamination, the outer carbon layers on the SCS-6 fibre remaining attached to the matrix. Fibres debonded from the matrix are

shown in fig.6.4, in this case retaining the outer carbon layers. The fracture surface of a fibre is shown in fig.6.5, the carbon core has pulled out of the fibre as well as the fibre debonding and pulling out of the matrix. An example of fibre pullout at a fracture surface is shown in fig.6.6.

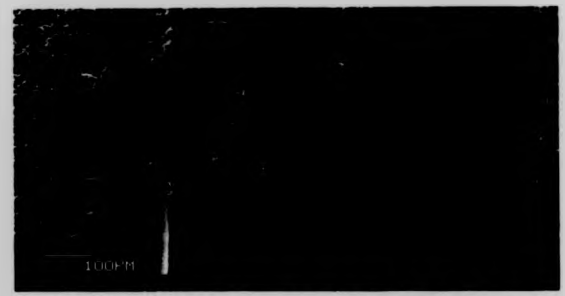

fig.6.3 Delaminated specimen, showing outer carbon layers adhering to the matrix

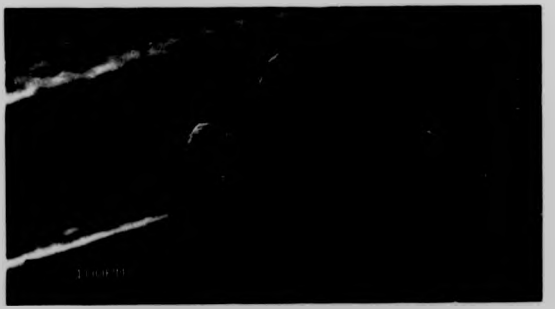

fig.6.4 Debonded fibres with intact outer carbon layers

fig.6.5 Fibre fracture surface, showing pullout of inner carbon core

fig.6.6 Fibre pullout at fracture surface of bend test sample

Composites containing HPZ fibres in an RBSN matrix were also tested, and were found to be very weak and brittle. The material was too weak to allow the preparation of polished samples for SEM examination, and the only microstructural investigation carried out was on fracture surfaces of bend test bars. Examination of the fracture surface showed that the fibres had been severely degraded by the nitriding process, a high magnification view of the fracture surface of a bend test bar is shown in fig.6.7. Heat treatment by Dr.V.S.R.Murthy of the fibres in pure (white spot) nitrogen for similar times and temperatures to that used in nitriding showed no such degradation, however a repeat nitriding run on the fibres alone destroyed them completely. It would appear that the hydrogen addition to the nitriding mixture is responsible for the degradation.

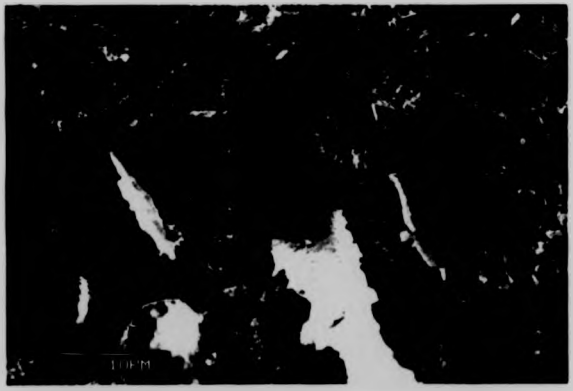

fig.6.7 Fracture surface of RBSN/HPZ fibre bend test bar

Problems in fabrication of composites using small diameter fibres and particulate based matrices include adequate penetration of the fibre tows and abrasive damage by the matrix particles. In glass matrix composites, the glass is assumed to be mobile enough at the processing temperature to avoid these problems. In the HPZ/RBSN composites fabricated, the matrix appeared to have penetrated the gaps between the fibres (in fig.6.7 the original outline of the fibre sections can be seen in the matrix, although the fibres themselves have been severely degraded by the nitriding process.

The samples all exhibited composite like behaviour to some extent, the early warm pressed samples suffered from delamination during bend testing, which lowered the apparent strength. Matrix cracking strength of the SCS-6/RBSN composite was generally less than 300MPa and was quite variable in early warm pressed samples. Some oxidation testing was also carried out on the SCS-6/RBSN material, and severe cracking of the matrix was seen after 72 hours at 1000°C in air. No further study of the RBSN matrix material was carried out because of the poor oxidation resistance of RBSN compared to dense (i.e. hot pressed or sintered) silicon nitride, and the apparent lack of stability of currently available small diameter fibres during the nitriding process. The methods developed for composite fabrication (e.g. tape casting, nitriding etc.) were directly applicable to the SRBSN matrix composites, which were investigated during the remainder of the program.

6.2 SRBSN MATRIX COMPOSITES - Room Temperature Behaviour

Investigation of the SRBSN matrix composites consisted of room temperature characterisation in bend, tension and short beam shear, high temperature characterisation in bend for zero time and in creep/stress rupture. Room temperature characterisation of oxidised samples was also carried out for oxidation temperatures up to 1400°C and times up to 1000 hours. All results shown are from the 6wt%Y_2O_3/2wt%Al_2O_3 additive SRBSN matrix composites (batch 27) unless otherwise stated.

6.2.1 Room temperature bend testing

Room temperature three point bend testing was carried out for samples selected from most of the 6wt%Y_2O_3/2wt%Al_2O_3 plates produced in order to gain a) average values for matrix cracking stress and ultimate bend strength and b) an idea of the scatter in properties.

The matrix cracking stress (σ_{mu}) was taken to be the point of departure from linearity of the stress/deflection curve, the average matrix cracking stress being 651.1 MPa for the 6%Y_2O_3/2%Al_2O_3. The ultimate bend strength (σ_{ub}) was taken to be the peak stress reached during the test, after σ_{mu} had been reached, the average value being 713.2 MPa (from an total of 15 specimens). Weibull moduli (m) were calculated for the matrix cracking stress and ultimate bend stress, and were 5.7 and 8.7 respectively. A combined Weibull plot (ln(ln(P)) vs ln(σ)) for both is shown in fig.6.8, the low values for one or two specimens reducing the slope (m) of the best fit straight line, and reducing the slope (m), particularly for the matrix cracking stress. These values of m are poor compared to HIPped silicon nitride where values in excess of 20 are attainable.

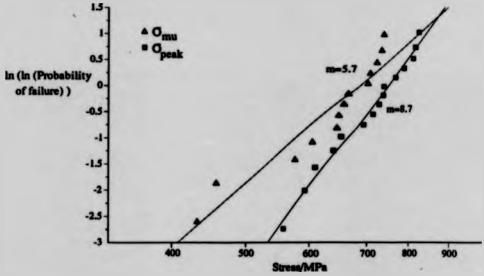

fig.6.8 Combined Weibull plot for matrix cracking stress and ultimate bend stress of 6%Y_2O_3/2%Al_2O_3 additive SiC/SRBSN composite, showing the effect of a few low results on the Weibull modulus.

Fig.6.9 shows a stress/deflection curve (specimen deflection was inferred from the crosshead movement) for a 6%Y_2O_3/2%Al_2O_3 bend specimen. The initial stress/deflection curve is linear, up to a matrix cracking stress (a) of 732MPa, after which there is a drop in stress. The stress then continues to rise, the slope of the curve being lower than prior to the matrix cracking stress, and reaches a peak (b) of 820MPa. The stress then falls in a stepwise manner (c) as the deflection increases, the stress at a deflection of 3mm being approx. 200MPa. The reduction in the slope of the curve between (a) and (b) can be explained by a reduction in modulus of the sample as the matrix cracking reduces the effective cross-section.

Acoustic emission from samples was audible as a series of clicks after the matrix cracking stress had been reached (indicated by a deviation from linearity on the stress/deflection curve).

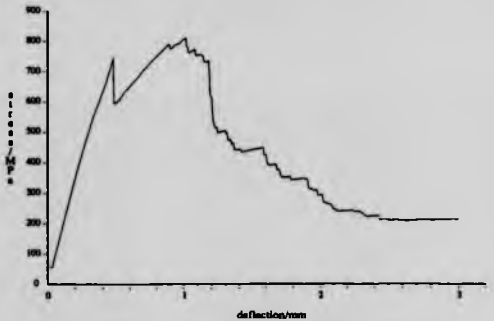

fig.6.9 Stress/deflection curve for 6%Y_2O_3/Al_2O_3 bend test sample

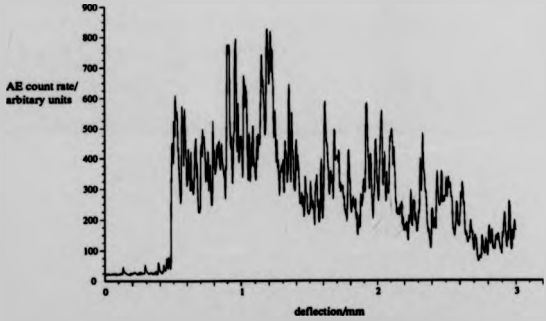

fig.6.10 Corresponding acoustic emission during bend test

Fig.6.10 shows the acoustic emission from the same sample (events were counted within a 0.1s window, the scale on the y axis is in arbitary units). The initial acoustic emission rate is low, however when the matrix cracking stress is reached, there is a sharp

increase in emission. This suggests that prior to the matrix cracking stress, very little, if any damage is being done to the composite (events counted before matrix cracking are probably due to friction between the specimen and the rollers, as coating the rollers with PTFE spray reduced the acoustic emission). Some of the peaks in the acoustic emission trace can be linked to indicated features on the stress/deflection curve, major cracking events having correspondingly large acoustic emission rates.

The sharp load drop after matrix cracking was initially thought to be due to a thick layer of matrix on the tensile surface of the bend test specimen failing in a catastrophic manner, the crack stopping at the first fibre layer. A number of samples were tested after grinding off the matrix layer at the surface and showed a similar behaviour, therefore another mechanism was sought to explain the sharp load drop. The actual failure mechanism at this stage in the stress/deflection curve is more likely to be a combination of an initial tensile failure at the outer surface followed by crack deflection as it approaches the neutral axis of the bend test bar. The difficulty in interpretation of bend test results encouraged the development of a simple method for tensile testing the material.

6.2.2 Room Temperature tensile testing

Dogbone shaped composite test pieces were made by grinding a gauge section in samples cut to the same dimensions as bend test pieces. Aluminium end plates were glued using epoxy, set screws clamping the test piece between the plates and the end plates gripped in conventional tensile testing grips. Further details of the test piece design are given in chapter 3. A batch of seven samples (all from plate K, 6% Y_2O_3/Al_2O_3) were tested, giving an average matrix cracking stress of 232MPa (standard deviation 52MPa), and an average peak stress of 413MPa (standard deviation 28MPa). Fig.6.11 shows a

tensile load/deflection curve from one of the tests with the corresponding acoustic emission data in fig.6.12.

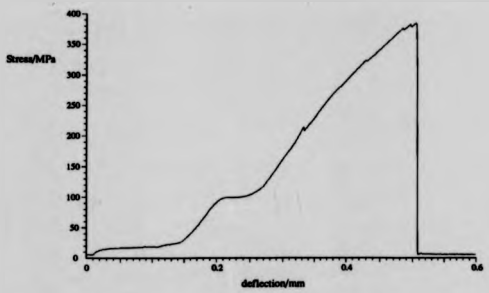

fig.6.11 Stress/deflection curve for room temperature tensile test.

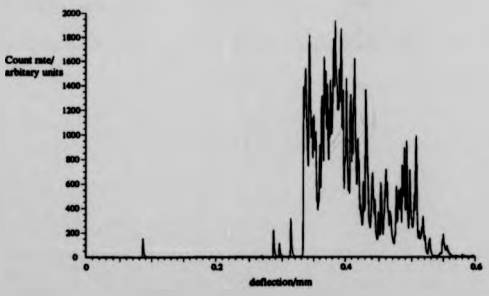

fig.6.12 Corresponding acoustic emission data for tensile test

The initial part of the stress/deflection curve is not linear and was attributed to shear

deformation of the epoxy adhesive used to glue the aluminium end tabs to the specimen (the correct curve is shown as a dashed line). The matrix cracking occurs at a stress of 214MPa, only $^1/_3$ of the value obtained in the bend test case. For some of the tests, a strain gauge was attached to the tensile test piece gauge length, to obtain a more accurate value of strain than inferred from the crosshead movement. The strain gauge indicated a bending component in the test piece, even for a zero applied stress, which was induced by misalignment of the load train. This additional bending stress had the effect of producing a higher localised stress in the sample than was indicated by the load cell output, causing the sample to fail at a lower apparent stress. Another contributing factor to the lower apparent strength of the tensile test samples is that a larger volume of material is under stress (compared to a bend test, where only the tensile surface region is subjected to the maximum stress). The probability of a flaw being present in the stressed volume increases as the volume increases, with a consequent lowering of the apparent strength. For monolithic ceramics, this volume effect has been well characterised for bend testing [9] .

Three initial tests were carried out using samples from a composite plate (plate E) that had not been fully densified due to being pressed at a lower temperature during the development of the tensile test method. A lower matrix cracking stress was expected due to porosity, however one of the samples gave a matrix cracking stress of 430MPa (and a peak stress of 667MPa), which is much closer to the values obtained in the bend testing. It is likely that the high strength measured for this sample is due to better alignment (causing lower induced bend stress) than the other samples tested (the other two samples from the same plate gave similar values to the fully densified material).

The final failure is more catastrophic in the tensile case, the load dropping down to zero, whereas in the bend case, the sample continued to support a load after severe deformation.

This is due to the effective strain in the bend sample varying through the sample thickness, and a shift in the neutral axis as the test is carried out. Tensile fracture surfaces (fig.6.13) exhibited a far greater degree of fibre pullout compared to bend fracture surfaces (fig.6.14) which generally showed little pullout. Higher magnification views of the fracture surfaces are shown inset, the fibre debonding process (detachment of the carbon rich layers from the SiC sheath) being common to all samples (including RBSN matrix composites). In the tensile fracture surface, debonding and pullout of the central carbon core occurs for a number of fibres.

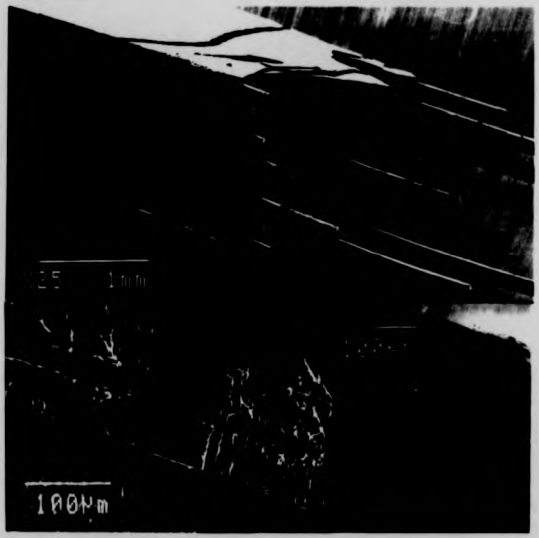

fig.6.13 SiC/SRBSN tensile fracture surface

fig.6.14 SiC/SRBSN bend fracture surface

6.2.3 Discussion of room temperature bend and tensile behaviour

The sharp load drop on matrix cracking observed during bend tests can be explained by the presence of interlaminar cracking, the crack path progressing from the surface, and being diverted along the fibre direction. This is a good example of the danger in using composite bend data exclusively, without resorting to tensile testing, which although more complex to perform, gives more reliable and easier to analyse results. Tensile testing of brittle materials is difficult to perform because bend stresses induced in the sample cause

the sample to fail at a reduced apparent stress. Bending stresses can be due to inaccurate testpiece machining, poor load train alignment or a combination of both. The reliability of the present tensile test results is considered to be poor, due to the bending of the sample. Bend stresses were detected by a strain gauge attached to the side of the sample, a strain was indicated when the apparent applied load was zero. The testpieces were made using a profiled diamond wheel to generate the gauge length, but accurate positioning of the wheel on the testpiece was difficult. It is therefore likely that part of the bending induced was due to poor testpiece machining. Universal joints were used in the load train, but due to the size of the grips used they were positioned at a distance from the specimen, and could not remove any bending moment between them. In the ideal situation, the universal joints are as close as possible to the ends of the testpiece.

Using values obtained from stress/strain curves, interfacial shear stress measurements, fracture surfaces and crack spacings, the behaviour of the material can be compared to the models discussed in chapter 2.

Examination of fractured specimens from room temperature tensile tests indicate that the material is close to the critical value for the transition between single and multiple cracking. Equation 2.3 gives the neccessary conditions for multiple fracture to occur, namely

$$\sigma_{fu} V_f > \sigma_{mu} V_m + \sigma_f' V_f.$$

Tensile tests carried out initially were on substandard material (plate E) with a low density, thought to be due to a low hot pressing temperature. The matrix cracking stress was expected to be correspondingly lower than the 'standard' material (tested in bend), and some multiple cracking was seen. The occurrence of single cracking in other cases (plate

K) would seem to indicate that the material is on the borderline between the single and multiple cracking regime. If for example the matrix cracking stress was lowered, the inequality would be shifted into the multiple cracking region in fig.2.4. The strength of the fibre in the processed composite is unknown, however for the best sample (from plate E), an estimate of 2669MPa can be made from the peak stresses measured in tensile testing (for the poorly processed material). The matrix cracking stress in the same sample was 430MPa, from the stress measured during tensile testing at the departure from linearity of the stress/strain curve. The stress in the fibre necessary to exceed the matrix strain to failure (σ') was calculated by multiplying the fibre Young modulus (391GPa) by the strain to failure of the matrix (matrix cracking stress/matrix Young modulus). These estimates gave:

$$\sigma_{fu}V_f = 2669 \times 0.25 = 667\text{MPa}$$

$$\sigma_{mu}V_m = 430 \times 0.75 = 322.5\text{MPa}$$

$$\sigma'V_f = 611 \times 0.25 = 152.8\text{MPa}$$

As 667>322.5+152.8 the inequality must be true, and multiple matrix cracking should occur, which was observed in the sample.

Using the same model and calculation method, the inequality for the 'correctly' processed specimens (plate K) can be found. A lower fibre strength of 1653MPa was found from the average peak composite strength values. It was assumed that the matrix microcracking stress measured (232MPa) was too low, due to the specimen bending previously mentioned, so a value of 400MPa was chosen (the strength of the correctly processed matrix should be at least as high as the substandard material). Using a σ_{mu} value of 400MPa, a value of 521MPa was calculated for σ'. Therefore

$$\sigma_{fu}V_f = 1653 \times 0.25 = 413.25\text{MPa}$$

$$\sigma_{mu}V_m = 430 \times 0.75 = 322.5\text{MPa}$$

$$\sigma'V_f = 521 \times 0.25 = 130.3\text{MPa}$$

As 413.25<322.5+130.3, the sample could be expected to have a single matrix crack, and this behaviour was observed in most of the samples tested (from that plate).

The strength of the fibres in the 'correctly' processed plate (K) seem to be lower than in the plate processed at a lower temperature (E). The effect of heat treatment on fibres has been discussed in chapter 2, fig.2.9 showing a rapid decrease in strength with increased heat treatment temperature above approximately 1500°C. As direct measurement of fibre strength within the composite is not possible, fibre heat treatment studies give a guide to the degradation expected.

From equation 2.5, the minimum matrix crack spacing, x, is given by

$$x=(V_m/V_f)\sigma_{mu}r/2\tau$$

Using a value of 400MPa for σ_{mu}, 0.25 for V_f, and 2MPa (from the indentation test results in chapter 5), an estimate of x=2.25 cm can be made. This would partly explain the lack of multiple matrix cracking observed in most of the bend and tensile testpieces, where the dimensions of the stressed region or gauge length were less than 2.25cm. In systems with small diameter (15μm) fibres, the expected crack spacing is lower, due to the radius term in the above equation, as well as a lower value for σ_{mu}.

Fibre pullout was observed in all tensile tests, the amount of pullout varying (the samples from plate E had a greater amount than those from plate K). Fibre pullout is one of the energy absorption processes that contributes to the work of fracture (WOF) during the failure of composites, equation 2.11 giving the relationship between energy absorbed and

average pullout length l_p , τ, r and V_f.

$$\gamma_f = \tau V_f l_p^2/r$$

For the samples tested, the pullout length was estimated to be 1.5mm, giving an energy contribution of 15 kJ/m^2. The frictional energy absorbed by the sample during fibre pullout is dissipated as heat and acoustic emission (both from frictional sliding at the fibre/matrix interface).

When fibres break, stress relaxation occurs, again absorbing energy and contributing to the work of fracture. Fibres breaking also create acoustic waves If a relaxation length (l_r) of 1cm is chosen (approx. half the minimum matrix crack spacing), the energy absorbed is given by

$$\gamma_f = \sigma_{fu}^2 V_f l_r/2E_f$$

For the samples tested, this energy contribution was estimated to be 8 kJ/m^2, giving a total work of fracture of approx.23 kJ/m^2.

An estimate of the work of fracture was made by integrating the area under the curve for the load/deflection curve for the tensile test in fig.6.11. This was carried out by dividing the area into rectangles and triangles and summing the individual areas to obtain a total energy absorption during fracture of 0.49J. The effect of shear of the epoxy bond between the sample and end plate was ignored in the calculation, the linear part of the stress/ deflection curve being extrapolated to the x axis. The work of fracture per m^2 was then found by dividing by the sample cross sectional area, to give a value of 89 kJ/m^2. The main source of error in the above estimate is the assumption that the crosshead deflection on the test machine respresented the actual specimen strain. As the load train is not infinitely stiff

and further deformation of the epoxy at the ends of the sample have not been taken into account, the real work of fracture is lower, approaching the energy absorption calculated from the models above.

Several conclusions can be reached from the above analysis. Firstly, the matrix cracking stress σ_{mu} is higher than for other CMC systems, such as glasses, where values between 100 and 300MPa are typical. This is due to the intrinsically higher strength of dense silicon nitride. Secondly, the crack spacing (although not measured directly) was estimated to be >2.25cm, which is relatively large compared to SiC/SiC (produced by the CVI process) and glass matrix composites where spacings<1mm have been observed. Thirdly, the fibre strength is lower in the as processed condition than in the as received condition, the typical reduction being of the order of 50%. The strength of small diameter fibres such as Nicalon and Tyranno is also reduced during composite processing, either by mechanical damage or by microstructural changes. Neither of these fibres would survive the 1700°C processing used to fabricate the SRBSN matrix composites. Finally, the fibre volume fraction V_f in the current material is too low to allow multiple cracking to occur, variations in V_f from plate to plate giving rise to the occasional example of multiple cracking.

The mechanical behaviour of the materials investigated was radically different to that found in monolithic examples of the silicon nitride matrix and the silicon carbide fibre. The fracture behaviour of the material at room temperature can be characterised by an initial linear increase in strain with applied stress, a matrix cracking stress comparable to that observed in monolithic silicon nitride, a non-linear increase in strain with applied stress reaching a peak stress, followed by a sharp load drop (in a tensile test) or a stepped decrease in stress (in a bend test) with increasing strain.

6.2.4 Effect of fibre angle on flexure properties

The effect of fibre angle on the flexure properties of unidirectional material was investigated, using specimens cut from the same 50x50mm plate. The length of the specimens was in some cases less than the standard 50mm specimen, and a outer span of 30mm was chosen for testing in three point bend. The width of the specimens was variable due to the way they had been sliced. Modulus values were calculated by fitting a straight line to the linear portion of the load deflection curve, and using the equation in section 3.4 to convert to GPa. Stresses were calculated using the three point bend equation, also in 3.4. The results were plotted against angle, shown in fig.6.15. The 0° values were lower than expected due to the specimen being on the edge of the plate so the average results from the previous testing of a number of 0° specimens are shown, to give a more representative value. The general form of the modulus curve is the same as that depicted in 2.1 for a carbon epoxy unidirectional laminate, although tensile testing is necessary for a more accurate comparison with theory. The difference in modulus between silicon nitride and silicon carbide is not as great as the carbon/epoxy example given in 2.1, and leads to smaller differences in longitudinal and transverse modulus. A theoretical modulus variation with angle function was plotted (fig.6.16), using the elastic constants E_1=300 GPa, E_2=170GPa, (both from the measurements made) and assuming values for the bulk modulus (G_{12}) of 70GPa, and the Poisson ratio (υ_{12}) of 0.25. The measured modulus results are also shown in fig.6.16 for comparison.

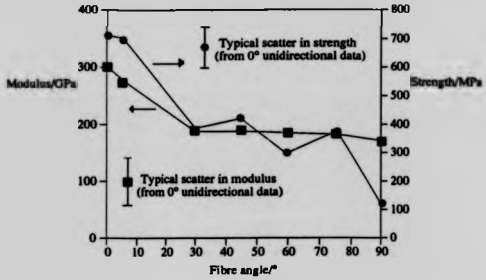

fig.6.15 Effect of fibre angle on properties of unidirectional material

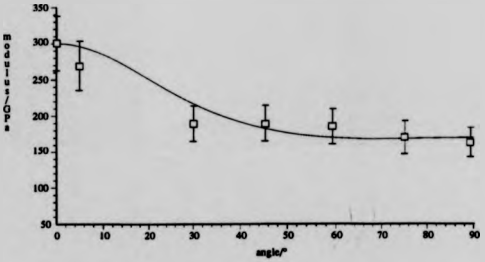

fig.6.16 Comparison of modulus values with theoretical prediction

Error bars were derived from the standard deviation measured for the unidirectional test results measured for samples from other plates, and appropriately scaled for each modulus value. There is fairly good agreement with the theoretical prediction, in spite of the crudity of the experiment, in which the modulus values are inferred from crosshead movement, rather than measured directly (using strain gauges, extensometers etc.).

The transverse strength can be expected to be low because the low fibre/matrix interfacial strength allows very little load to be transmitted across the interface. The composite becomes equivalent to monolithic silicon nitride with 150μm holes dispersed through it, acting as stress raising flaws.

6.3 SRBSN Matrix Composites - Elevated Temperature Behaviour

6.3.1 Elevated temperature bend testing

SiC/SRBSN specimens were tested in four point bend at elevated temperature at 1000°C, 1200°C and 1400°C. The mechanical properties were found to decrease with increasing temperature, and the stress/deflection curve indicated that the matrix exhibited some plasticity at 1400°C. The stress/deflection curves for all three temperatures, with a room temperature curve for comparison are shown in fig.6.17. It is difficult to establish a value for the matrix cracking stress at 1400°C, due to the plasticity of the matrix, however a value of approx. 160MPa was estimated from the stress/deflection curves.

At high temperatures, it was not possible to obtain acoustic emission data (with the piezoelectric transducers used for room temperature testing), however some audible cracking was heard between the matrix cracking stress and the ultimate bend stress.The matrix cracking stress and ultimate bend strength are shown as a function of temperature in fig.6.18, the error bars shown indicating the minimum and maximum values obtained (only three samples were tested for most of the conditions making statistical analysis difficult).

At elevated temperatures below 1200°C, the behaviour is similar to that observed at room temperature, but with a tendency for a sharper load drop after the peak stress is reached (all elevated temperature testing was carried out in bend). At 1400°C the material exhibited plasticity, and the previously observed distinct matrix cracking event did not occur, however a plastic deformation process appeared to take place, the stress-strain curve decreasing in slope, prior to a sharp load drop and failure.

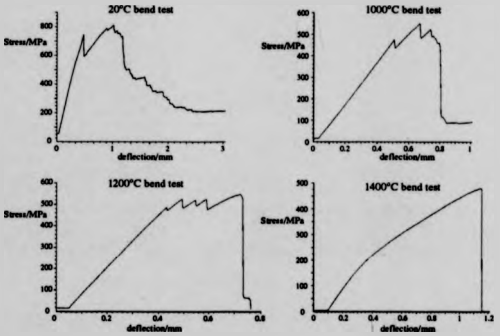

fig.6.17 Stress/deflection curves for RT, 1000°C, 1200°C and 1400°C in bend

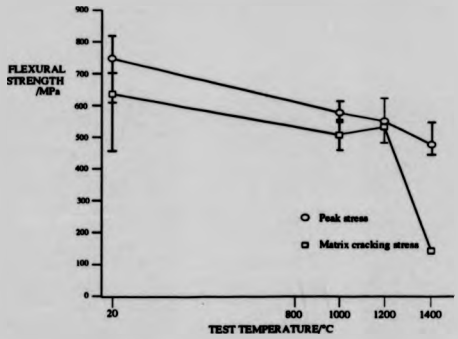

fig.6.18 Variation of flexural properties with test temperature

Elevated temperature behaviour is similar in character to that at room temperature, the degradation in non-catastrophic behaviour during failure being explained by a reduction in the strength of the fibre at elevated temperature (if the as produced strength at 1000°C is scaled to take the reduction in properties during processing into account, this results in a fibre strength of approx. 1300MPa). The effect of this would be to degrade the ability of the fibres to withstand the extra load put upon them after the matrix had cracked.

Fig.6.19 shows a comparison of the matrix cracking and peak bend strength of the SiC/SRBSN composite with monolithic silicon nitride (Y_2O_3 or MgO additive, data from [79]). The variation in peak strength of the composite with temperature is roughly comparable with the MgO additive monolithic silicon nitride, the matrix cracking stress being lower. Y_2O_3 additive materials have better higher temperature properties than MgO additive materials because the Y^{3+} ion produces a viscous grain boundary phase. In contrast, the lower valency Mg^{2+} ion produces a grain boundary phase with lower

viscosity.

In order to gain maximum potential from the material, the fibre volume fraction must be high enough to allow multiple matrix cracking to occur. The low interfacial shear strength is likely to remain in the region below 5MPa, and the minimum distance between cracks will still be high (>11 mm) compared to the model systems cited by Aveston, Cooper and Kelly in [34].

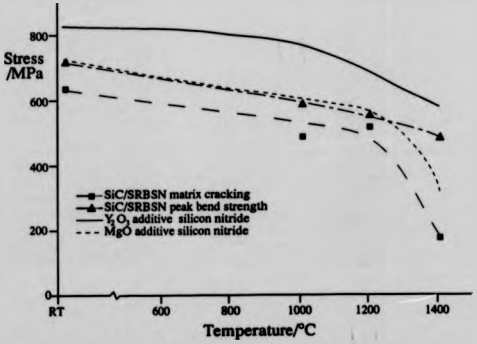

fig.6.19 Comparison of SiC/SRBSN matrix cracking stress and bend strength with Y_2O_3 and MgO additive monolithic silicon nitride (monolithic data from [79]).

6.3.2 Effect of oxidation time and temperature

Oxidation testing of samples was carried out for 100 hours and 1000 hours at 1000°C, 1200°C and 1400°C. Samples were weighed before and after oxidation, and then tested at room temperature in three point bend. The variation in bend properties with oxidation time

and temperature is shown in fig.6.20. For 100 hours, there is a decrease in strength for all three temperatures, however it appears that room temperature strength after oxidation at 1200°C is less damaging for 1000 hours than either 1000°C or 1400°C. The scatter in the results, combined with the small number of specimens for each condition make it difficult to draw firm conclusions, and further investigation, comparing stress/deflection curves and fracture surfaces was carried out.

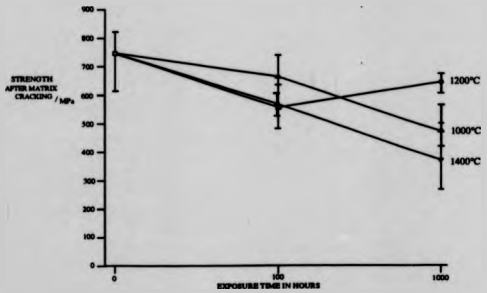

fig.6.20 Effect of oxidation on room temperature bend strength

The stress/deflection curves for the oxidised samples did not show the same characteristics as the 'as fabricated' samples tested at room temperature. In particular, the acoustic emission appeared to start as soon as load was applied to the sample, rather than starting after the matrix cracking stress had been reached. Also, the samples appeared to fail in a more brittle manner, with less load carrying capability after the matrix had cracked than as produced material. An example of a stress/deflection curve for sample after a 1400°C, 1000 hour exposure, together with the associated acoustic emission data is shown in fig 6.21. All samples showed a sharp load drop at the matrix cracking stress, continual

deflection resulted in an increasing load, but not reaching the original matrix cracking value again, and in the 1400°C case, the load tailed off without increasing after the load drop.

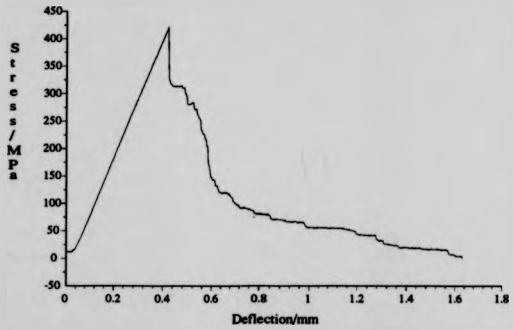

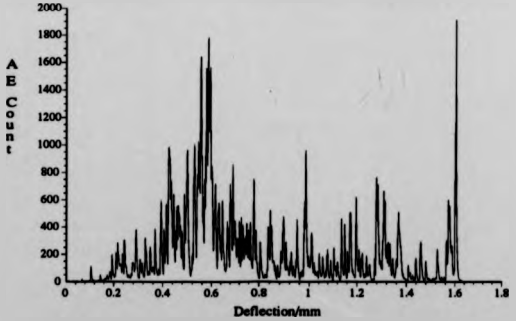

fig.6.21 Stress/deflection curve and acoustic emission data for 1400°C,1000 hour sample

The oxidation resistance of the material has been investigated at temperatures between 1000°C and 1400°C at times up to 1000 hours. A steady decrease in ultimate composite strength was observed with increasing time for samples oxidised at 1000°C and 1400°C. Samples oxidised at 1200°C retained a higher proportion of their strength, with 1000 hour samples having a higher average strength than 100 hour samples. The acoustic emission from oxidised samples below the matrix failure stress is consistent with the microstructural results, the damaged carbon layers allowing movement of the fibre relative to the surrounding matrix, creating acoustic events. The outer carbon rich layers are deposited on the fibre to provide a suitable interface for the metal matrices for which the fibres are intended, and also to seal exposed grain boundaries which act as flaws, lowering the strength of the fibre. Whether or not this is the precise mechanism that occurs, the fibres without carbon rich layers (either uncoated or removed by oxidation) have lower measured strengths than the standard SCS-6 fibre. It is therefore likely that at least part of the reduction in composite strength observed is as a result of fibre degradation by oxidation damage of the outer carbon rich layers, causing the original grain boundaries to become exposed. Exposure to high temperatures has also been shown to have a damaging effect on fibres, possibly via grain growth mechanisms. However the oxidation exposure testing carried out was below 1400°C, and little grain growth can be expected at these temperatures in pure silicon carbide.

6.3.3 Creep and Stress Rupture Testing

Creep testing was carried out in four point bend at 1300°C, to compare creep behaviour with that reported for similar silicon nitrides in monolithic form. Creep in ceramics [2] is

generally described by the empirical law

$$\dot{\varepsilon} = A e^{-E/RT} \sigma^n$$

where $\dot{\varepsilon}$ is the creep rate, A is a constant, E is the activation energy of the creep mechanism, R is the universal gas constant, T is the temperature (K), σ is the applied stress and n is a constant known as the stress exponent. The creep rate $\dot{\varepsilon}$ is derived from the part of the creep curve (strain vs time) when the slope is approximately constant (the slope initially decreases exponentially after the load is applied and approaches a constant creep rate after typically several tens of hours). The samples were put under nominal stresses of 150,200,250 and 300MPa, the exact value of the outer fibre stress in the four point bend bar being dependent on the value of n, during a creep experiment [66]. Samples were tested as they became available, hence the first two samples were from a different plate to the others. The first two samples were tested under nominal stresses of 200 and 250MPa, the resulting creep curves are shown in fig.6.22.

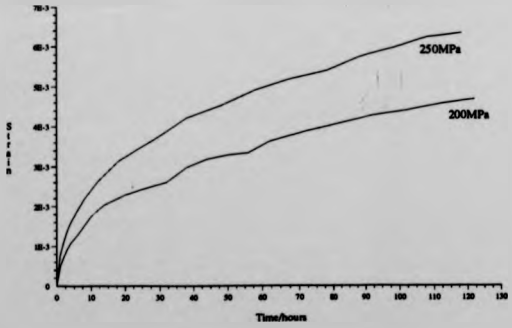

fig.6.22 Creep curves from plate 1 specimens

When the 150MPa and 300MPa tests were carried out, the creep rate measured was significantly higher than for the first tests, the samples being taken from a second plate. An additional run at 200MPa was carried out using a third specimen from the second plate, and all three creep curves are shown in fig.6.23.

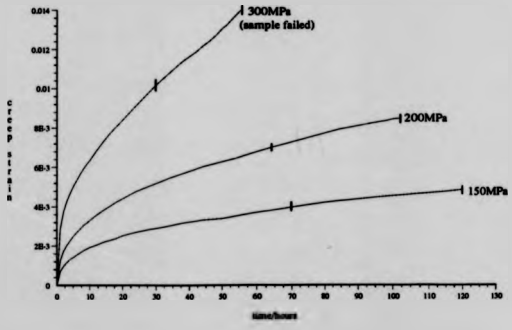

fig.6.23 Creep curves obtained from specimens from the second plate

The creep curves all exhibited a high initial deformation rate reducing exponentially reaching an approximate 'steady state' after 60 hours (the 300MPa sample reached a steady state creep rate after approx.30 hours and failed at 55.3 hours).

The stress exponent n was calculated by plotting load point deflection rate against the applied load on a log-log graph, the slope of the line being equal to n [66]. The value obtained for n was then used to calculate the actual stress and strain rate for each specimen, and these were then plotted on a log-log graph. A value of n=1.73 was obtained for the creep exponent for plate 1, and a value of n=3.07 was obtained for plate 2. The differences in creep behaviour between the two plates can be seen in fig.6.24, in which creep results

for MgO additive HPSN and a developed Y_2O_3/SiO_2 additive HIPped material are shown for comparison.

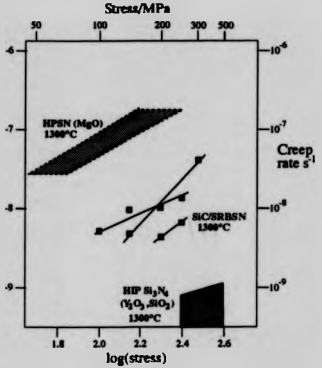

fig.6.24 Results from present work compared to other silicon nitrides

6.3.4 Stress Rupture Testing

Stress rupture testing was carried out between 200 and 400MPa in steps of 50 MPa at a temperature of 1300°C, results from the creep tests in which specimen failure occurred being used as stress rupture results. Testing was carried out using the creep rig previously used and the results (plotted on a log-log scale) are shown in fig.6.25. A value of 500MPa was used for the zero time failure stress, using a value estimated from the monotonic testing previously carried out at 1200°C and 1400°C. As only one specimen was tested for each stress, no measurement of the scatter in the data could be made (the typical scatter in the monotonic tests carried out was ±50MPa). The curve shows no indication of 'bottoming out' at a threshold level above 200MPa, whereas HIPped dense monolithic silicon nitride

(Y_2O_3/SiO_2 additve) [74] had a threshold stress of approx. 400MPa (at 1300°C) below which no failures occurred, even after times as long as 1000 hours (6.55 on the x-axis in fig.6.25).

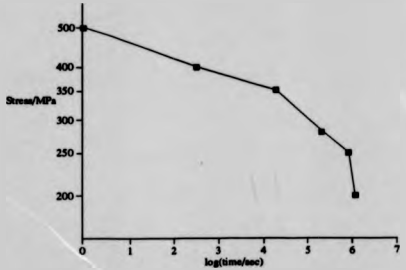

fig.6.25 Stress rupture behaviour of SiC/SRBSN at 1300°C

Recent work [80] on stress rupture testing of monolithic silicon nitride has shown that the Larson-Miller curve fitting method can be used to map the overall time/temperature behaviour against stress on one graph. The Larson-Miller method [81] is used extensively for lifing metals (e.g. turbine blade alloys), and uses the equation

$$P = T \log(C+t)$$

where P is the Larson-Miller parameter, T is the thermodynamic temperature, and t is the stress rupture life. P is plotted against the stress σ to obtain a stress rupture map, incorporating stress, time and temperature on one graph. A value of 20 for the constant C has been derived empirically, and is valid for the majority of nickel based alloys. For silicon nitride, the value of C given in [80] is 30, allowing a comparison between nickel

based alloys and the SiC/SRBSN composite investigated in this work. The typical ultimate tensile strength of the material is approximately two thirds of the ultimate bend strength, and the SiC/SRBSN stress rupture data was scaled accordingly. The comparison is shown in fig.6.26, and although highly speculative (due to the nature of the testing method employed), shows a dramatic increase in stress rupture performance over conventional materials, particularly at low stresses.

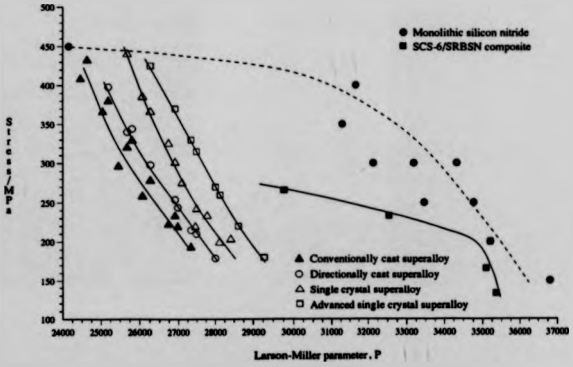

fig.6.26 Larson-Miller plot of nickel based alloys and SiC/SRBSN (monolithic data from [80], superalloy data from Rolls-Royce)

The constant in the Larson-Miller equation is found by plotting data for different temperatures on the same graph, and adjusting the constant C so that all the data lies on a straight (for most metals) line. Data for the conventionally cast superalloy in fig.6.26 has some spread, and would ideally be plotted using a different constant to the other superalloys, however a direct comparison between the different materials could not then be

made; this is also the reason for the spread in the monolithic silicon nitride data from [80]. There is also a pronounced knee in the ceramic stress rupture data, which probably reflects the different damage accumulation processes occuring, compared to the superalloys. The dependance of the Larson-Miller parameter on stress is much greater for ceramics than for the superalloys plotted in fig.6.26, although each step in development of blade superalloy (with a move to the right in fig.6.26) represents a cost of several million pounds for research and development. The benefits of using ceramic materials in applications where stress rupture is the dominant failure mode can therefore be appreciated.

6.3.5 Discussion of Elevated Temperature Behaviour

Creep testing of the material gave results which were encouraging, considering the lack of development of the matrix, and the reported creep behaviour of the fibres. All testing was done in bend, which made interpretation of the results difficult, but avoided the complexity of tensile creep testing (the limited specimen size of 50mm would make adequate gripping, extensometry and even heating very hard to achieve).

Creep in sintered or hot pressed silicon nitrides occurs as a result of grain boundary diffusion and/or sliding due to the presence of a glassy grain boundary phase (the glassy phase is incorporated to allow densification as in pure silicon nitride diffusion etc. is difficult due to covalent bonding). It has long been recognised that the high temperature behaviour of silicon nitrides is largely dependant on the properties of the grain boundary phase, and the improvement of properties has concentrated on reducing the volume fraction (using HIPping to obtain higher pressures during sintering) or controlling the grain boundary composition (to produce a refractory phase). The 6wt%Y_2O_3/2wt%Al_2O_3 additive silicon nitride system is easily densified in the monolithic state and was chosen for

use in the composite because the effect of fibres on sinterability of the matrix was unknown. The system does not however represent the state of the art in terms of high temperature strength and creep resistance. Syalon 201 (a commercially available hot pressed monolithic silicon nitride) is produced using carefully controlled amounts of Y_2O_3, Al_2O_3 and AlN to produce a 'balanced' composition, in which a second crystalline grain boundary phase (yttrium aluminium garnet or YAG) is produced. The material has good high temperature strength and is highly resistant to creep, compared to the 6wt%/2wt% material in monolithic form. A disadvantage with the YAG second phase is that above 1300°C, it undergoes catastrophic oxidation (involving a volume expansion) causing severe disruption of the material.

More stable systems under oxidation have been investigated that use only Y_2O_3 and SiO_2 additions, and has crystalline yttrium disilicate as a grain boundary phase. Careful control of the oxygen content in the material is necessary for a fully crystalline phase to be formed, which would probably prove difficult using the SRBSN route, where extra oxygen could be accidentally added during the different processing steps. The material investigated in [74] was densified by the HIPping route, allowing the liquid phase content (at the sintering temperature) to be minimised.

The variation in creep behaviour between samples from the first and second plates was assumed to be due to variations in fibre volume fraction and distribution, grain boundary volume fraction and composition. Stress exponents greater than unity have been associated with dislocation movement within the crystal lattice [2], and cavitation within the grain boundary phase. The stress exponents calculated indicate a cavitation dominated mechanism for samples from both plates (n=1.73 for plate 1 and n=3.05 for plate 2), dislocation movement within the Si_3N_4 lattice being difficult at 1300°C due to covalent

bonding. A stepped creep test (on a single specimen from plate 2) indicated a lower value, generally associated with a diffusional creep mechanism, or viscous flow within the grain boundary phase allowing grain boundary sliding. Because testing was only carried out at one temperature (1300°C) no estimate of the activation energy could be made. In the composite, the overall creep rate will be controlled by the component with the highest creep behaviour (taking into account stress distribution between the components and volume fractions), so the ideal situation for the SRBSN/SCS-6 composite system is that the creep rate of the matrix is lower than that of the fibre, allowing the fibre to limit the composite creep performance.

Fibre creep data is only available for times up to a few hours [82], compared to the longer term (>50 hours) creep testing of the SiC/SRBSN composite, so it is difficult to assess the contribution of the fibres to the overall creep rate. A relaxation parameter γ was defined in [82] as

$$\gamma = \ln t - 57700/T$$

where t is the time in seconds, and T is the thermodynamic temperature. The creep compliance J_c is a function of γ and can be defined as

$$J_c(\gamma) = \varepsilon_c / \sigma$$

The relationship between J_c and γ was given as a series of curves for different conditions (e.g. fibre pretreatment between 1400 and 1450°C, creep testing <1450°C), for values of γ up to -25 (corresponding to 32 hours at 1300°C). The fibre pretreatment at 1400-1450°C is the nearest to the temperatures experienced by the fibre during processing of the SiC/

SRBSN composite, and the curve corresponding to this pretreatment temperature range was chosen for calculating the likely creep behaviour of the fibre. Values of creep strain ε_c were calculated for 5, 10, 20 and 30 hours and the resulting curve is shown in fig.6.27, together with the corresponding creep data obtained from the SiC/SRBSN composite.

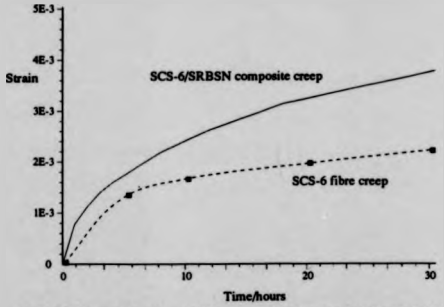

fig.6.27 Creep behaviour of fibre (calculated using data from [82]) compared to SCS-6/SRBSN composite (effective fibre stress of 308MPa).

An effective fibre stress of 308MPa in the outer (tensile) part of the composite bend test sample was calculated by taking into account the fibre volume fraction, and the fibre and matrix moduli. This stress was used in the equation

$$\varepsilon = \sigma J(\gamma)$$

to obtain a value for ε, which was plotted in fig.6.27. The results show that the fibre has a creep rate approximately $^3/_5$ that of the composite. In the composite, the matrix is susceptable to creep deformation, due to softening of the glassy grain boundary. The effective stress on the fibre is therefore likely to increase as the matrix is deformed (the

calculation of effective fibre stress previously made assumed that the stress distribution between the fibre and matrix remained constant). The overall creep rate of the composite would then appear to be higher than that of the fibre in isolation, which is seen in fig.6.27. It is reasonable to assume that an improvement in the creep properties of the matrix would lower the creep rate of the composite, by allowing the stress in the fibre to remain at a constant level. The ideal situation would perhaps be when the fibre and matrix had similar creep behaviour, so that the stress distribution between the fibre and matrix would remain constant (and predictable) throughout the lifetime of a component.

Stress rupture testing, although not as extensive as the testing carried out on dense monolithic silicon nitrides gave a clear indication of a general behaviour that did not appear to have a well defined threshold stress, below which failure did not occur. The precise mechanism of failure is unclear at present, although all specimens failed from a single crack, with little evidence of major fibre pullout, implying that cracking reached a critical level before sudden failure. This is in keeping with the reduced fibre strength inferred at higher temperatures (from more brittle monotonic tests), the measured drop in fibre strength with increasing temperature and the lack of major fibre pullout being seen in all the bend test samples. It is likely that a process of accumulated damage is occurring, the rate of damage being greater at the higher stresses, leading to shorter lifetimes. This may be fibre dominated (fibres relaxing or breaking in areas of greatest stress and passing their load to the surrounding matrix) or matrix dominated (matrix microcracks growing and joining together to form a single critical flaw). In either case, an increase in fibre volume fraction would be likely to have a beneficial effect, as a smaller load would be put on individual fibres for a given external load applied. An increased fibre volume fraction would also be beneficial in terms of the fracture behaviour (i.e. a less catastrophic fracture)

at both ambient and elevated temperatures). It is unclear at present how the creep and stress rupture behaviour will be affected by a higher fibre volume fraction.

CHAPTER 7.0 CONCLUSIONS AND FUTURE WORK

7.1 CONCLUSIONS

A number of composite materials based on the silicon carbide fibre/silicon nitride matrix system have been produced, and investigated both microstructurally, mechanically and physically. Early work concentrated on the silicon carbide/reaction bonded silicon nitride system previously investigated by Bhatt et al [23-27], and the material was found to have poor oxidation resistance due to the open porosity inherent in the matrix. The low strength of RBSN is also a limitation, as the usable stress of the composite is correspondingly low as well (assuming that the matrix cracking stress is a design limit). The investigation allowed the development of a 'prepreg' route for the production of ceramic matrix composites, using the SCS-6 Textron fibre for reinforcement. The prepreg process developed was based on tape casting (a process widely used in the manufacture of electronic ceramics), a slip or slurry of matrix powder (mixed with a polymer binder and associated solvents) being cast over fibres wound with controlled spacing onto a drum.

Further work concentrated on the sintered reaction bonded route to produce a dense (and therefore oxidation resistant) matrix. A system using 6wt% yttria and 2wt% alumina as sintering aids was chosen for the production of a sufficient quantity of material to characterise in some detail. The remainder of the program consisted of characterisation microstructurally (in optical microscopy, SEM and TEM), mechanically (room temperature tensile and bend testing (both as produced material and after long term oxidation), high temperature monotonic and long term bend testing) and physically (density, thermal expansion).

Regarding the initial objectives of the program, the following comments may be made:

1. High temperature mechanical testing and long term oxidation exposure give reasonable confidence in the behaviour of the material at temperatures below 1200°C, and behaviour has been characterised up to 1400°C.

2. The tape casting process has been shown to be a viable method for the production of prepreg sheets of unidirectionally aligned fibres in a silicon nitride matrix. Magnesia and yttria/alumina sintering aids have been assessed for a) densification capability in the presence of fibres and b) reaction with the fibres and consequent micromechanical behaviour of the fibre/matrix interface. Matrices with magnesia sintering aids were found to react more strongly with the outer fibre layers, whereas there was less apparent reaction with the yttria/alumina additive matrix. The fibre/matrix interfacial shear strength for the magnesia additive system was higher (>8MPa) than the yttria/alumina system (2-4MPa), a weak interface being desirable for composite like failure. Tensile testing has yielded an approximate value for the residual fibre strength of 1800MPa after processing, which is around 50% of the initial fibre strength.

3. Mechanical properties were investigated at room temperature and elevated temperature, and after long term high temperature exposure in air. The flexure strength at room temperature was found to be 750MPa (peak), with a matrix cracking stress of 640MPa. At 1200°C these had dropped to 560MPa and 540MPa respectively, and were even lower at 1400°C. Specimens appeared to fail in a composite like manner (*i.e.* a continuation of load carrying capability after the matrix had cracked), the matrix at 1400°C being somewhat plastic, giving a curved stress/deflection curve, and an indistinct matrix failure stress. Long term exposure appeared to degrade the material, lowering the peak strength and matrix cracking strength. 1000°C and 1400°C

exposure appeared to be the most damaging in this respect. For 1000°C exposure, oxygen penetration of the composite via the exposed fibre/matrix interfaces is the most likely cause of damage.

4. The matrix appeared to be fairly dense when examined in the microscope, and composite density measurements gave an average density of around 3.16 gcm^{-3} for the yttria/alumina system finally chosen for in depth characterisation. The coefficient of thermal expansion was found to be approx. $4.2x10^{-6}/K$.

5. The microstructure was evaluated in the SEM, TEM and also optically. Fibre volume fraction was found to be between 15 and 30% (measured by counting fibres in an optical micrograph), and was found to be moderately difficult to control, due to the crudity of the filament winding machine, and of the tape casting system used. The matrix microstructure was found to be similar to related silicon nitrides in SEM investigation, and this was confirmed in the TEM. An amorphous grain boundary phase was present in as produced materials, and was found to contain oxygen, aluminium, silicon and yttrium when analysed using a windowless LINK X-ray detector system. A reaction zone with the matrix was observed in the outer fibre layer, and was studied using X-ray mapping (extending to light elements, carbon etc.) in the SEM, and also in the TEM, where diffraction rings from the zone were identified as silicon carbide.

6. Creep testing at 1300°C has revealed low creep rates ($5x10^{-9}/s$ at 200MPa stress). The creep rate was expected to be the limiting factor in the ultimate use of the material, when the poor intrinsic creep rate of the fibre and matrix are considered. This value compares favourably with monolithic silicon nitrides having an amorphous grain boundary phase.

The stress rupture results indicate that a cumulative damage process occurs at all

stresses (above 200MPa) at 1300°C, with no apparent threshold stress value. This raises implications for design and lifing of components, the design avoiding stresses above 200MPa, and the life of the component at this stress being of the order of 300 hours. If the temperature were lowered, or the fibre volume fraction raised, the failure mechanism could perhaps be altered to give an unlimited lifetime below a certain threshold level but more testing would be needed to confirm this. More reliable and easier to analyse tensile testing in creep and stress rupture is desirable, as the lifetimes of components in the material would be able to be predicted with greater certainty. The stress rupture data has been compared (using Larson-Miller stress rupture analysis) to the state of the art single crystal superalloys, and is considerably better for stresses below 300MPa, although inferior to the state of the art monolithic silicon nitride. To sumarise, for the 6wt%Y_2O_3/2wt%Al_2O_3 additive SRBSN composite described here, the likely failure mode at 1300°C is stress rupture.

7. The prepreg may be cut and stacked to produce a 2D layup of chosen ply orientations and uniaxial hot pressing has been shown to allow a limited number of shapes to be produced (albeit with the limitation of the 150μm diameter fibre). The shapes produced included a filament wound cylinder (using an RBSN matrix), a curved tile, an aerofoil and a T section (the T section was only processed to the first hot pressing stage).

7.2 FUTURE WORK

Future work on silicon carbide fibre reinforced silicon nitride may be divided into two areas.

Firstly, the processing (in particular the prepregging) should be improved to give a more consistent fibre volume fraction, and a more even fibre distribution. Spraying the

matrix slip onto the wound fibres is likely to be more consistent and easily automated than a further development of the tape casting process. The tape casting method may still be retained for the production of monolithic tape. Hot pressing and nitriding are developed technologies which may be easily scaled up, however the HIPping process should be investigated for the final processing step. HIPPing allows the possibility of densifiying more complex shapes, and high pressures (>100MPa) are attainable. A lowering of the final processing temperature would reduce degradation of the fibres, the high pressures available during HIPping making matrix densification possible at lower temperatures than hot pressing.

Secondly, the matrix composition could be refined, perhaps along the lines suggested in [74], in which a controlled matrix composition allowed the crystallisation of the intergranular glassy phase, producing a more refractory material, with improved high temperature properties.

THESIS REFERENCES

1. "Prospects for Ceramics in Airborne Gas Turbine Engines", E.G.Butler and M.H.Lewis, 4th Int.Symp.on Ceramic Materials and Components for Engines, Ed. R. Carlsson (Elsevier 1992) pp.32-49

2. "Mechanical Behaviour of Ceramics", R.W.Davidge, Cambridge Solid State Science Series, Cambridge University Press (1979)

3. "Brittle fracture and toughening mechanisms in ceramics", S.M.Wiederhorn, Ann.Rev.Mater.Sci. 14 (1984) 373-403

4. "Physics of Fracture", Brian R.Lawn, J.Am.Ceram.Soc., Vol.66, No.2, 83-91. (1983)

5. "Silicon Nitride-Based Ceramics for Gas Turbine Application", I.P.Tuersley, G.Leng-Ward, M.H.Lewis., Proc. 3rd Int.Symp. on Ceramics for Engines, Ed. V.J.Tennery, Am.Ceram.Soc. (1988) pp.856-867

6. "Ceramic Steel", R.C.Garvie, R.H.Hannink, R.T.Pascoe, Nature, Vol.258, (1975) p703

7. "Development of Microstructure in High Performance Ceramics", Lena K.Falk, PhD thesis, Chalmers University of Technology, Göteborg, Sweden. (1986)

8. "Strength and Toughness of Ceramic Matrix Composites", W.B.Hillig, Ann. Rev. Mater. Sci., 17, (1987) 341-383

9. "The Unit Strength Concept In The Interpretation Of Beam Test Results For Brittle Materials", P.Stanley, H.Fessler, A.D.Sivill, Proc.Instn.Mech.Engrs. Vol.190 49/76, p585-595 (1976)

10. "Crack Deflection Processes-I. Theory", K.T.Faber and A.G.Evans, Acta.Metall., Vol.31, No.4, pp565-576. (1983)

11. "Crack Deflection Processes-II. Experiment", K.T.Faber and A.G.Evans, Acta.Metall., Vol.31, No.4, pp 577-584, (1983)

12. "Hot-Pressed SiC Whisker/Si_3N_4 Matrix Composites", P.D.Shalek, J.J.Petrovic, G.F.Hurley, and F.D.Gac, Am.Ceram.Soc.Bull.,65 [2] 351-56 (1986)

13. "High-Temperature, High-Strength Materials- An Overview", R.L.Fleischer,Journal of Metals, Dec.(1985),pp16-20

14. "Polymer, Metal, and Ceramic Matrix Composites for Advanced Aircraft Engine Applications", D.L.McDaniels, T.T.Serafini and J.A.Dicarlo, Nasa Technical Memorandom 87132, prepared for the Advanced Composites Conference, Detroit, Michigan, Dec. 3-4, (1985)

15. "Carbon fibre reinforced glass matrix composite tension and flexure properties" K.M.Prewo, J.Mat.Sci. 23 (1988) 2745-2752

16. "Carbon-Carbon Composites", Allen J.Klein, Advanced Materials and Processes inc. Metal Progress 11/86. pp. 64-68. (1986)

17. "Development of Silicon Carbide Fiber with High Tensile Strength", S.Yajima, J.Hayashi, M.Emery and K.Okamura, Nature (London), 261, 683 (1976)

18. "Thermal stability of SiC fibres (Nicalon(R))", T.Mah, N.L.Hecht, D.E.McCullum, J.R.Hoenigman, H.M.Kim, A.P.Katz, H.A.Lipsitt, J.Mat.Sci. 19 (1984) 1191-1201

19. "Microstructural and Microchemical Characterization of Silicon Carbide and Silicon Carbonitride Ceramic Fibers Produced from Polymer Precursors", R.Chaim, A.H.Heuer, R.T.Chen, J.Am.Ceram.Soc., 71 [11] 960-69 (1988)

20. "High-Strength Silicon Carbide Fibre-Reinforced Glass-Matrix Composites", K.M.Prewo, J.J.Brennan, J.Mat.Sci. 15 (1980) 463-468

21. "SiC/SiC Composite Ceramics", Pierre J.Lamicq, Gerald A.Bernhart, Martine M.Dauchier, and Jean G.Mace, Am.Ceram.Soc.Bull., 65 [2] 336-38 (1986)

22. "Fibres for Structurally Reliable Metal and Ceramic Composites", James A.DiCarlo, J.of Metals, June (1985), p44-49

23. "Mechanical Properties of SiC Fiber reinforced Reaction Bonded Si_3N_4 Composites", R.T.Bhatt, presented at 21st University Conference on Ceramic Science sponsered by The University of Pennsylvania, July 17th-19th, (1985), NASA Technical Memorandum TM87085, N85-34223

24. "Properties of Silicon Carbide Fiber Reinforced Silicon Nitride Matrix Composites", R.T.Bhatt, presented at the International Conference on Whisker- and Fiber-Toughened Ceramics sponsored by the American Society for Metals, Oak Ridge, Tennessee, June 6th-9th, (1988), NASA Technical Memorandum TM101356.

25. "Thermal Effects On The Mechanical Properties Of SiC Fibre Reinforced Reaction-Bonded Silicon Nitride Matrix Composites", R.T.Bhatt, R.E.Phillips, J.Mat.Sci., 25, (1990) p3401-3407

26. "High Temperature Tensile Properties Of Fiber-Reinforced Reaction Bonded Silicon Nitride", D.Jablonski and R.T.Bhatt, Presented at ASTM Symposium on Thermal and Mechanical Behavior of Ceramic and Metal Matrix Composites, Nov. 7th, 1988, Atlanta, Georgia.

27. "Role of the Interfacial Thermal Barrier in the Effective Thermal Diffusivity/ Conductivity of SiC-Fiber-Reinforced Reaction-Bonded Silicon Nitride", H.Bhatt, K.Y.Donaldson, D.P.H.Hasselman, R.T.Bhatt, J.Am.Ceram.Soc.,73 [2] 312-16 (1990)

28. "Microstructure/Property Relationships for SiC Filament-Reinforced RBSN", N.D.Corbin, G.A.Rossetti, Jr., and S.D.Hartline, DOD-NASA Sponsored Ceramic Matrix Composites Meeting, Cocoa Beach, Florida, pp. 958-968. (1986)

29. "Silicon Carbide Fibre Reinforced Nitrided Silicon Nitride Composites", R.Lundberg, R.Pompe, R.Carlsson, Sixth International Conference on Composite Materials/Second European Conference on Composite Materials, Vol. 2, (1987), (Elsevier)

30. "SiC Monofilament-Reinforced Si_3N_4 Matrix Composites", D.K.Shetty, M.R.Pascucci, B.C.Mutsuddy, and R.R.Wills, Ceram.Eng.Sci.Proc., 6, 632-645 (1985)

31. "Characteristics of Hot-Pressed Fiber-Reinforced Ceramics with SiC or Si_3N_4 Matrix",T.Miyoshi, H.Kodama, H.Sakamoto, A.Gotoh, S.Iijima.,Conf.Proc. Oak Ridge, Tennessee.USA. 7-9 June (1988)

32. "Tough Silicon Nitride Matrix Composites Using Textron Silicon Carbide Monofilaments",W.Foulds,J.F.LeCostaouec, C.Landrey,S.DiPietro and T.Vasilos, Ceram.Eng.Sci.Proc., 10 [9-10] pp.1083-1099 (1989)

33. "An Introduction to Composite Materials", Derek Hull, Cambridge Solid State Science Series, Cambridge University Press, (1981).

34. "Paper 2 Single and Multiple fracture", J.Aveston, G.A.Cooper & A.Kelly in Conference on the Properties of Fibre Composites, National Physical Laboratory pp.15-26, Guildford, Surrey I.P.C. Science and Technology Press. (1971)

35. "Theory of Multiple Fracture of Fibrous Composites", J.Aveston, A.Kelly, J.Mat.Sci. 8 (1973) pp352-362

36. "On The Theoretical Average Crack Spacing In Brittle Matrix Composites Containing Continuous Aligned Fibres", A.C.Kimber, J.G.Keer, J.Mat.Sci.Letters 1 (1982) 353-354

37. "Some Structural Properties of Ceramic Matrix Composites", A.G.Evans, M.D.Thouless,D.P.Johnson-Walls, E.Y.Luh, 5th International Conf.Proc.Composite Materials (1985)

38. "Fibre Reinforced Ceramics", R.W.Davidge, Proc.World Congress on High Tech Ceramics (6th CIMTEC) Elsevier, Amsterdam (1986)

39. "Mechanics of Matrix Cracking in Brittle-Matrix Fibre Reinforced Composites", L.N.McCartney, Proc.R.Soc.Lond. A409, 329-350 (1987)

40. "Effect of Pull-Out on the mechanical properties of Ceramic-Matrix Composites", M.D.Thouless and A.G.Evans, Acta Metall., Vol 36, No.3, pp 517-522. (1988)

41. "The Tensile Failure Of Brittle Matrix Composites Reinforced With Unidirectional Continuous Fibres", R.W.Davidge, A.Briggs. J.Mat.Sci. 24 (1989) 2815-2819

42. "The Mechanical Behaviour of Ceramic Matrix Composites" (Overview No. 85), A.G.Evans, D.B.Marshall. Acta Metall. Vol 37, No.10. pp2567-2583. (1989)

43. "Perspectives on the Development of High-Toughness Ceramics", Anthony G.Evans, J.Am.Ceram.Soc. 73 [2] 187-206. (1990)

44. "Fiber Debonding in Residually Stressed Brittle Matrix Composites", Panos G.Charalambides, J.Am.Ceram.Soc.,73,[6], 1674-80 (1990)

45. "Tensile Tests of Ceramic-Matrix Composites: Theory and Experiment", Hengchu Cao, Michael D.Thouless, J.Am.Ceram.Soc.,73 [7] 2091-94 (1990)

46. "Ceramic Composites At Extremes Of Performance", D.C.Phillips, in Mechanical and Physical Behaviour of Metallic and Ceramic Composites, Proceedings of the 9th RISO International Symposium on Metallurgy and Materials Science, 5-9 Sept. (1988)

47. "Tensile and Shear Properties of Laminated Ceramic Matrix Composites", O.Sbaizero and A.G.Evans, J.Am.Ceram.Soc., 69 [6] 481-86 (1986)

48. "Tension And Flexural Strength Of Silicon Carbide Fibre-Reinforced Glass Ceramics", K.M.Prewo, J.Mat.Sci. 21 (1986) 3590-3600

49. "High Temperature Properties Of Some Carbon-Carbon Composites" Claus G.Goetzel, High Temperatures - High Pressures, (1980), volume 12, p11-22

50. "Fiber-Reinforced SiC Composites with Improved Mechanical Properties", A.J.Caputo, D.P.Stinton, R.A.Lowden, and T.M.Besmann, Am.Ceram.Soc.Bull., 66 [2] 368-72 (1987)

51. "Mechanical Properties of a Uniaxially Reinforced Mullite-Silicon Carbide Composite", Raj.N.Singh and Achuta R.Gaddipati, J.Am.Ceram.Soc., 71 [2] C-100-C-103 (1988)

52. "The Removal Of Surface Silica And Its Effect On The Nitridation Of High-Purity Silicon", M.N.Rahaman, A.J.Moulson, J.Mat.Sci. 19 (1984) 189-194

53. "The Nitridation of High Purity, Laser-Synthesized Silicon Powder to Form Reaction Bonded Silicon Nitride", B.W.Sheldon and J.S.Haggerty, Ceram.Eng.Sci.Proc.,9 [7-8] pp. 1061-1072 (1988)

54. "Properties of Reaction-Bonded Silicon Nitride Made From High Purity Silicon Powder", J.S.Haggerty, A.Lightfoot, J.E.Ritter, S.V.Nair and P.Gennari, Ceram. Eng. Sci. Proc., 9 [7-8] pp. 1073-1078 (1988)

55. "Strength of Reaction Bonded Silicon Nitride After High Temperature Air Exposure", J.E.Ritter, P.A.Gennari, S.V.Nair, J.S.Haggerty and A.Lightfoot, Ceram.Eng.Sci.Proc., 10 [7-8] pp. 625-631 (1989)

56. "The Formation of Reaction Bonded Si_3N_4 at Low Temperatures and in Short Times", B.W.Sheldon and J.S.Haggerty, Ceram.Eng.Sci.Proc., 10 [7-8] pp.784-793 (1989)

57. Review "Sialons And Related Nitrogen Ceramics", K.H.Jack, J.Mat.Sci. 11. pp.1135-1158 (1976)

58. "SiC Fibers for Advanced Ceramic Composites",Thomas F. Foltz, Ceram.Eng.Sci.Proc. , 6 [9-10] pp. 1206-1220 (1985)

59. "High temperature properties of CVD silicon carbide fibers" James A.Dicarlo , Oak Ridge conf. 7-9 june (1988)

60. "Microstructural Characterization of SiC (SCS) Filaments", F.W.Wawner, A.Y.Teng and S.R.Nutt, SAMPE Quarterly, April (1983), pp39-45

61. "Silicon Carbide Fibers form Methylpolysilane (MPS) Polymers", Jonathan Lipowitz, Gary E. LeGrow, Thomas F. Lim, and Neal Langley (Dow Corning Corp.), Ceram.Eng.Sci.Proc., 9 [7-8] pp 931-942 (1988)

62. "Preform Fiber Architecture for Ceramic-Matrix Composites", Frank K.Ko, Ceramic Bulletin (Am.Ceram.Soc.), Vol.68, No.2, (1989) pp.401-414

63. "Dow Corning(R) X9-6371 HPZ Ceramic Fiber", manufacturers product information

64. "Microstructural Characterisation of Interfaces in Fibre-Reinforced Ceramics", M.H.Lewis & V.S.R.Murthy, Composites Science and Technology 42 (1991) 221-249

65. "Determination of Phase Content of Si_3N_4 by X-Ray Diffraction Analysis", C.P.Gazzara and D.R.Messier, Cer.Bull., Vol.56, No.9 (1977)

66. "Calculation of Stresses and Strains in Four-Point Bending Creep Tests", G.W.Hollenberg, G.R.Terwilliger and R.S.Gordon, J.Am.Ceram.Soc.,Vol.54, No.4, (1971) , pp196-199.

67. "An Indentation Method for Measuring Matrix-Fiber Frictional Stresses in Ceramic Composites", D.B.Marshall, J.Am.Ceram.Soc.,67 [12] C259-C260 (1984)

68. "Temperature Dependence of Interfacial Shear Strength in SiC-Fiber-Reinforced Reaction-Bonded Silicon Nitride", G.Morscher, P.Pirouz, and A.H.Heuer, J.Am.Ceram.Soc.,73 [3] 713-720 (1990)

69. "Ceramics from Hydridopolysilazane", Gary E. LeGrow, Thomas F. Lim, Jonathan Lipowitz and Ronald S. Reaoch, Am.Ceram.Soc.Bull., 66 [2] 363-67 (1987)

70. "Interdisciplinary Research On The Nature And Properties Of Ceramic Materials", (supported by NASA, grant no. NAGW 199), Semiannual Status Report no. 199-7, Dec. 31, (1984), College of Engineering, University of Washington.

71. "A mechanism for the nitridation of Fe-contaminated silicon", S.M.Boyer, A.J.Moulson, J.Mat.Sci. 13 (1978) 1637-1646

72. "Electron Microscopy Study of the Effect of Iron in Reaction-Sintered Silicon Nitride",S.Shinozaki, M.E.Milberg, J.Am.Cer.Soc. Vol.64, No.7, 382-385 (1981)

73. "Modern Boron and SiC CVD Filaments: A Comparative Study", Y. Le Petitcorps, M. Lahaye, R.Pailler and R.Naslain, Comp.Sci.and Tech. 32 (1988) 31-55

74. PhD thesis, I.P.Tuersley, University of Warwick, Dept. of Physics. (1990)

75. "Microstructure-Property Relationships in Silicate Matrix Composites", M.H.Lewis, A.M.Daniel, A.Chamberlain, M.P.Pharoah, M.G.Cain, Journal of Microscopy (to be published)

76. "Investigation of Interfacial Shear Strength in SiC/Si_3N_4 Composites", J.I.Eldridge, R.T.Bhatt, and J.D.Kiser, Ceram.Eng.Sci.Proc. 12 [7-8] pp. 1152-1171 (1991)

77. Review "On Reactions Between Silicon And Nitrogen; Part 1 Mechanisms", H.M.Jennings, J.Mat.Sci. 18 (1983) 951-967

78. "Thermochemical Analysis of Chemical Processes Relevant to the Stability and Processing of SiC/Si_3N_4 Composite", Ajay K.Misra, Ceram.Eng.Sci.Proc. 12 [9-10] pp.1873-1885 (1991)

79. Review "Relationships Between Processing, Microstructure And Properties Of Dense And Reaction-Bonded Silicon Nitride", G.Ziegler, J.Heinrich, G.Wötting, J.Mat.Sci. 22 (1987) pp 3041-3086

80. "Development Of Silicon Nitride Radial Turbine Rotors", Keiichiro Watanabe, Tadao Ozawa, Yoshito Kobayashi and Eito Matsuo, in Proc.4th Int.Symp.on Ceramic Materials ans components for engines. Eds. R.Carlsson, T.Johansson, L.Kahlman. (1991) (Elsevier)

81. "Deformation and Fracture Mechanics of Engineering Materials", Richard W.Hertzberg, 3rd Edition, published by John Wiley & Sons, New York. (1989)

82. "Creep Of Chemically Vapour Deposited SiC Fibres", James A. DiCarlo, J.Mat.Sci. 21 (1986) 217-224